

Functional Organic Thin Films

Dissertation

zur Erlangung des akademischen Grades
Doktor der Ingenieurwissenschaften
(Dr.-Ing.)
der Technischen Fakultät
der Christian-Albrechts-Universität zu Kiel

Michael Scharnberg

Kiel
2007

Für Diana

1. Gutachter

Prof. Dr. R. Adlung

2. Gutachter

Prof. Dr. H. Föll

3. Gutachter

Dr. P.S. Ho

Datum der mündlichen Prüfung

07.09.2007

Contents

1	General Introduction	1
2	Noble Metal Diffusion in Organic Crystalline Thin Films	3
2.1	Introduction	3
2.2	Organic Electronics	4
2.2.1	Organic Semiconducting Materials	4
2.2.2	Metal-Organic Interfaces	9
2.2.3	Field Effect Transistor Structures	13
2.3	Diffusion in Organic Crystalline Materials	16
2.4	Methods	17
2.4.1	Radiotracer Technique	17
2.4.2	Deposition of the Radiotracers	18
2.4.3	Ion Beam Sputtering	20
2.4.4	Detection of the Radioactive Decay	24
2.4.5	Determination of the Sputter Rate	25
2.4.6	Determination of the Surface Topography	26
2.4.7	Deposition of the Metal Contacts	27
2.4.8	Electronic Characterization	27
2.5	Initial Film Growth	28
2.6	Sputtering of Organic Crystalline Materials	31
2.7	Noble Metal Diffusion in DIP and Pc	33
2.7.1	Ag Depth Profiles	33
2.7.2	Au Depth Profiles	46
2.8	Correlation between Diffusion and Device Properties	47
2.8.1	Sample Preparation	47
2.8.2	Electronic Characterization	48
2.9	Summary and Outlook	55
2.10	Author's Related Publications	57
3	PTFE Capping Layers for Organic Field Effect Transistors	58
3.1	Introduction	58
3.2	Multilayer Barriers for OLEDs	58
3.3	Methods	61
3.3.1	PTFE Deposition	61
3.3.2	Determination of the Deposition Rate	63
3.3.3	Determination of the Film Thickness	64

3.3.4	Electronic Characterization	65
3.4	PTFE Capping Layers for Pc-FETs	65
3.4.1	Degradation Mechanisms	65
3.4.2	Sample Preparation	66
3.4.3	Degradation Measurements	67
3.5	Summary and Outlook	69
3.6	Author´s Related Publications	70
4	Teflon-based Electret Layers for Threshold Voltage Tuning	71
4.1	Introduction	71
4.2	Electrets	73
4.2.1	Basics	73
4.2.2	Selection of the Electret Material	75
4.3	Methods	76
4.3.1	Thermal Evaporation of Teflon AF	76
4.3.2	Electret Charging	78
4.3.3	Charge Density Measurements	79
4.3.4	Electronic Characterization	79
4.4	Tuning of the Threshold Voltage	79
4.4.1	Sample Preparation	80
4.4.2	Electronic Characterization	80
4.5	Summary and Outlook	83
4.6	Author´s Related Publications	85
5	Water Jet Reflection on Ultrahydrophobic Surfaces	86
5.1	Introduction	86
5.2	Reflection of Liquids	87
5.3	Biological and Artificial Ultrahydrophobic Surfaces	88
5.3.1	Nasturtium	88
5.3.2	Teflon-coated Metal Fibers	88
5.4	Methods	91
5.4.1	PTFE Deposition	91
5.4.2	Water Jet	91
5.5	Water Jet Reflection	91
5.6	Summary and Outlook	98
5.7	Author´s Related Publications	99
6	General Conclusions and Outlook	100
	Bibliography	103
	List of Figures	111
	List of Tables	114

1 General Introduction

Organic thin films are used in many technological and engineering applications nowadays. They find use as coatings, sensors [1], detectors [2], as matrix materials in nanocomposites [3], as self-assembled monolayers for surface functionalization [4, 5], as low-k dielectrics in integrated circuits [6] and in advanced organic electronic applications like organic light emitting diodes [7], organic field effect transistors [8] and organic photovoltaics [9] (esp. organic solar cells) and many other applications. OLED displays are now commonly implemented in portable multimedia products like mp3-players. And just recently, self-cleaning ultrahydrophobic and superhydrophilic surfaces found first applications.

Organic thin films can exhibit a large variety of mechanical, electrical and chemical properties depending on their composition and structure. The applications mentioned above use very different properties of these organic thin films. For example, in magnetic nanocomposites for high frequency applications the electric insulating properties of Teflon thin films are used to reduce losses due to eddy currents, while electronic applications utilize very different properties, like a low dielectric number in low-k dielectrics or semiconduction in organic electronics. This work shows how different properties of even the same organic thin film can be used to create different functionalities that alter the macroscopic properties of the coated materials.

Due to the huge variety of organic thin films it is impossible to describe their properties and functionalities comprehensively within the framework of a PhD thesis. In order to address the topic, examples from various fields of actual research in materials science were chosen, including organic semiconductors, dielectrics, barrier layers and hydrophobic materials.

Organic crystalline materials are of great interest for applications in organic electronics, i.e., organic field effect transistors due to their good semiconducting electronic properties [10]. Though a massive research effort has led to promising advances in this field, many challenges remain. The next three chapters deal with issues that arise from the implementation of these functional organic thin films in organic field effect transis-

tors and show how Teflon-based organic thin films can be functionalized to address these issues.

In chapter 2 noble metal diffusion in organic crystalline semiconductors is studied and a method to control the diffusion is tested. Most importantly, the influence of the metal diffusion on the electronic properties of contacts in organic field effect transistors is examined. Chapters 3 and 4 deal with the application of Teflon-based functional organic thin films. They can improve the performance of organic field effect transistors by acting as one part of a protective multilayer against aging and as electret gate layer for control of the threshold voltage of the transistors.

Chapter 5 demonstrates another application of a Teflon-based functional organic film by turning a microstructured metal alloy surface into an ultrahydrophobic surface. The reflection of a laminar water jet from ultrahydrophobic surfaces is shown for the first time and described qualitatively.

In the last chapter the results of this work on organic functional thin films are summed up, finally general conclusions and an outlook are provided.

2 Noble Metal Diffusion in Organic Crystalline Thin Films

2.1 Introduction

Single crystalline silicon is the most important building block of modern microelectronics as it is used as semiconductor in the fabrication of microprocessors. But for large area applications like *active matrix liquid crystal displays* (AMLCDs), for which one or three *field effect transistors* (FETs) are used to control each of the display's pixels, materials other than single crystalline silicon are used. Mostly, *hydrogenated amorphous silicon* (a-Si:H) is used in these FETs and sometimes polycrystalline silicon. Implementation in large area flat panel displays is one promising application for organic semiconductors as their implementation could open the door to novel applications that require mechanical flexibility, low processing temperatures and low costs [8]. For example, a-Si:H requires deposition temperatures of about 360 °C rendering it impossible to use transparent organic substrates [8]. Most organic semiconductors are deposited at or around room temperature, thus creating compatibility with the use of transparent organic substrates.

In recent years there has been a major research effort in the field of organic electronics, i.e. *organic light emitting diodes* (OLEDs) [7], *organic solar cells* [9] and *organic field effect transistors* (OFETs)[8]. But whereas OLEDs are already implemented in commercial products, for OFETs a number of important problems need to be solved before they can be implemented. Metallization of OFETs can lead to metal diffusion into the organic semiconductor thin film in certain OFET structures (see chapter 2.2.3), affecting the electronic properties. Understanding of the interface formation between the metal and the organic thin film as well as of the diffusion behaviour can help to improve the processing of OFETs. With better control of the interface formation the device performance of the FET can be improved [11].

In this chapter, noble metal diffusion in selected organic crystalline semiconductors was studied. An extremely sensitive radiotracer technique was used for the first time

to examine diffusion in these materials. The results are correlated with the electronic properties of contacts between metal and organic semiconductor and the microstructure of the organic thin films. Furthermore, novel concepts in the form of so-called submonolayer barriers, so far only known from polymers, were tested for their ability to control the diffusion behaviour. The chapter begins with an overview of organic semiconductors in general and details on the materials investigated in this study, followed by the discussion of the different types of transistor structures and issues arising from their application. After the description of the experimental methods that were used, the results of the diffusion experiments and the dependence of the diffusion on temperature and microstructure as well as the effect of the submonolayer diffusion barriers are presented. The results of the diffusion measurements are then correlated with the electronic properties of metal-semiconductor contacts that were fabricated using different process conditions. The chapter concludes with a summary of the results and an outlook on future work.

2.2 Organic Electronics

2.2.1 Organic Semiconducting Materials

Organic semiconductors have been researched since the late 1940s [12] and a field effect in an organic semiconductor was first reported in 1970 for a phthalocyanine single crystal [13]. The first polyacetylene OFET was built in 1983. Today, organic semiconductors can be divided into three material groups: polymers, oligomers and small molecules. All of these organic semiconductors feature alternating single and double bonds between the carbon atoms of the backbone, a so-called *conjugated* structure. However, these three groups differ considerably with respect to the structure of the films they form. Semiconducting polymers form mostly amorphous, disordered films, while oligomers and small molecules can form ordered films. The small molecules can form polycrystalline films and even single crystals. These highly ordered structures show *charge carrier mobilities* that are orders of magnitude higher than those of polymeric semiconductors (see tab. 2.1), making them the most promising candidate materials for organic electronics. The charge carrier mobility μ of the semiconductor is defined as

$$\mu = \frac{v}{E} \quad (2.1)$$

Material	class	Mobility μ (cm ² /Vs)	Reference
Si (single crystal) (poly-crystalline) (amorphous)	inorganic	450 (h ⁺), 1400 (e ⁻)	[14]
		10-10 ²	[14]
		1	[8]
Pc	small molecule	3-5	[15]
DIP	small molecule	0.1	[16]
Rubrene	small molecule, single cry.	10	[17, 18]
hexyl-substituted sexithiophene	polymer	0.05	[19]

Table 2.1: Mobilities of selected inorganic and organic semiconductors. The mobility of single-crystalline silicon is orders of magnitude higher than the mobility of the best organic semiconductors. Polycrystalline pentacene and diindenoperylene films show mobilities in the range of amorphous silicon.

with v being the velocity of the charge carrier and E the electric field causing the drift of the charge carriers. It is a very important figure of merit for organic semiconductors. Typical values for the mobility of some selected materials are given in tab. 2.1. The mobilities of even the best organic semiconductors are orders of magnitude lower than the mobility in single crystalline silicon, ruling out applications requiring high switching speeds like fast logic circuits. However, a field-effect mobility (i.e. the mobility determined from the current voltage characteristics of the FET) in the range of 1 cm²/Vs is sufficient for its use in displays. Other applications, like *radio frequency identification tags* (RFID-tags) could also be realized with such organic semiconductors.

In disordered semiconductors like polymers transport occurs by hopping processes between localized states as no bands can form. Hopping is assisted by phonons so that μ increases with temperature but is typically very low ($\mu \ll 1$ cm²/Vs) [8]. In highly ordered films, like crystals formed by small molecules, overlap of the $\pi - \pi^*$ orbitals can lead to the formation of small intermolecular bands [20] resulting in band-like transport of delocalized charge carriers [8].

Fig. 2.1(a) shows the electronic structure of a polyatomic molecule. The atomic nuclei form individual potential wells. The *atomic orbitals* (AOs) within these potential wells are the core levels of the individual atoms. The electrons that occupy these AOs can be localized at the site of the atoms. At higher energies the wells merge to form one large well. The electrons that occupy these *molecular orbitals* (MOs) are delocalized over the whole molecule, i.e. they are shared by all atoms of the molecule. The MOs up to the *highest occupied molecular orbital* (HOMO) are occupied with electrons. The next-highest MO is called the *lowest unoccupied molecular orbital* (LUMO). The energy

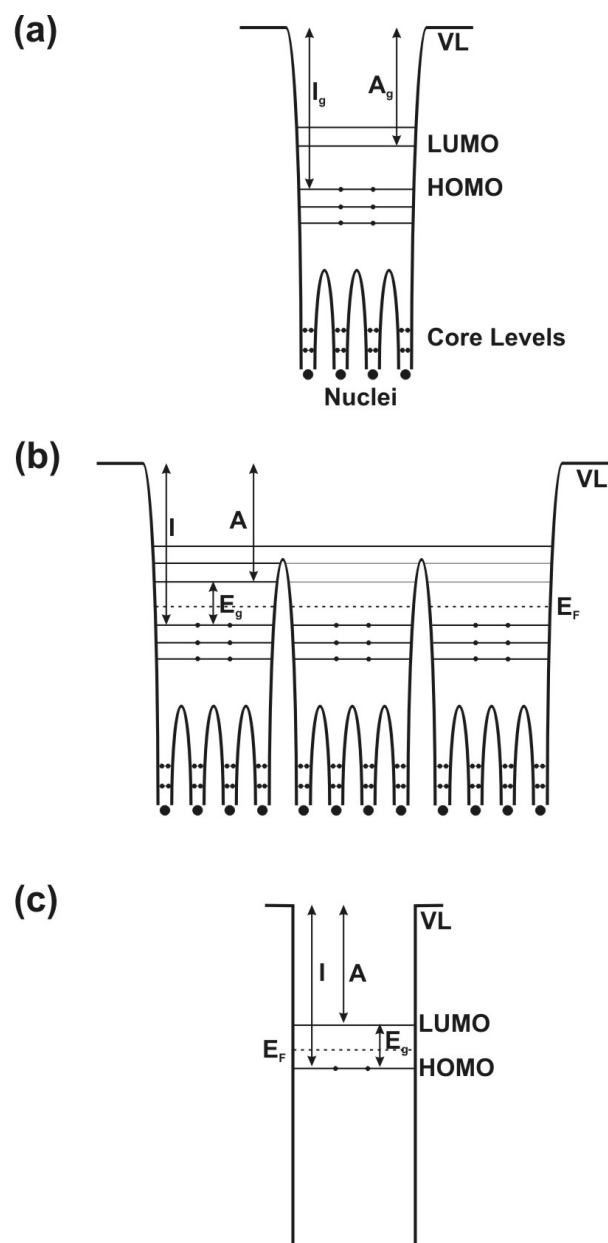


Figure 2.1: Energy diagrams of molecules and molecular solids. (a) Energy diagram of a polyatomic molecule. While the core level electrons are localized at the individual atoms, the electrons occupying the molecular orbitals are delocalized over the entire molecule. (b) Energy diagram of a molecular solid. The energy states up to the LUMO are still confined to the individual molecules. In highly ordered organic semiconductors a narrow band forms above the top of the potential wells. (c) Simplification of (b).

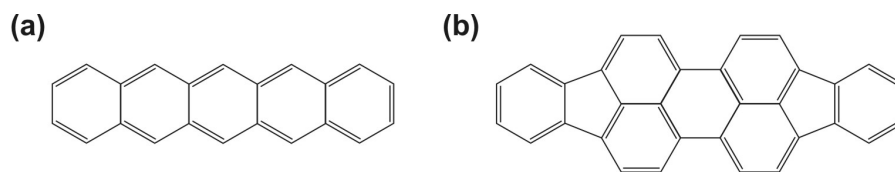


Figure 2.2: Chemical structure of (a) pentacene (Pc) and (b) diindenoperylene (DIP).

difference between HOMO and LUMO is the *band gap* E_g of the organic semiconductor. The energy difference between the HOMO and the *vacuum level* (VL) is called *gas phase ionization energy* I_g and the energy separation between VL and the LUMO is the *electron affinity* A_g . When molecules form an organic solid, i.e. a polymer or organic crystal, a typical electronic structure develops that is shown in fig. 2.1(b) and (c). Due to the weak van-der-Waals interaction the energy states up to the LUMO level are localized in the molecules and transport occurs by hopping. In highly ordered organic semiconductors like organic crystals narrow intermolecular bands will form which allow band-like transport [21–23]. These materials show the highest charge carrier mobilities of all organic semiconductors. These mobilities are sufficient for the realization of organic displays. As they are the most promising class of organic semiconductors they are examined here. From this class two materials were chosen for this work.

2.2.1.1 Pentacene

Pentacene (Pc) was selected for the diffusion studies because it shows mobilities that are in the range of a-Si:H (see tab. 2.1). It is one of the most intensively studied organic semiconductors due to these high reported mobilities. Organic AMLCDs using Pc field-effect transistors have already been demonstrated [10]. This makes them directly relevant for technical applications. Pc belongs to the group of small molecule semiconductors with the molecules consisting of five fused aromatic rings, as show in fig. 2.2(a). Pc thin films can be deposited by thermal evaporation. Depending on the deposition parameters, Pc either forms amorphous films, polycrystalline films or single crystals. In crystals the molecules arrange in the so-called herringbone structure (see fig. 2.3).

2.2.1.2 Diindenoperylene

Diindenoperylene (DIP) (see fig. 2.2(b)) is another small molecule that forms highly ordered films. It was chosen for the diffusion studies because it not only possesses good charge carrier mobilities (see tab. 2.1) but its microstructure can be controlled precisely

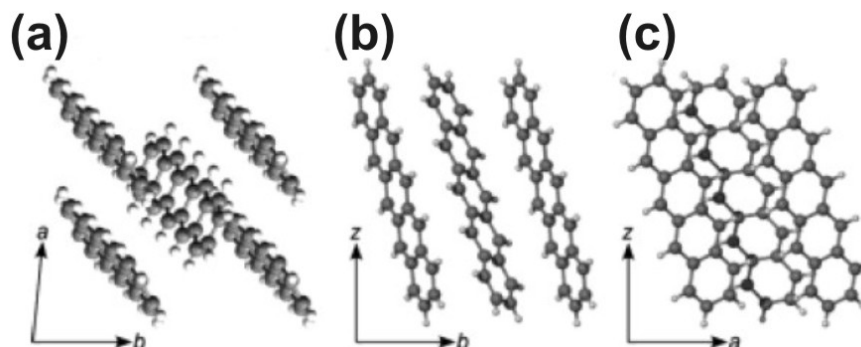


Figure 2.3: Normal views of the ab planes (a) of bulk pentacene and the respective side views (center (b), right (c)). The z -axis is the normal to the ab plane (from [24]).

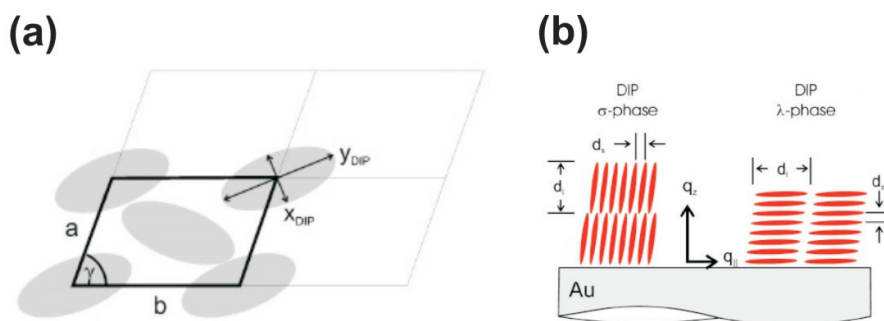


Figure 2.4: (a) Schematic representation of a possible unit cell of DIP molecules in σ -phase in the x - y plane. a and b are the C axes and γ is the angle between the axes. (b) Sketch of the two growth modes of DIP molecules in thin films. In the σ -phase (left), the molecules re-stacked with their long axis oriented along the surface normal. In the λ -phase (right), the molecules are lying flat on the substrate surface (both taken from [25]).

during film deposition. This allows to study the influence of the film microstructure (e.g., grain boundaries) on the diffusion of noble metal atoms in organic crystalline semiconductors. In the crystals the molecules arrange themselves in the herring-bone-structure with a unit cell as shown in fig. 2.4(a). Two different phases are observed depending on the growth substrate and growth conditions. In the σ -phase (see fig. 2.4(b)) almost all molecules are standing upright on the substrate with their long axis aligned parallel to the surface normal. Since the overlapping π -orbitals are parallel to the substrate surface and therefore the channel, films formed by σ -phase crystals show a high mobility in field effect transistors [25]. In the λ -phase (see fig. 2.4(b)) the molecules are lying flat on the substrate so that their π -system is oriented perpendicular to the substrate surface leading to low mobilities in OFET structures.

2.2.2 Metal-Organic Interfaces

Before the different field effect transistor designs are discussed, this chapter reviews the electronic properties of two interfaces between metal and organic semiconductor as well as metal-oxide-organic semiconductor which are of decisive importance not only because their electronic properties directly determine the device performance but also because of the influence on the microstructure of the organic semiconductor (see chapter 2.2.3. *Metal-semiconductor* junctions (MS junction) as well as *metal-insulator-semiconductor* junctions (MIS junctions) are a fundamental part of FETs.

2.2.2.1 Metal-Insulator-Semiconductor Junction

MIS junctions are formed between the gate electrode, the gate insulator and the semiconductor. This junction allows control of the charge carrier concentration in the semiconductor by applying a voltage to the gate electrode. The energy diagram of a metal and a p-type semiconductor is shown in fig. 2.5(a). If no voltage is applied equilibration of the Fermi levels E_F of the metal and the semiconductor will cause band bending in the semiconductor at the interface, resulting in a built-in potential V_{bi} . Band bending only occurs in semiconductors with high charge carrier concentrations or in very thick films. For crystalline organic semiconductors, the charge carrier concentration is high enough to assume band bending. If a negative bias is applied to the gate, the band bends upward and the Fermi level in the semiconductor shifts closer to the valence band edge (see fig. 2.5(b)). This leads to an increased *majority charge carrier* (hole) concentration near the interface with respect to the bulk. This condition is called the *accumulation* regime.

If a positive voltage is applied to the metal, the band bends downward and consequently the region near the insulator-semiconductor interface is depleted of the mobile majority charge carriers (fig. 2.5(c)). This is called *depletion* regime. If the positive voltage is increased further, the Fermi level crosses the intrinsic level of the p-type semiconductor E_i [27]. Accordingly, the concentration of the minority charge carriers increases and finally exceeds the hole concentration. Near the interface the semiconductor is now n-type. This regime is called *inversion* regime (see fig. 2.5(d)). Inversion is reached if

$$V = V_{bi} - \frac{Q_d}{C_i} + (E_i - E_F) \quad (2.2)$$

where Q_d is the depletion charge and C_i is the capacitance of the oxide layer. The voltage $V = Q_d/C_i$ is required to compensate the charge in the depletion region at the

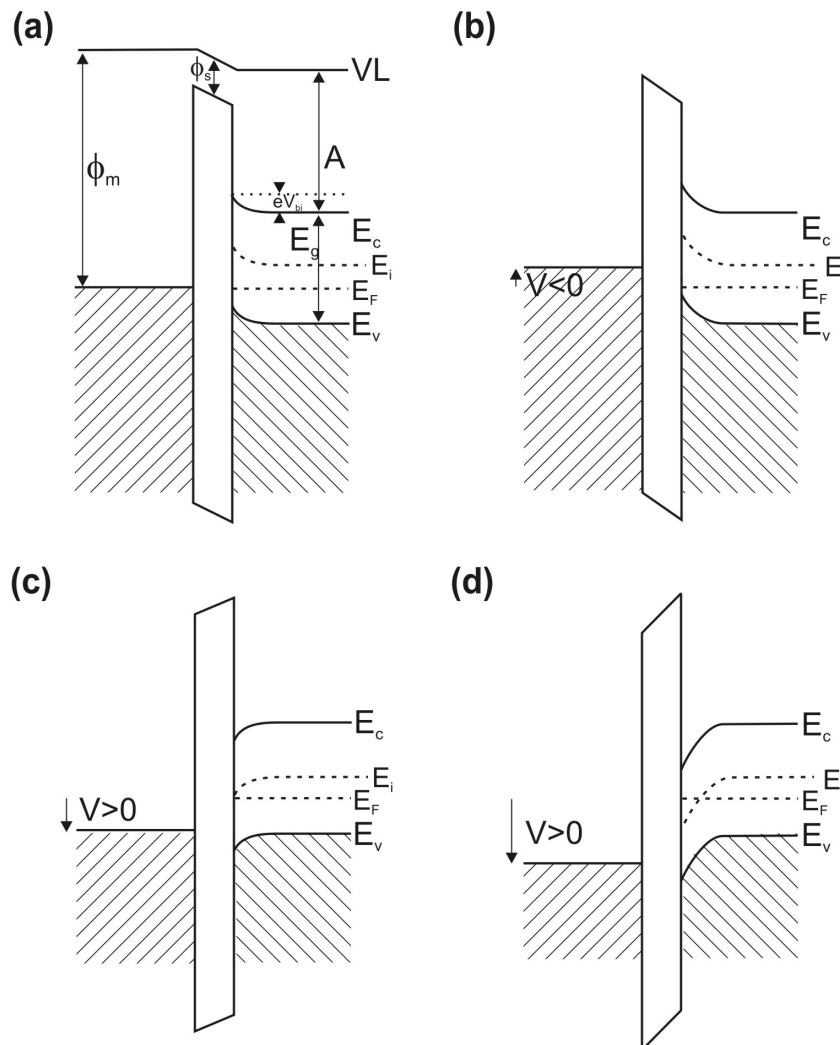


Figure 2.5: Energy diagram of a metal-insulator-p-type semiconductor junction. (a) In equilibrium, alignment of the metal work function ϕ_m and the Fermi energy of the semiconductor E_F leads to band bending and a built-in potential eV_{bi} . (b) By applying a negative voltage to the metal, the bands in the semiconductor bend upward. As the valence band edge E_v approaches E_F , the charge carrier concentration at the interface increases (accumulation regime). (c) If a positive voltage is applied, the bands bend downward and the interface is depleted from mobile charge carriers (depletion regime). (d) If the positive voltage is further increased, E_F crosses the middle of the band gap (E_g) [26] and the intrinsic level of the semiconductor E_i bends below the Fermi level [27]. Thus the interface region is inverted from p-type to n-type behavior.

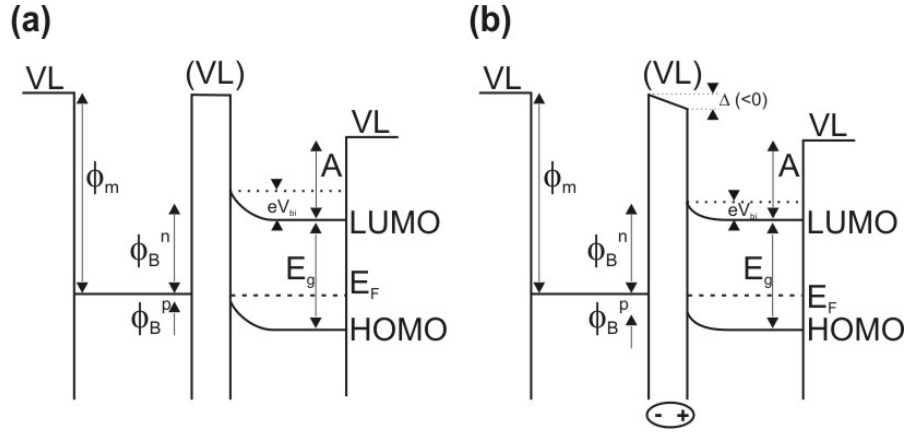


Figure 2.6: Energy diagram of a metal-semiconductor junction (a) without and (b) with formation of an interfacial dipole Δ . The electron and hole injection barriers ϕ_B^n and ϕ_B^p are determined by the metal work function ϕ_m , HOMO and LUMO of the semiconductors and in case of (b) Δ .

interface. If the condition in equation 2.2 is fulfilled this is called *weak inversion*. In order to form a conduction channel *strong inversion* is required. The voltage required for strong inversion is called the *threshold voltage* V_{th} which is given by

$$V_{th} = V_{bi} - \frac{Q_d}{C_i} + 2(E_i - E_F) \quad (2.3)$$

2.2.2.2 Metal-Semiconductor Junction

MS junctions are a very important part of a FET as they are formed between source and drain material and the organic semiconductor. Important electronic properties like the charge carrier injection barriers are determined by this junction. The energy diagram of a junction between a metal and an organic semiconductor is displayed in fig. 2.6. Equilibration of the Fermi levels leads to charge redistribution and band bending near the interface. In *thin film transistors* (TFTs) (see chp. 2.2.3), charges need to be injected from the source into the semiconductor and from the semiconductor into the drain. Therefore, ohmic contacts are required and for good device characteristics the injection barrier should be low. The *hole injection barrier* ϕ_B^p and *electron injection barrier* ϕ_B^n are given by

$$\phi_B^p = I - \phi_m \quad (2.4)$$

$$\phi_B^n = \phi_m - A \quad (2.5)$$

where I is the solid state ionization energy, A the electron affinity and ϕ_m the work function of the metal. In order to form an ohmic contact with a p-type semiconductor like Pc and DIP a high work function metal is required. The work function of the chosen metal should be close to I of the semiconductor in order to minimize ϕ_B^p . For DIP and Pc, Au is used as contact material as the work function of Au and the LUMOs of Pc and DIP are of about the same value. Formation of an interfacial dipole layer can influence the energy alignment at the interface. The dipole layer can originate from several different processes like charge transfer, chemical reactions at the interface or alignment of permanent dipoles [20]. The energy diagram of a MS junction with a dipole layer is shown in fig. 2.6(b). As the dipole layer influences the energy alignment it also effects the carrier injection. Equations 2.4 and 2.5 change to

$$\phi_B^p = I - \phi_m - \Delta \quad (2.6)$$

$$\phi_B^n = \phi_m - A + \Delta \quad (2.7)$$

where Δ is energy shift due to the dipole layer. Depending on the sign and magnitude of Δ , the dipole layer can either enhance charge carrier injection by lowering ϕ_B^p or impair it by increasing ϕ_B^p . The sequence of the film deposition can further affect the interfacial electronic structure. While deposition of organic films onto metals leads to the formation of sharp interfaces, metal deposition onto organic films can lead to formation of a dipole layer due to reactions between arriving metal atoms and the organic film. As mentioned in the introduction, metal atoms might also diffuse into the organic film during metallization. In these cases, the interface cannot be regarded as a simple MS junction between a metal and an organic semiconductor [20]. The interface should rather be considered as an additional layer created by reaction or diffusion. This additional layer might have a serious effect on charge carrier injection if the charge carrier injection barriers are increased or decreased by its formation.

For a noble metal like Au no strong interaction with the organic film is to be expected. For Au deposition onto DIP it was already shown that Au is only physisorbed [25]. Due to the weak interaction between the metal and the organic film diffusion might readily occur. It is very important to understand the diffusion behavior of noble metal atoms during metallization of OTFTs in order to control the formation of the interface and its electronic properties. Therefore, a combination of radiotracer diffusion and electric measurements was used to study the interface formation between noble metals and organic crystalline semiconductors.

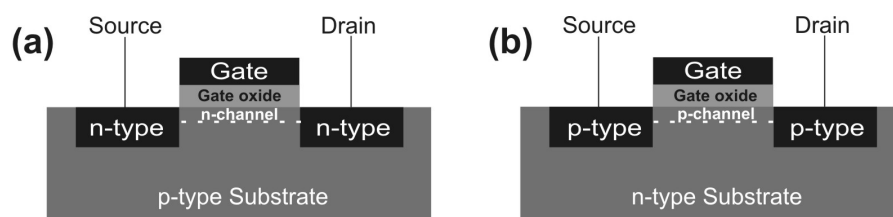


Figure 2.7: Schematics of (a) a *n*-channel MOSFET and (b) a *p*-channel MOSFET. Two regions of similar doping are separated by a substrate with opposite doping. By application of a voltage to the gate, a small region at the interface to the gate oxide can be inverted (see chp. 2.2.2.1). Through this channel a current can now flow from source to drain if a voltage is applied between the two. The schematics are not drawn to scale.

2.2.3 Field Effect Transistor Structures

Field effect transistors can be realized in various designs. In order to understand the problems arising from their implementation, the basic concepts of some device architectures are briefly discussed here. The emphasis is put on the *thin film transistor* (TFT) design which is commonly used for OFETs.

The first transistor ever to be built in 1947 was a *bipolar transistor* based on inorganic semiconductors [28, 29]. Bipolar transistors are mainly used in amplifiers nowadays. Since this work focuses on FETs the working principles are not discussed in detail here, but can be found in many textbooks (e.g., [27]). FETs have been successfully implemented in practical applications since 1960 [30]. FETs realized with single crystalline silicon are most commonly used in microelectronics today, especially in the field of microprocessors and logic. Basically, in a FET a current flowing between two electrodes (*source* and *drain*) is controlled by a voltage applied to a third electrode (*gate*). A FET can be realized by various structures and the most common one is the *metal-oxide-semiconductor field effect transistor* (MOSFET) also called *metal-insulator-semiconductor field effect transistor* (MISFET). In a silicon MOSFET structure (see fig. 2.7), the *n*-type (*p*-type) source and drain are separated by the *p*-type (*n*-type) substrate. The gate is isolated from the channel by an insulating layer, most commonly an oxide. In the *n*-type region the majority charge carriers are electrons and in the *p*-type region holes. Without a voltage or a negative (positive) voltage applied to the gate, almost no current can flow from source to drain. If a positive (negative) voltage is applied to the gate, electrons (holes) are attracted into a narrow region along the gate. If the voltage is sufficiently large (threshold voltage, see chp. 2.2.2.1), the *p*-type (*n*-type) nature of the substrate changes to *n*-type (*p*-type) in a narrow channel along the gate oxide. Through this con-

ducting n-channel (p-channel) a current can flow between source and drain. This device operates in the inversion regime, as the type of majority charge carrier is inverted in the channel.

Since a-Si:H and organic semiconductors are only deposited as thin films, MOSFET structures are not feasible. Therefore, FETs from these materials are realized in the TFT design (see fig. 2.8)[14, 26]. As for the MOSFET, the gate is also separated from the active layer by an insulating layer. In contrast to MOSFETs, the semiconductor only forms a thin layer on a substrate. Source and drain are ohmic contacts that are in direct contact with the semiconductor. If a positive voltage is applied to the gate in case of a p-type organic semiconductor, the semiconductor near the gate is depleted of positive charge carriers resulting in a high channel resistance and a small *off-current* I_{off} . If a negative voltage is applied to the gate during operation, positive charge carriers are accumulated in the channel resulting in a low channel resistance and a high *on-current* I_{on} . Due to the large number of charge carriers I_{on} increases drastically with increasing *drain-source voltage* V_{DS} . In the accumulation regime the *drain-source current* I_{DS} is given by

$$I_{DS} = \frac{w}{l} \mu C_i \left[(V_{GS} - V_{th}) V_{DS} - \frac{V_{DS}^2}{2} \right] \quad (2.8)$$

where w and l are the width and the length of the channel respectively. μ is the mobility of the majority charge carriers, C_i the capacitance of the gate insulator, V_{GS} the *gate-source voltage* and V_{th} the *threshold voltage*. Therefore, a TFT works in the accumulation regime. While the threshold voltage for MOSFETs is clearly defined as the onset of the strong inversion regime, the notion of a threshold in TFT is not fully justified, as currents can already flow at 0 V gate bias [31]. Therefore, the threshold voltage of an ideal p-type TFT is positive. It is defined as

$$V_{th} = V_{bi} + \frac{qp_0 d_s}{C_i} \quad (2.9)$$

where V_{bi} is the built-in potential, q is the elementary charge, p_0 is the bulk hole density, d_s is the thickness of the semiconducting film and C_i is the capacitance of the insulator.

Two important figures of merit are the current modulation ($I_{\text{on}}/I_{\text{off}}$ ratio) and V_{th} . In order to compete with a-Si:H-TFTs an *organic thin film transistor* (OTFTs) must have an $I_{\text{on}}/I_{\text{off}}$ ratio in the order of 10^6 or higher and a threshold voltage of 15 V or less and, as mentioned before, a field effect mobility μ of at least $1 \text{ cm}^2/\text{Vs}$ [8]. Due to the low mobility and low intrinsic charge carrier concentration of organic semiconductors and due to the low film thickness, I_{off} is very small and therefore high $I_{\text{on}}/I_{\text{off}}$ ratios can be

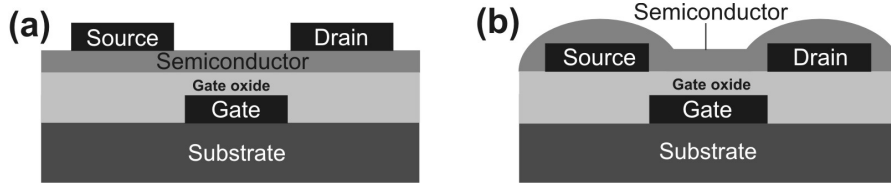


Figure 2.8: Schematics of (a) a top-contact thin film transistor (TOC-TFT) and (b) a bottom-contact thin film transistor (BOC-TFT). In the TOC-design the semiconductor is only deposited on the gate oxide, while for the BOC-TFT the semiconducting film is grown on the gate oxide and metal contacts. Due to the poor film growth on metal, the performance of BOC-TFTs is inferior to those of TOC-TFTs. The schematics are not drawn to scale.

realized. However, the threshold voltages required to obtain a good device performance can be in the order of typically 50-100 V, which is undesired for applications. The reason for the high threshold voltages might either be high doping levels or undesired doping due to impurities, which result in a high bulk hole density p_0 , large film thicknesses (high d_s or a thick gate dielectric (small C_i)). This causes a high threshold voltage as the second term of equation 2.9 increases [32]. TFTs can be realized in different configurations. In *top contact thin film transistors* (TOC-TFTs) the source and drain contacts are deposited on top of the semiconductor (see fig. 2.8(a)) and in *bottom contact TFTs* (BOC-FETs), the semiconductor is deposited onto source and drain (fig. 2.8(b)). In polycrystalline films not only the structural order is very important for the device performance of an OFET but also the microstructure of the films. The charge carrier mobility μ of a polycrystalline film is given by

$$\mu_{total}^{-1} = \mu_{cry}^{-1} + \mu_{gb}^{-1} \quad (2.10)$$

where μ_{cry} is the mobility in the crystal (intragrain mobility) and μ_{gb} is the contribution of the grain boundaries to the overall mobility. It follows from equation 2.10, that large grain sizes and a low density of grain boundaries are favorable. Since the substrate onto which the semiconductor is deposited plays an important role during growth of the organic film, the field effect transistor structure can have a direct impact on the mobility of the semiconductor.

In TOC-OFETs the organic thin film is deposited onto a single type of substrate, most commonly silicon dioxide (SiO_2). Pc as well as DIP show good growth behavior on SiO_2 leading to uniform films with large crystallites. In BOC-OFETs the organic film is grown on the gate dielectric as well as on the source and drain contacts, which

are made of gold (Au) in case of both Pc- and DIP-FETs. The growth behavior of the organic crystalline thin films on Au is poor. For Pc it was shown that the grain size of Pc growing on the Au contacts is much smaller than for Pc grains growing on SiO₂ in the middle of the channel and far away from the contacts. Between these two regions a gradual transition region extending into the channel exists [33–35]. The small grains and the resulting high density of grain boundaries are responsible for the low mobilities in Pc-BOC-TFTs (see equation 2.10) and why TOC-TFTs show a superior device performance compared to BOC-TFTs [8]. While DIP deposited onto SiO₂ almost exclusively forms the upstanding σ -phase, it was found that for DIP deposition on Au the σ -phase and λ -phase coexist. As the λ -phase formation is preferred ($\geq 74\%$) the resulting mobility is low as the overlapping π -system is oriented perpendicularly to the channel (see chp. 2.2.1) [25]. For those reasons BOC-TFTs are inferior to TOC-TFTs with respect to performance. Thus, most high performance OTFTs reported are realized as top contact structures [8]. However, while deposition of organic molecules onto metal leads to formation of sharp and stable interfaces, deposition of metal onto organic films can lead to penetration of metal atoms into the organic film [36, 37] making it difficult to control the device properties of TOC-devices [31, 36–39]. Understanding of the interface formation between metal and organic crystalline films is of utmost importance in order to create well defined interfaces and to control the device properties.

2.3 Diffusion in Organic Crystalline Materials

While diffusion in metals, metallic glasses and also polymers is well studied for various systems [40–43], metal diffusion in organic semiconductors has been hardly researched. First information on metal diffusion in organic semiconductors was obtained by cross-sectional *transmission electron microscopy* (TEM) [39, 44]. For Au deposition on DIP substrates at high substrate temperatures and for low deposition rates, it was found that large Au clusters formed within the DIP films and even at the interface between the DIP film and the Si substrate. However, due to the difficult sample preparation for TEM this method is not well suited for this kind of analysis as sample preparation is very difficult and also time-consuming while only a small volume is examined. Even single atoms or small metal clusters, which are difficult to detect by TEM, might already significantly affect the charge carrier concentration and the injection behavior. Photoemission was also used to study the diffusion of metal in organic semiconductors [45], but due to its surface sensitivity it is not suited to study bulk diffusion. Furthermore, the resolution is

also not good enough to detect very small metal concentrations. The high sensitivity of the radiotracer technique allows the detection of even smallest amounts of metal atoms. The resolution is only limited by the detector and the specific activity of the tracer, but is typically in the range of 10^{-4} to 10^{-5} monolayers of metal and therefore provides a higher resolution than any other analytical method.

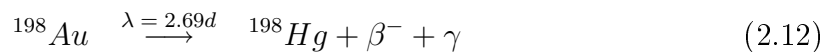
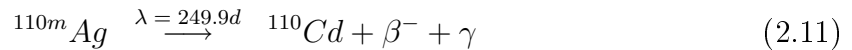
2.4 Methods

The different experimental methods that are needed in order to perform radiotracer measurements of metal diffusion in organic semiconductors are described in some detail in the following chapter followed by a description of the methods used to fabricate the contacts that were used to correlate the diffusion data and the electronic properties of the interface. First, the radiotracer technique itself is introduced. Then, in the following subchapters those experimental methods that are required for the individual steps of the radiotracer technique are described. In the last two subchapters deposition of the source and drain contacts and their electronic characterization are described.

2.4.1 Radiotracer Technique

The radiotracer technique has been used to study diffusion in various systems including metals, metallic glasses and also polymers [40–43]. It uses radioactive isotopes of a given element in order to study its diffusion in the material of interest. In order to achieve that, the tracers must be deposited onto the substrate in which diffusion is to be studied. Depending on the tracer/substrate system, annealing might be necessary after the tracer deposition in order to facilitate and accelerate diffusion. Depth profiles, i.e., the tracer concentration with respect to the distance from the film surface, allow the examination of the metal atoms' diffusion into the organic film during deposition. In order to obtain the depth profiles, serial sectioning of the sample is performed. During serial sectioning the sample is removed in layers by methods like grinding (the different layers are collected by changing the grinding paper) or, as in this work, by ion beam sputtering. In the case of ion beam sputtering, the material that is sputtered off the surface (see chp. 2.4.3 for a description of the sputtering process) is caught on a polymer film. The film is installed in an apparatus that is similar in design to a film camera. A part of the polymer film is exposed to the material that is sputtered off from the substrate. After a layer of a certain thickness is sputtered off the sample, the polymer film is advanced exposing a new piece of the film to the sputtered material. In this way,

sections of the substrate can be caught on different pieces of the film. The activity of the sections can be determined by detection of the radioactive decay of the tracer atoms in the film pieces. Through normalization of the activity in a section with respect to the thickness of the section a depth profile can be constructed. The normalized activity is proportional to the metal concentration of the section. In this work, two types of radiotracers were used. The first, silver (*Ag*) containing a fraction of $1.5 \cdot 10^{-4}$ ^{110m}Ag radio-isotopes, was used in order to compare the results with those obtained for polymers [46]. ^{110m}Ag is a metastable state of the ^{110}Ag isotope and decays to ^{110}Cd by β^- -decay with a half-life of 249.9 days (see equation 2.11). A neutron is converted into a proton and an electron under emission of a γ -ray with a probability > 0.95 . These γ -photons were detected in special detectors and used for analysis. The second tracer used was gold (*Au*) containing a fraction of $1.5 \cdot 10^{-5}$ ^{198}Au isotopes. As mentioned before, Au is used as contact material for Pc and DIP because of the good alignment of the Au work function and the HOMO of the organic semiconductors. A good alignment is important for a low charge carrier injection barrier. ^{198}Au also decays by β^- -decay with a half-life of 2.69 days (see 2.12).



2.4.2 Deposition of the Radiotracers

The tracer metal was deposited onto the organic films by thermal evaporation. It is one of the most commonly used *physical vapor deposition* (PVD) techniques today. Basically, heat is transferred to a liquid or solid until its *vapor pressure* (v_p) exceeds the background pressure in the evaporation chamber leading to evaporation or sublimation respectively. The evaporated material is transported to the substrate, where it condenses and a film is formed. Metals are evaporated as single atoms [47, 48]. Since the mean free path of the evaporated atoms at 1 Pa and 25 °C is only 1 cm, evaporation is performed under high vacuum conditions ($p < 10^{-6}$ mbar), so that the mean free path of the atoms is much larger than the distance from the evaporator to the substrate surface. Under these conditions, the atoms reach the sample without collisions between each other or the residual gas in the chamber (molecular flow regime). The reduced pressure in the chamber also reduces the temperature required to raise the vapor pressure of the material above the chamber pressure. A schematic of the *ultra high vacuum* (UHV) chamber that was used for deposition of the noble metals is shown in fig. 2.9. The sample was placed

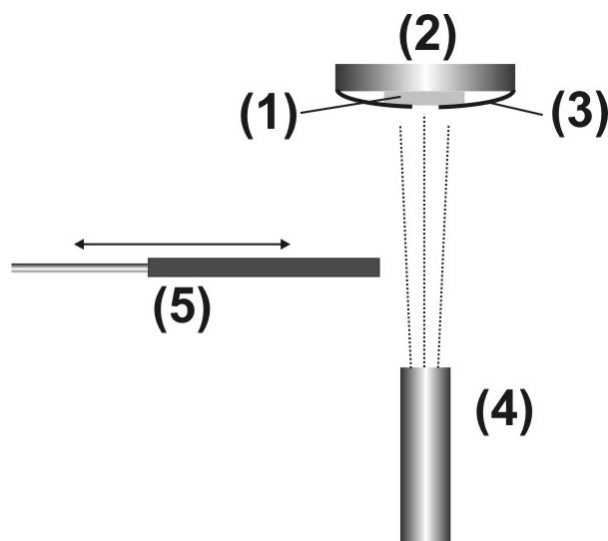


Figure 2.9: Schematic of the vacuum chamber for thermal evaporation of the metal radiotracers. The sample (1) is fixed to the sample holder (2) by a mask (3). The metal tracers are deposited from a thermal evaporator (4). A shutter (5) shields the sample during heating and cooling of the evaporator.

on a heatable sample holder and for thermal coupling of the sample and the sample holder a heat-conductive paste was used. The sample was held in place by a mask with a circular hole in its center. A schematic of the evaporator is shown in fig. 2.10. A tungsten wire is coiled around a steel crucible that contains the noble metal. An electric current provided by a DC power supply was used for resistive heating of the wire. The heat is transferred to the crucible by heat radiation (due to the ultra high vacuum in the chamber the convective contribution to heat transfer can be neglected). The evaporated metal atoms can leave the crucible through a small orifice at the top of the evaporator, the distance between the orifice and the sample holder being 15 cm. In order to shield the sample during heating and cooling of the evaporator, a shutter can be placed in front of the sample. The film thickness was estimated by the total activity deposited onto the sample. The control parameter was the evaporation time. Due to the very low deposition rates (see below) and the deposition of only submonolayers, film thickness monitoring using, e.g., a *quartz crystal microbalance* (QCM) (see chp. 3.3.2) was not possible. The Ag containing the radioactive tracer atoms was evaporated at a crucible temperature of 680 °C at a base chamber pressure of $1.8 \cdot 10^{-8}$ mbar. During evaporation the pressure increased to 10^{-7} mbar. The Au tracers were evaporated at 860 °C at a base pressure of $1.8 \cdot 10^{-8}$ mbar.

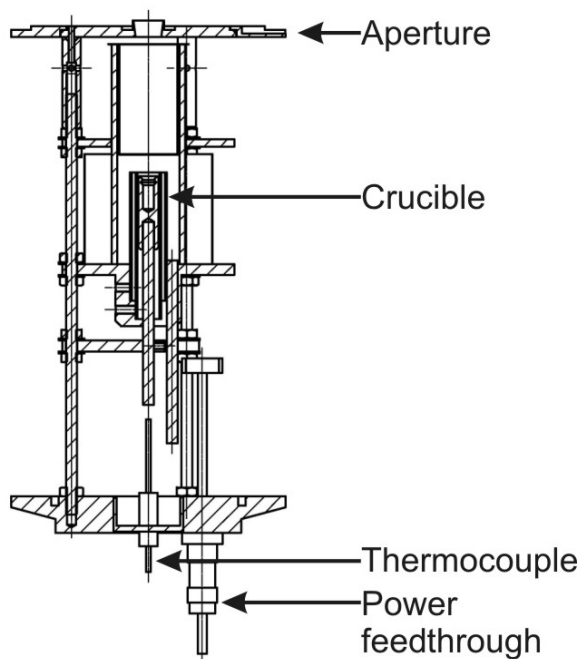


Figure 2.10: Schematic of the metal evaporator used for deposition of the radiotracers.

2.4.3 Ion Beam Sputtering

The serial sectioning was done by ion beam sputtering. Ion beam sputtering is used in a variety of processes and applications like *Secondary Ion Mass Spectroscopy* (SIMS) and surface modification of polymers [49]. Chemical and physical sputtering processes can be distinguished. In chemical sputtering, reactive ions (e.g., oxygen ions) react with the substrate and form volatile species that are desorbed into vacuum. Since an inert gas (krypton (Kr)) was used in this work, only physical sputtering will be discussed in more detail. In general, it is a process in which accelerated ions impinge on a surface and knock out atoms, clusters of atoms or even whole molecules [47, 50]. For ion beam sputtering a gas is ionized in an ion source (also called ion gun) and the ions are accelerated towards the substrate. Typical ion energies vary from 10^2 to 10^8 eV. On impact of the ions onto the surface several processes take place (see fig. 2.11). Depending on the ion energy three different regimes can be distinguished (see tab. 2.2) [51]. Due to the low energies used in this work (10^2 eV), only the first regime will be discussed in the following.

When ions impinge on the surface they are either backscattered directly, mostly as neutral atoms, or penetrate into the substrate. On its way through the substrate, a

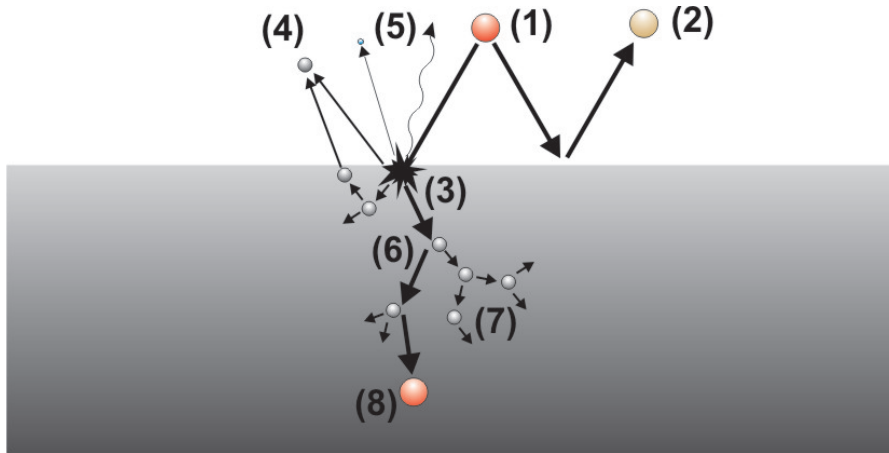


Figure 2.11: Processes occurring during ion impingement. An ion from the sputter source (1) impinges on the surface and is either directly backscattered from the surface (mostly as neutral atom) (2) or transfers a part of its kinetic energy onto atoms of the sample (3). If the transferred energy is larger than their binding energy, atoms are ejected from the sample (4) together with electrons and photons (5). The ion continues to lose energy on its way through the bulk displacing atoms (collision cascade) (6). If the transferred energy is large enough the displaced atoms can also cause a cascade (recoil cascade) (7). When the ion lost all its momentum it is incorporated into the substrate (ion implantation) (8).

Regime	Energy range	process
Single-knock-on	< 1 keV	collision cascades are dilute; only a few atoms involved; no recoil cascade;
Linear-cascade	1-100 keV	recoil atoms cause recoil cascade
Collision-spike	> 100 keV	all atoms in a certain volume are in motion

Table 2.2: Depending on the ion energy different sputtering regimes are observed. The ion energies of 10^2 eV used in this work lie in the single-knock-on regime.

Material	Sputter yield
Au	3.06
Ag	3.27
Si	0.5
C	0.13

Table 2.3: Sputter yields of selected elements for sputtering with Kr ions with a kinetic energy of 500 eV [53, 54].

penetrating ion transfers its momentum onto atoms and molecules of the substrate creating a *collision cascade* (see fig. 2.11). In the *single-knock-on regime* the cascades are dilute and only a few atoms are involved. If the transferred energy exceeds the binding energy of an atom it is knocked out of its place (*recoil atom*), near the surface it might be ejected from the substrate, i.e. it is sputtered. In the single-knock-on regime the energy of the recoil atoms is sufficient for sputtering of the atoms but too low for the recoil atoms to cause a cascade on their own (*recoil cascade*). The ion continues its path through the substrate until it has lost all its momentum and comes to rest and is incorporated in the film (*ion implantation*). The *sputter yield* S is a measure for the efficiency of the sputtering process and is defined by

$$S = \frac{\text{Number of sputtered atoms}}{\text{Incident ion}} \quad (2.13)$$

It can range from 10^{-5} up to 10^3 depending on the material [52]. In tab. 2.3, literature values for selected materials are given. The value of S not only depends on the sputtered material and the type of ion, but also on the angle of incidence and the energy of the ion [47]. In addition to ejected atoms, electrons and photons are also emitted from the sample. Two effects occurring during ion beam sputtering are of special importance with respect to its application in serial sectioning. The first is the knock-on process in the cascade itself. If radiotracer atoms are knocked deeper into the material by an ion or a recoil atom of the cascade, the metal diffusion depth in the depth profiles (see chp. 2.7.1) is overestimated. The second effect is preferential sputtering of different components of a compound. In this case, a system composed of noble metal clusters on top and in an organic film is sputtered. The sputter yield of the organic semiconductors was found to be in the region of graphite (see tab. 2.3). As the sputter yields of metals are much higher than those of the organic semiconductors and Si, the metal clusters should be sputtered much faster than the surrounding material. Due to this effect the metal diffusion would be rather underestimated. All films were sputtered in an UHV

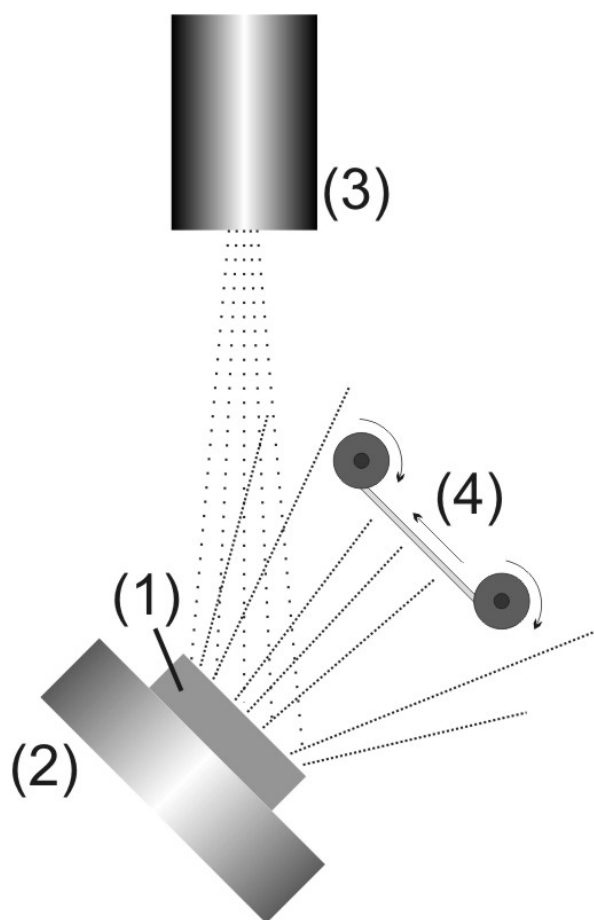


Figure 2.12: Schematic of the UHV chamber used for serial sectioning. The sample (1) is fixed to a rotatable, water-cooled sample holder (2). An ion source (3) was mounted to the chamber in an angle of 45° with respect to the sample. An ion beam emitted from the source sputtered material from the sample surface. A fraction of the material is collected on the polymer film (4). The film could be advanced in order to acquire several "images".

chamber, its schematic layout is shown in fig. 2.12. To assure uniform sputtering the sample was placed on a rotatable copper sample holder, which was water-cooled in order to avoid heating of the sample during sputtering. The sample was fixed to the sample holder by a mask. A shutter could be placed directly in front of the sample during stabilization of the ion source to avoid sputtering of the sample and deposition of material sputtered from the chamber. The ion source used is a 3 cm ion source from Ion Tech, Inc. In the ionization chamber of the source, electrons are emitted from a helical tungsten filament. The electrons are accelerated by a voltage that is applied between two electrodes within the ionization chamber. The electrons ionize the Kr atoms that stream into the chamber through the gas inlet. The Kr ions are extracted from the chamber

and accelerated towards the sample by an acceleration voltage. The kinetic energy of the ions was 160 eV and the angle of incidence 45° . The gas pressure in the chamber during sputtering was $2.5 \cdot 10^{-4}$ mbar and the base pressure $2 \cdot 10^{-7}$ mbar. Semiconducting and insulating materials would charge up during continued sputtering with positive ions reducing the sputter rate. In order to avoid charging the ion source was equipped with a neutralizer filament that was placed between the grids and the sample. A current in the order of 2 A run through the filament led to emission of electrons from the wire. These electrons neutralize the positive charge on the sample surface.

2.4.4 Detection of the Radioactive Decay

The radioactive decay was measured by detection of the γ -photons that are emitted upon decay of the tracers (see equations 2.11 and 2.12). A germanium detector was used for the γ -ray detection. A Ge detector functions as a *solid state ionization chamber*. Some important properties of Ge are given in tab. 2.4. In a large Ge single crystal with a p-n or p-i-n (p-type/intrinsic/n-type) junction either a depletion or intrinsic region exists. A large reverse bias in the order of several kV is applied. The intrinsic region in Ge detectors might have a width of up to 60 mm [55]. An ionizing particle like α - and β -particles and γ -radiation will excite a certain number of electrons into the conduction band, creating electron-hole pairs (e^- - h^+ pairs). The electrons and holes are separated and swept away towards the opposite contacts by the applied electric field. An integrating preamplifier transforms the current pulse into a step voltage. About 33% of the particle energy is consumed by the formation of electron-hole pairs, the rest is transformed into lattice vibrations. Due to the relatively small band gap, Ge detectors have to be cooled down below 100 K in order to minimize leakage currents caused by thermal generation of charge carriers to an acceptable level [55]. Liquid nitrogen is used for cooling of the detector. For protection of the detector surface from moisture

Property	Ge (at 77 K)
Electron mobility μ_e (cm^2/Vs)	$3.6 \cdot 10^4$
Hole mobility μ_h (cm^2/Vs)	$4.2 \cdot 10^4$
Energy ϵ required to create 1 (e^- - h^+)	2.96 eV
Atomic number Z	32
Band gap E_g	0.746 eV

Table 2.4: Physical properties of Ge which was used as detector material for detection of γ -photons [55].

and condensable contaminants it must be operated in vacuum. The entrance window of the vacuum chamber will absorb charged particles like α - and β -particles making Ge detectors less suited for their detection. Low energy ions are also detected with a lower efficiency. However, other photons are detected with high efficiency due to the large width of the intrinsic region of several cm. For comparison, in Si detectors the intrinsic region is only in the order of $10^2 \mu\text{m}$ [55]. Since photons are only detected in the intrinsic region, Ge detectors are more efficient and better suited than Si detectors. The Ge single crystal detector used for this work was p-i-n type from DSG Detector System GmbH which was operated at 2.5 kV.

2.4.5 Determination of the Sputter Rate

In order to plot the depth profiles it is necessary to determine the *sputter rate* r_{sputter} during serial sectioning. The rate can be calculated by

$$r_{\text{sputter}} = \frac{d_{\text{sputter}}}{t_{\text{sputter}}} \quad (2.14)$$

where d_{sputter} is the *sputter depth* and t_{sputter} is the *total sputter time*. Since t_{sputter} is known, only the sputter depth has to be determined. During serial sectioning, the sample was covered by a mask (see fig. 2.13(a)). While the area of the organic film on which the tracers were deposited was centered in the middle of the large opening

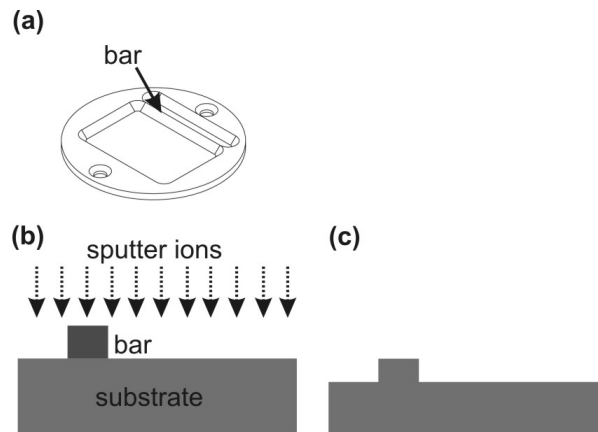


Figure 2.13: (a) Drawing of the mask used to fix the sample to the sample holder. (b) The bar shielded a part of the sample from the ion bombardment. (c) The part of the sample that was covered by the bar remains unsputtered, whereas the rest of the sample is sputtered by the ions. The resulting step in the surface can be measured by a profilometer.

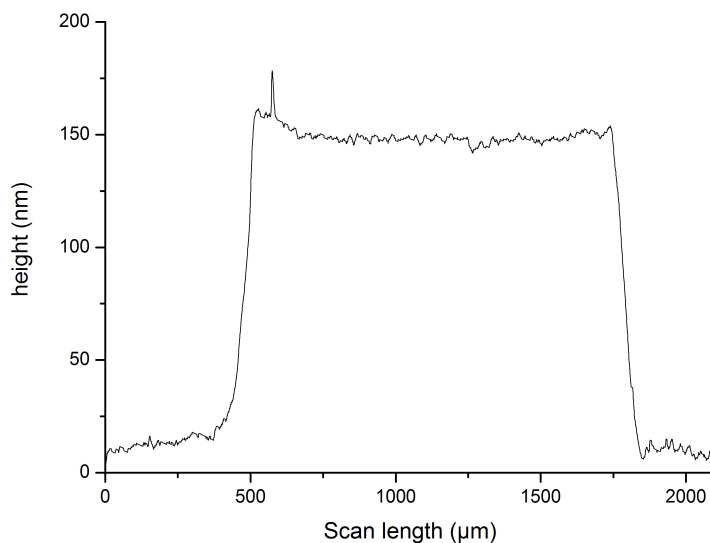


Figure 2.14: Height profile of a DIP surface after sputtering obtained by a profilometer scan. The height of the step is equal to the sputter depth.

of the mask for unhindered sputtering, a part of the film is covered by the bar of the mask. This part of the film is not sputtered during serial sectioning creating a step in the surface profile as shown in fig. 2.13(b,c). The step height is equal to the sputter depth. It was measured using a profilometer, a tool that can determine surface profiles over distances of several millimeters with a resolution in the order of several nanometers. In a profilometer, a fine steel tip is brought into mechanical contact with the sample. The tip is then moved across the surface and its change in height is recorded. With the resulting data a surface profile can be plotted. A typical profile obtained for the surface steps described above is shown in fig. 2.14. The profilometer that was used for these experiments was a Dektak 8000 from Veeco.

2.4.6 Determination of the Surface Topography

Since sputtering of the organic films' surface could influence the surface topography, it is necessary to characterize the surface before and after sputtering. This is of great importance since a change in the surface roughness might influence the interpretation of the depth profiles. *Atomic force microscopy* (AFM) is another analytical method for characterization of the topography of a sample surface. In contrast to the profilometer, AFM is much more sensitive but only allows to analyze a maximum area of (100·100) nm².

For AFM the interaction of a very fine tip, which is attached to a flexible cantilever, and the sample surface is used for imaging. A laser beam is reflected off the back of the cantilever onto a couple of photo diodes causing a photo current. If the tip is brought close to a surface (*non-contact mode*) or into contact with the surface (*contact mode*), the cantilever is deflected due to repulsive forces between the atoms in the tip and the sample. Therefore the position of the laser beam on the photo diodes is changed. If the tip is scanned across the surface at a constant height the photo currents change due to the deflection of the cantilever. The change in the photo currents and the position on the sample is used to image the sample topography. This is called *constant height mode*, a variation of the contact mode. It is mostly suitable for very flat surfaces as rough surface structures might cause the tip to crash into the sample. Another contact mode is the widely used *constant force mode*. Here, the force acting on the cantilever and its deflection are kept constant using the photo currents as a variable of a control loop which controls piezoelectric actuators. This mode reduces the mechanical load acting on the surface as the force exerted by the tip is kept constant. Since the organic surfaces that were examined are very sensitive to mechanical loading and the surface roughness is in the range of 40 nm this mode was chosen for AFM imaging. The AFM that was used was a Park Autoprobe.

2.4.7 Deposition of the Metal Contacts

The source and drain contacts of the examined OFETs were deposited by thermal evaporation of Au as described in chp. 2.4.2 for deposition of the radiotracers. Deposition of the contacts was not performed in the same chamber as the radiotracer deposition in order to avoid contamination of the sample with radioactive isotopes, but the general setup of the chamber is similar to the chamber shown in fig. 2.9. Patterning of the contact structures was obtained using a stainless steel shadow mask. By deposition of Au an array of nine contacts was formed. The contact area of the Au was $50 \times 50 \mu\text{m}$ and the distance between the contacts varied from $300 \mu\text{m}$ to $3290 \mu\text{m}$ (see fig. 2.15).

2.4.8 Electronic Characterization

The Au pads were contacted with fine Au tips. A voltage was applied between the tips using a standard power supply. The resulting currents were measured with a Keithley picoamperemeter. All measurements were performed in ambient air directly after the sample was removed from the vacuum chamber.

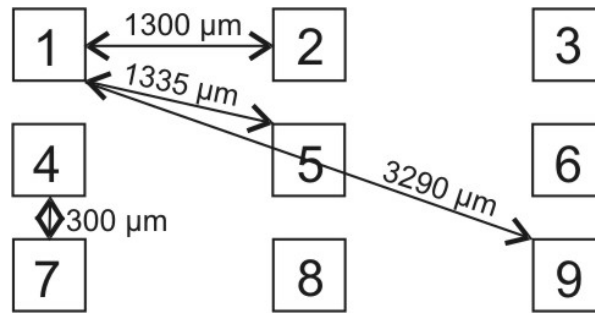


Figure 2.15: Schematic of the contact pattern obtained by deposition through a shadow mask. Nine contacts with an area of $50 \times 50 \mu\text{m}$ were deposited. The shortest separation between the contacts was $300 \mu\text{m}$, the largest $3290 \mu\text{m}$.

2.5 Initial Film Growth

Before the interface formation between noble metals and organic semiconductors and the diffusion of noble metal atoms in these materials can be investigated, some of the general processes occurring during the initial stage of metallization need to be discussed. After impingement on the surface different processes can take place (see fig. 2.16). If the interaction between the atom and the substrate is weak, an atom will diffuse across the surface jumping from site to site for a distance equal to the *average diffusion length* Λ . If it either encounters a preferential nucleation site (e.g., a step or defect on the surface), another diffusing metal atom (random nucleation by cluster formation) or an already existing metal cluster it is adsorbed on the surface and incorporated into the growing film. A single atom or small cluster might also diffuse into the substrate. If none of the aforementioned processes occurs, the atom will be desorbed back into vacuum provided that it gains enough energy in the tail of the room temperature energy distribution. The initial film growth is strongly influenced by the surface energy of the free substrate γ_s , the surface energy of the free film surface γ_f and the surface energy of the interface between film and substrate γ_i . Three general growth modes can arise from the interaction of a growing film and its substrate (see fig. 2.17). If

$$\gamma_f + \gamma_i < \gamma_s \quad (2.15)$$

is valid, it means that the total surface energy is lower for the film-covered substrate than for the bare substrate [47]. In this case, the film grows layer-by-layer in a smooth film (see fig. 2.17(a)). This growth mode is also called *Frank-van der Merwe* growth. For equation 2.15 to be valid, γ_i must be reduced by a strong bonding between film and

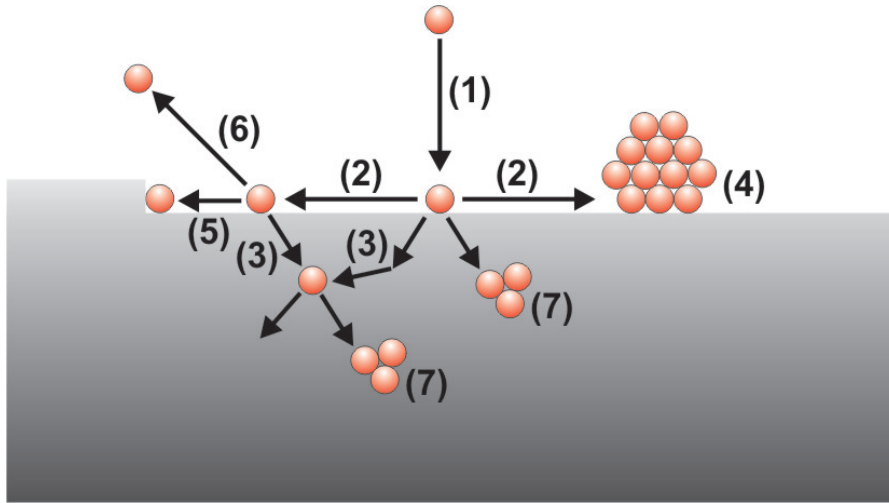


Figure 2.16: Processes occurring during film growth with a certain probability: An atom arriving at the surface (1) can either diffuse across the surface (2) or into the bulk (3). An atom diffusing across the surface might either be incorporated into a cluster (4), be trapped at a surface step or other defect (5) or diffuse into the bulk (3). If none of these processes occurs within a certain time, the atom will desorb again (6). An atom diffusing in the bulk will diffuse until it is immobilized by incorporation into a cluster (7).

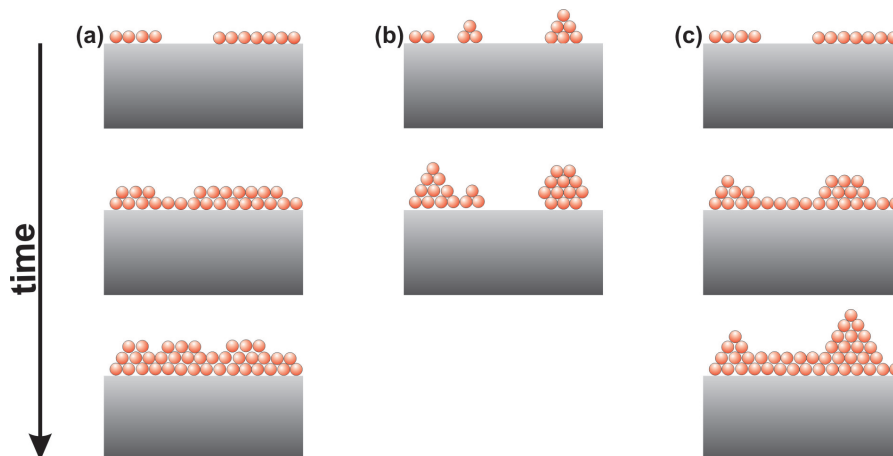


Figure 2.17: The three basic growth modes for thin films. (a) Frank-van der Merve (Layer growth). (b) Volmer-Weber (Island growth). (c) Stranski-Krastanov

substrate. If there was no bonding at all, γ_i would be given by

$$\gamma_i = \gamma_f + \gamma_s \quad (2.16)$$

In this case, wetting of the substrate by the film would increase the total surface energy by $2\gamma_f$. Therefore, already for weak bonding to the substrate equation 2.15 does not hold anymore. Instead of layer-by-layer growth the film forms three-dimensional islands (clusters) on the surface (see fig. 2.17(b)). This growth mode is called *Volmer-Weber* growth. The last growth mode, called *Stranski-Krastanov*, shows a transition from layer-by-layer to island growth after formation of the first monolayer (see fig. 2.17(c)). This transition is caused by a change in the energy situation with deposition of successive layers. As Ag and Au are both noble metals they are not very reactive, so the interaction with the substrate is only weak. This results in a high surface diffusivity, atoms and subcritical clusters can move easily across the surface allowing the growing film to rearrange in order to minimize the total surface energy γA . This fact in combination with the low surface energy of the organic semiconductors investigated in this chapter leads to Volmer-Weber growth of the Ag and Au films as described above. Since only films with a maximum nominal thickness of a monolayer were deposited for the radiotracer measurements, the resulting films consist of metal clusters dispersed on the organic film surface as no closed layer is formed. As described above, not all metal atoms impinging on the surface are incorporated into the growing film. The desorption is thermally activated and the desorption probability is proportional to

$$p \propto \exp\left(\frac{-E_d}{kT}\right) \quad (2.17)$$

where E_d is the energy required for desorption, k is the Boltzmann constant and T the substrate temperature. For that reason, the fraction of the arriving atoms that is desorbed increases with increasing substrate temperature as it becomes more likely that the atoms gain the required energy for desorption. The *condensation coefficient* (or sticking coefficient) is defined as

$$C = \frac{N_a}{N_e} \quad (2.18)$$

N_a being the number of adsorbed atoms and N_e is the number of atoms evaporated onto the surface. Since $N_a = N_e - N_d$, where N_d is the number of atoms desorbed from the

surface, equation 2.18 can be rewritten as

$$C = 1 - \frac{N_d}{N_e} \quad (2.19)$$

The result is that the condensation coefficient decreases with increasing temperature as the number of desorbed atoms increases. This means that at a constant evaporation rate the deposition rate decreases. Under the conditions mentioned in chp. 2.4.2, about 0.75 monolayers per hour (ML/h) of Ag were deposited onto the substrate at 50 °C. At substrate temperatures of 75 °C and 100 °C the sticking coefficient decreases. As the evaporation time and therefore the total amount of evaporated material was kept constant, less material was deposited onto the organic films at these temperatures. The very low deposition rates used in this work represent an extreme condition for diffusion, because the number of atoms arriving at one point in time is small. Therefore, the probability that two atoms encounter each other is low and that way more atoms are likely to diffuse into the film or desorb. After the formation of first clusters, the probability to encounter an atom or a cluster within the average diffusion length increases and the probability to diffuse into the film decreases. Once a closed film is formed no further diffusion into the film should occur. If the metal diffusion can be understood and controlled for these extreme conditions, it should be possible to control the metal diffusion for all technologically relevant conditions, too.

2.6 Sputtering of Organic Crystalline Materials

Although the sputtering behavior of polymers is well established in the literature [56] the sputtering of organic crystalline materials in this low-energy range is not well-studied. Since the sputtering behavior of the organic films is, as mentioned before, very important for the analysis of the depth profiles (see chp. 2.7.1), it was necessary to examine the sputtering behavior of the two organic crystalline materials in detail. Knowledge of the sputtering behavior allows the correct interpretation of the depth profiles. If surface topography changes during sputtering, this would have to be taken into account when determining the depth resolution. Sputter experiments with Pc and DIP films show that the grain size and the surface topography are perfectly maintained within the resolution of the instrument. Simple constant-force contact-mode AFM measurements were performed for various sputter depths and rates, but no change in the topography was found. In fig. 2.18(a) the structure of an unsputtered Pc film is shown. At the higher

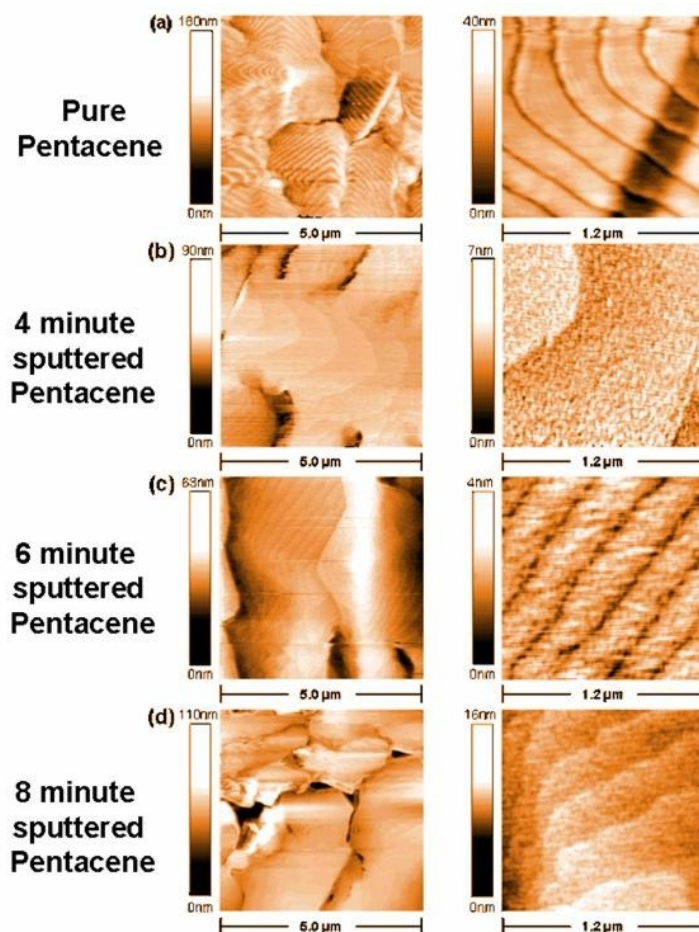


Figure 2.18: AFM images of (a) an unsputtered and (b-d) sputtered Pc film. Though the overall film topography is not influenced by sputtering a roughening of the surface on the molecular scale is observed.

magnification the terrace structure of the film can be clearly seen. During sputtering (see fig. 2.18(b-d)) the roughness of the surface increases slightly, however the terrace structure can still be seen. In fig. 2.19 (a) and (b) AFM images of an unsputtered and sputtered DIP film are shown respectively. As for the Pc film no change in the overall surface topography is observed. In these high resolution AFM images, the fingerprint of the sputter process becomes visible: an additional roughness on the molecular scale can be observed in the form of nanometer-deep and -wide holes. One large difference between the examined organic films and polymers are the much lower sputtering yields of the former, which are even much lower than the sputter yield of metals. Since the metal clusters would be sputtered faster than the surrounding organic film, an overestimation of metal penetration by preferential sputtering of metal clusters can hence be ruled out.

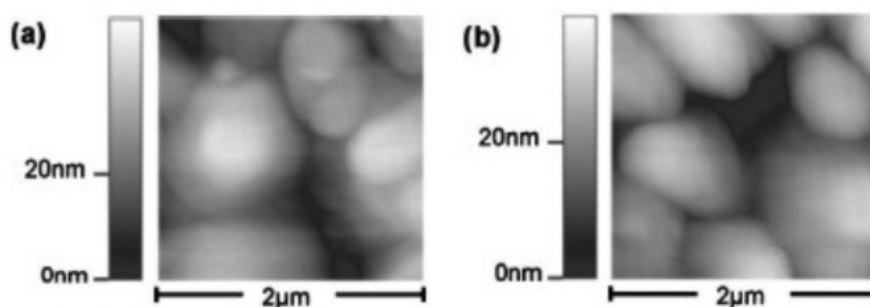


Figure 2.19: AFM images of (a) unspattered and (b) spattered diindenoperylene.

2.7 Noble Metal Diffusion in Diindenoperylene and Pentacene

Using the radiotracer method described in chp. 2.4.1 the diffusion of Ag and Au in Pc and DIP (see chp. 2.2.1) was studied. The obtained depth profiles are discussed in the following.

2.7.1 Ag Depth Profiles

As Ag diffusion in polymers is well studied and understood [41, 43, 46, 57–59], depth profiles for Ag diffusion in Pc and DIP were obtained. Comparison with the depth profiles of polymers will help to further the understanding of the nature of noble metals in these organic semiconductors.

2.7.1.1 General Features

About one monolayer of Ag + ^{110m}Ag was evaporated for 80 min. at 680 °C onto Pc and DIP thin films with thicknesses of 60 nm and 80 nm respectively. The substrate temperature during evaporation was 75 °C. After evaporation the samples were annealed for 120 min. at the same temperature. The depth profiles that were obtained are shown in fig. 2.20. The examined functional organic thin films did not only differ in their molecular structure (see fig. 2.2) but also in their microstructure. The inset of fig. 2.20 shows AFM images of the films. The grain size is about 1 μm for the DIP film and 0.3 μm for the Pc thin film. Even though the films are very different the depth profiles share some common features. A drop in metal concentration of three orders of magnitude within the first 5 nm was observed for both films. This indicates that most

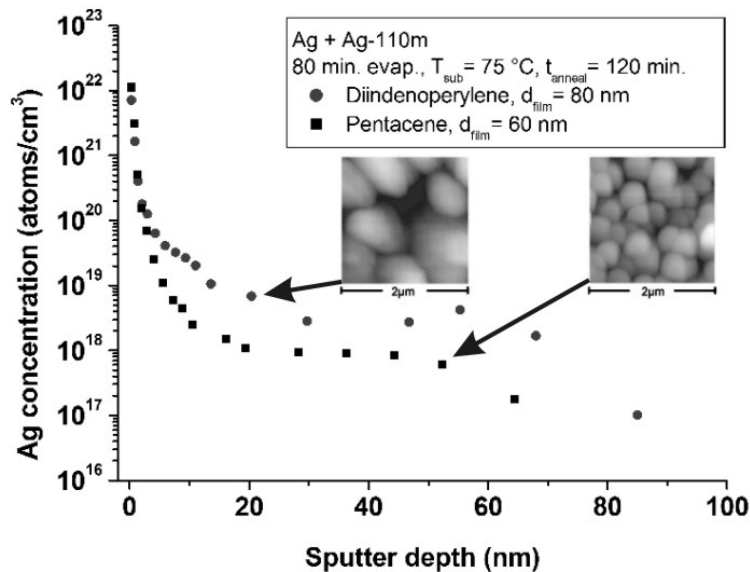


Figure 2.20: Depth Profiles for Ag diffusion in thin films of pentacene and diindenoperylene at a substrate temperature of $75\text{ }^{\circ}\text{C}$. For both materials, most metal atoms remain near the surface as the metal concentration drops by three orders of magnitude within the first 5 nm.

metal atoms ($>99\%$) remain on or near the surface, even though the total amount of material deposited was only about a monolayer. The metal concentration in the films drops to the level of the natural background at a depth of 60 nm for Pc and 80 nm for DIP which agrees very well with the corresponding film thicknesses. In addition to these common features some differences were observed. After the first initial drop, the metal concentration with respect to depth decreases more strongly in Pc than in DIP. At 20 nm the metal concentration in DIP is about one order of magnitude higher than in Pc. With increasing depth the difference in concentration decreases slightly but the Ag concentration in DIP is still much higher than in Pc. As the same amount of Ag was deposited onto both film, this indicates that Ag diffuses faster and more easily in DIP. Whether the differing crystal- or microstructure are the cause cannot be concluded here but will be discussed below.

In the DIP depth profile, around 40 nm a slight increase in activity is observed, which drops towards the natural background after reaching a maximum. This concentration peak can be explained by an accumulation of Ag atoms at the DIP/Si interface (agglomeration was already observed for Au/DIP (see chp. 2.3 and for other systems [60]), the surface topography, and the sputtering behavior of DIP. If Ag agglomeration at the

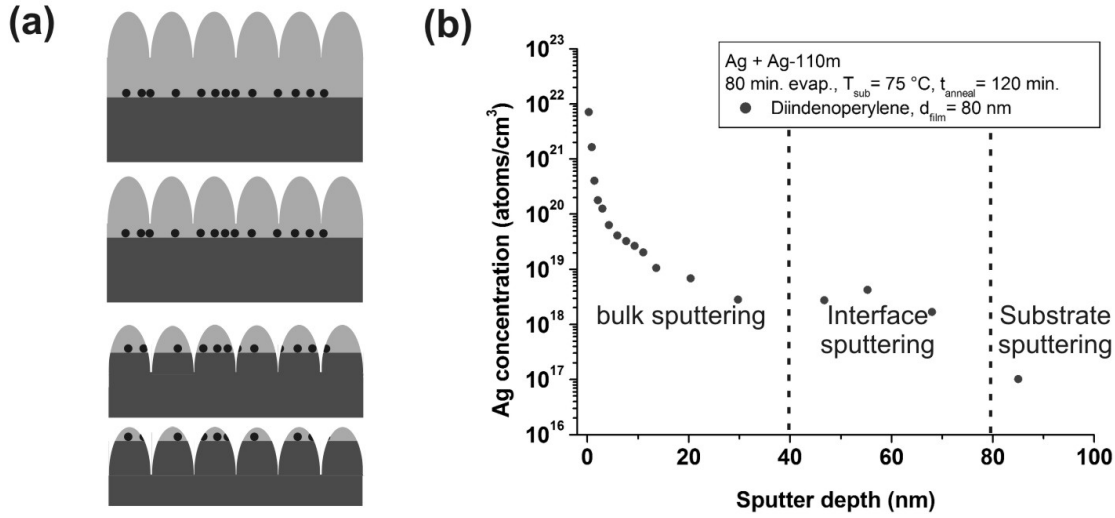


Figure 2.21: (a) Due to the surface topography of the film which is maintained during sputtering, some parts of the interface are sputtered prior to the rest of the interface. Material agglomerated at the interface will be sputtered likewise. (b) Due to non-uniform sputtering of the interface, three sputter regimes can be distinguished in the depth profile: after sputtering of the bulk of the DIP thin film, first parts of the interface are sputtered (≈ 40 nm). Due to clusters agglomerated at the interface the Ag concentration increases while more of the interface is sputtered. After 80 nm the complete DIP film was sputtered and the Ag concentration decreases to the natural background.

interface takes place, this should ideally lead to a sharp peak in the detected metal concentration at the depth of the interface. However, as mentioned in chp. 2.6, the natural grain structure and the surface topography of the DIP film with a maximum height difference of around 40 nm (see fig. 2.19) are maintained. That is why some parts of the interface are sputtered prior to other parts (see fig. 2.21(a)). The Ag atoms and clusters in these parts are also sputtered prior to the rest of the metal atoms. Instead of a sharp peak the metal concentration is smeared out over a depth range which correlates with the surface roughness of 40 nm due to the non-uniform sputtering of the interface.

2.7.1.2 Comparison with Ag Diffusion in TMC-PC

A comparison of a typical polymer profile, in this case trimethylcyclohexane polycarbonate (TMC-PC) (structure shown in fig. 2.22), and a DIP depth profile is shown in fig. 2.23 [46].

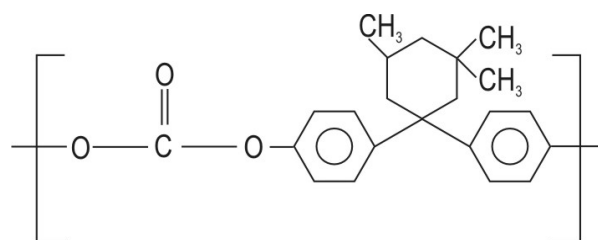


Figure 2.22: Chemical structure of trimethylcyclohexane polycarbonate (TMC-PC).

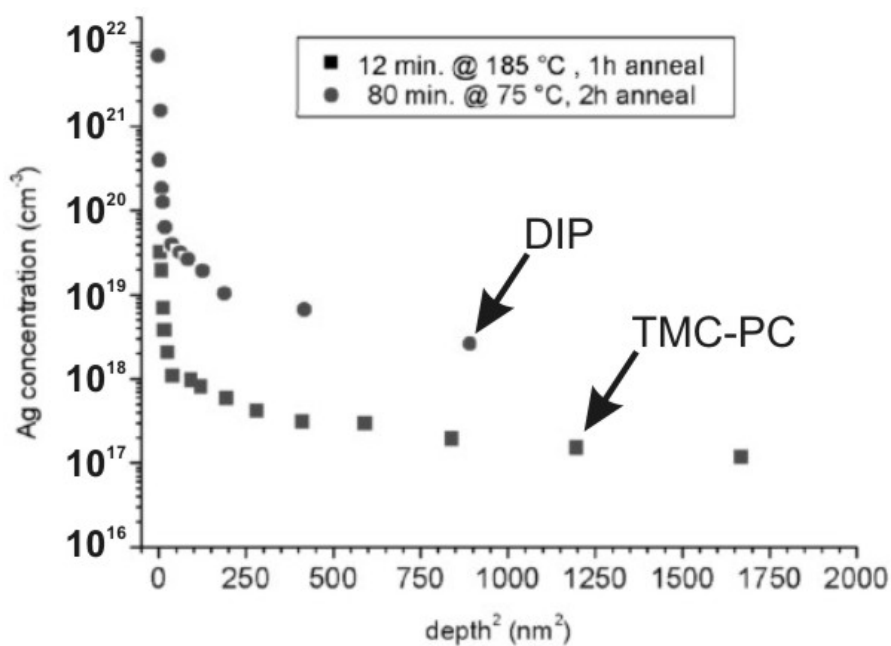


Figure 2.23: Comparison of depth profiles for Ag diffusion in DIP and TMC-PC (data for TMC-PC from [46]). Both depth profiles show the same basic features like the steep drop in metal concentration within the first few nanometers. This indicates that the diffusion behavior of noble metals is the same for both materials.

The diffusion of Ag in polymers is well-studied and the comparison of the depth profiles can provide a better understanding of the physical processes of metal diffusion in DIP. The profiles obtained for DIP are qualitatively very similar to the results obtained for TMC-PC, e.g., the first steep drop in concentration occurs over a very small depth range. In polymers, the cohesive energy of the organic matrix is smaller than that of the metal, and the interaction between metal and organic matrix is weak. Single atoms are very mobile in the polymer, but metal atoms encountering each other will form stable clusters which will impede further diffusion. The larger the clusters grow the stronger diffusion is impeded. This leads to effective immobilization of the metal atoms by clustering [42, 46]. In these terms, the drop in intensity with increasing sputter depth can be interpreted as the superposition of different diffusion rates of clusters of different size (see fig. 2.23).

This similarity of the depth profiles for the DIP and the TMC-PC indicates that the interplay of diffusion and aggregation in organic crystalline films and polymers is basically the same. This was expected as the cohesive energy of DIP and TMC-Pc is of the same order. The region with decreased slope is as pronounced as in polymers, suggesting a similar interpretation. In contrast to the thin DIP film (the organic crystalline film has the typical thickness used in OFET transistors of about 80 nm) the polymer film is much thicker (> 400 nm). Consequently, no agglomeration at the interface can be observed here.

2.7.1.3 Time Dependence

To further investigate the dynamics of noble metal diffusion in DIP, Ag + 110m Ag was deposited onto a DIP thin film with a thickness of 80 nm at 680 °C for 8 min. The resulting depth profile was compared to the depth profile obtained for 80 min. of tracer deposition (see fig. 2.24(a)). Increasing the evaporation time by a factor of ten leads to a metal concentration that is one order of magnitude higher, just as expected. Otherwise the general shape of the profiles is similar. With continuing film deposition the surface coverage with Ag increases as more than 99% of the Ag atoms is trapped on the surface. Due to the clusters growing on the surface, the probability of immobilization for an Ag atom diffusing across the surface increases. If the atoms diffuse across the surface before penetrating into the bulk, the relative metal concentration in the DIP film with respect to the concentration on the surface should be smaller for the longer deposition time. In fig. 2.24(b) the relative concentration with respect to the surface concentration is shown. As it can be seen, there is no difference in the depth profiles. That means either the metal coverage of half a monolayer is too low to impede the metal diffusion into the bulk,

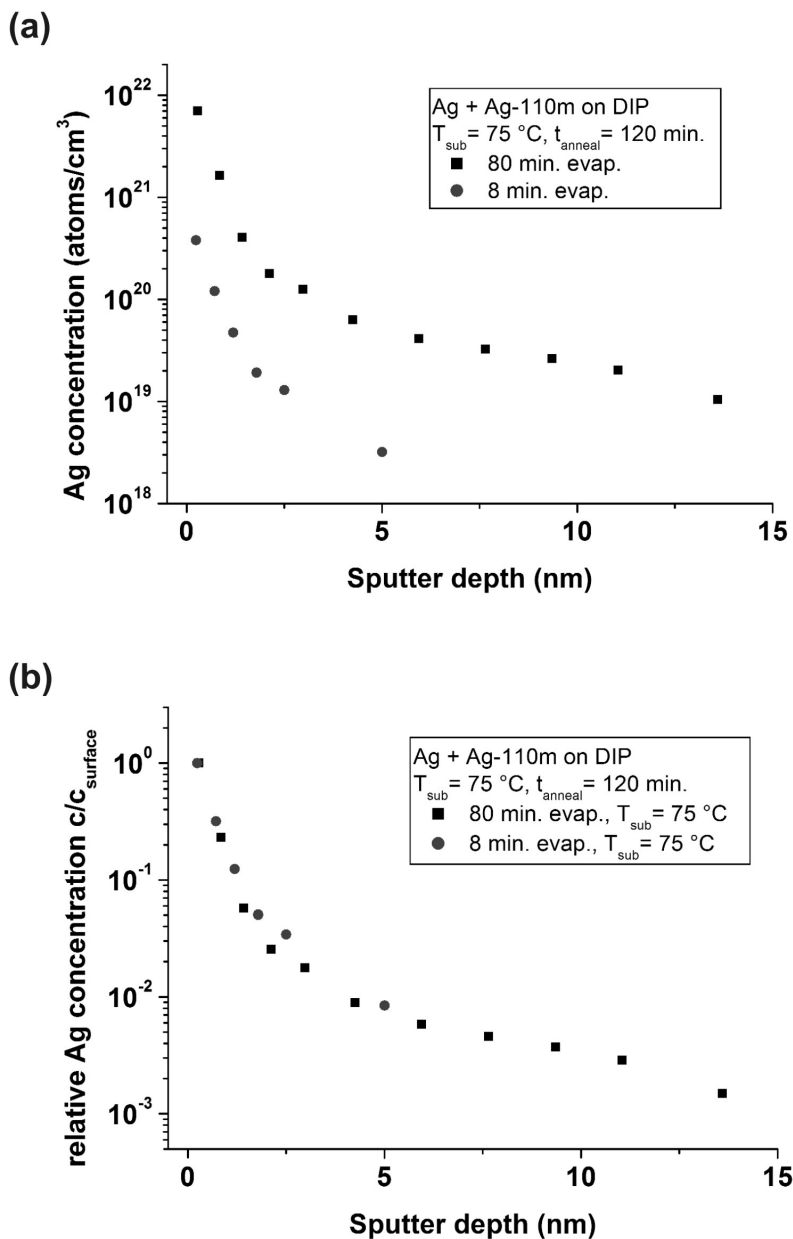


Figure 2.24: (a) Comparison of depth profiles obtained for 8 and 80 min. of tracer deposition. The general shape of the profiles is similar. Increasing the evaporation time by a factor of ten leads to an increase in the metal concentration by one order of magnitude. (b) Relative Ag concentration with respect to the surface concentration. No difference in the depth profiles is observed indicating that the different surface coverages do not influence the diffusion of metal atoms into the bulk.

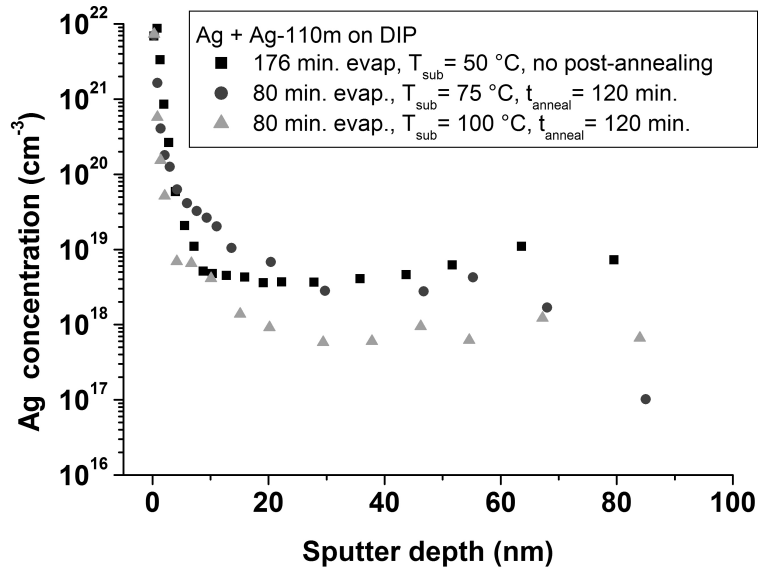


Figure 2.25: Temperature dependence of the Ag depth profiles obtained at substrate temperatures of 50 °C, 75 °C and 100 °C. After the initial drop in metal concentration, a region with a reduced negative slope is observed for all three temperatures. The negative slope decreases with increasing temperature, indicating increased metal diffusion with increasing temperature.

or the metal atoms do not diffuse across the surface but diffuse into the bulk almost directly.

2.7.1.4 Temperature Dependence

In order to examine the temperature dependence of the metal diffusion, Ag + ^{110m}Ag was deposited onto 80 nm thick DIP films at substrate temperatures of 50 °C, 75 °C and 100 °C. For the deposition at 75 °C and 100 °C the evaporation time was 80 min. and the samples were annealed for another 120 min. at the same temperature. For the sample kept at a temperature of 50 °C, the evaporation time was 176 min with no post-annealing treatment. Due to the longer evaporation time and the decreasing condensation coefficient with increasing temperature (see chp. 2.5), more metal is deposited onto this sample. For the sample with a substrate temperature of 50 °C, about one monolayer was deposited onto the film. Because of the Volmer-Weber growth of noble metals on the organic films, it is not a closed layer, but the film consists of clusters distributed over the surface. The resulting depth profiles are shown in fig. 2.25(a). All three DIP profiles have some general features in common. Within the first 5 nm the metal concentration

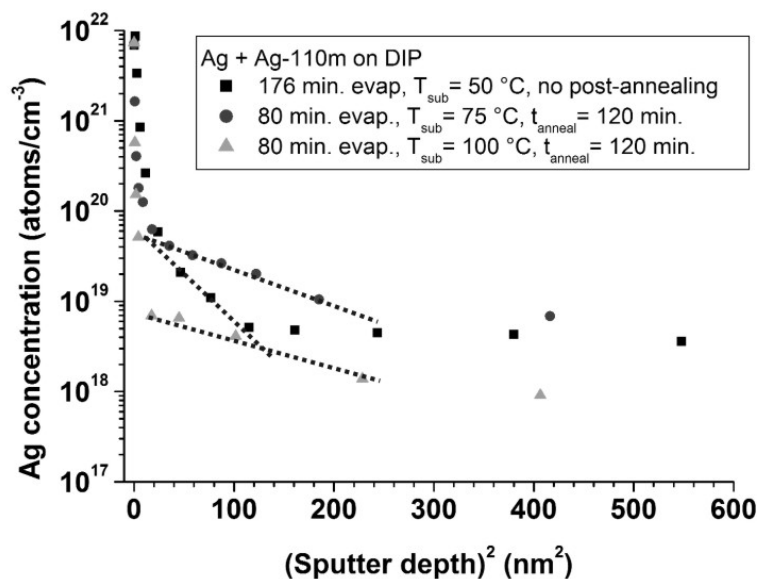


Figure 2.26: Metal concentration plotted against the square of the sputter depth for the samples shown in 2.25. In the region following the initial drop a linear dependence of the Ag concentration on the square of the sputter depth is observed. The slope of the linear fit decreases for increasing temperatures.

drops by three orders of magnitude, indicating that most metal atoms (>99%) remain on or near the surface, even though the total amount of material deposited was only about a monolayer (or less for 75 °C and 100 °C (see chp. 2.5)). Following this first drop there is a region with a drastically reduced negative slope which is proof of a decreasing metal concentration. Considering the large difference in the sputter yields of Ag and the DIP films discussed earlier, Ag clusters on the surface should not contribute to the Ag signal in this region, meaning that it originates from metal atoms diffusing into the film. For substrate temperatures of 75 °C and 100 °C, the change in the slope is more pronounced as compared to the depth profile obtained at 50 °C. This indicates increased diffusion of metal into the organic layer at higher temperatures. The absolute concentrations cannot be compared directly because the condensation coefficient of Ag on the organic film is expected to drop drastically at elevated temperatures (see chp. 2.5) [58].

In fig. 2.26 the Ag concentration for the three samples is plotted against the square of the sputter depth. In the region following the initial drop in Ag concentration, a linear relation between metal concentration and sputter depth is observed. With increasing substrate temperature the negative slope of the linear fit decreases. This indicates a faster diffusion at higher temperatures. It is not possible to calculate diffusivities from

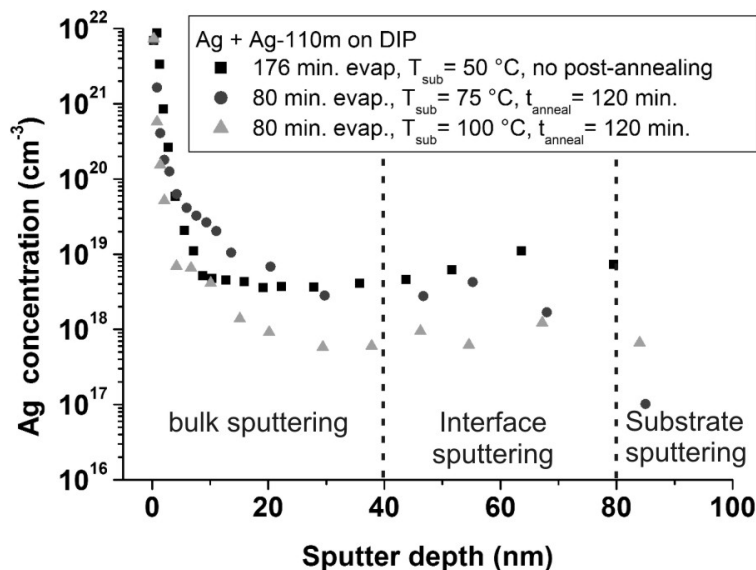


Figure 2.27: Accumulation at the interface is observed at all three temperatures. The broad peak in metal concentration results from the non-uniform sputtering of the interface (see chp. 2.7.1.1, fig. 2.21).

these slopes as the time t for diffusion is not known, since the diffusion process is stopped by agglomeration.

At all three temperatures, agglomeration at the interface was observed as can be seen from fig. 2.27.

2.7.1.5 Influence of the Microstructure

In chp. 2.7.1.1 it was found that Ag diffuses faster into DIP than Pc. The reason could either be the different crystal structure or the different microstructure, i.e. the smaller grain size and resulting higher grain boundary density. To study the influence of the microstructure of the organic film on noble metal diffusion, DIP films deposited at substrate temperatures of $-180\text{ }^{\circ}\text{C}$ and $60\text{ }^{\circ}\text{C}$ were examined. The different substrate temperatures resulted in different average grain sizes of the polycrystalline films. Details on the film structure are given in tab. 2.5, schematic diagrams and AFM images are shown in the inset in fig. 2.29. The film with the smaller grains has a higher grain boundary density. The radiotracer measurements can help to determine their influence on the diffusion. A higher grain boundary density might lead to more metal atoms diffusing deeper into the organic film, if they act as fast diffusion paths. On the other hand, the metal diffusion would decrease, if the grain boundaries act as trapping sites for

Sample	T_{sub}	d_{film}	d_{cry}	Rocking width
DIP01	60 °C	183 nm	183 nm	0.09°
DIP02	-180 °C	147 nm	76 nm	0.04°

Table 2.5: Two DIP films were deposited at different substrate temperatures T_{sub} . The resulting films allowed the examination of the microstructure's influence on the metal diffusion. The film deposited at a substrate temperature T_{sub} of 60 °C showed a crystallite size d_{cry} similar to the film thickness d_{film} . The crystallites of the film deposited at -180 °C are half as large as the film thickness. The rocking width of the XRD spectra is a measure for the structural order of the film. It is small for both films, indicating that both films are well ordered and most molecules are aligned in parallel.

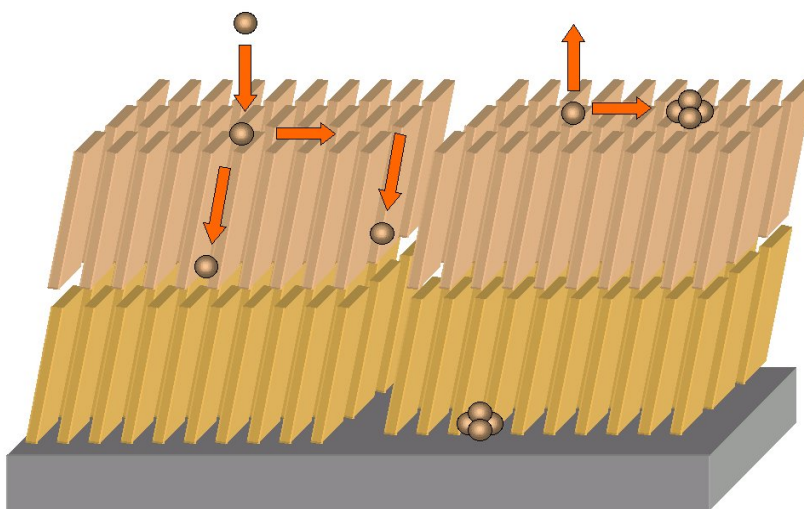


Figure 2.28: Schematic visualizing the possible influence of the film structure on the metal diffusion. Grain boundaries might either act as fast diffusion paths or act as trapping and nucleation sites for clusters.

noble metal atoms, i.e., nucleation site for clusters, (see fig. 2.28). If the bulk diffusion is dominating the grain boundary diffusion, the depth profiles should show no dependence on the microstructure. In fig. 2.29 the depth profiles obtained for Ag diffusion in the two different DIP films are shown. For the DIP film with the smaller crystallites, a larger metal concentration with respect to the depth is observed, indicating that grain boundaries act as fast diffusion paths.

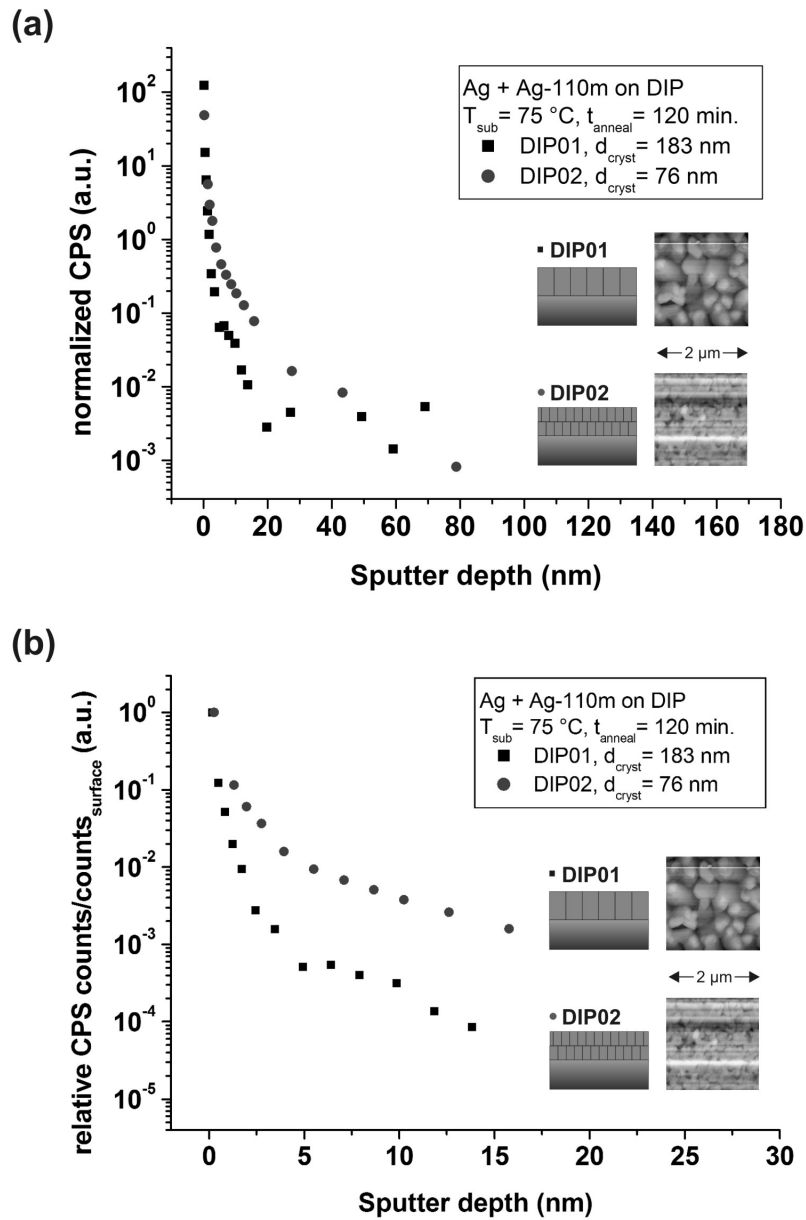


Figure 2.29: (a) Depth profiles for Ag diffusion in DIP films with differing microstructure. (b) The magnification of the first 15 nm shows the dependence of the metal diffusion on the film structure. In the film with the lower grain boundary density (DIP01 in inset), the relative Ag concentration with respect to the surface concentration is one order of magnitude lower as compared to the film with the higher grain boundary density (DIP02). This indicates that grain boundaries are acting as fast diffusion paths.

2.7.1.6 Chromium Diffusion Barrier

The comparison of the depth profiles for Ag diffusion in DIP and TMC-PC indicated a similar diffusion mechanism for polymers and organic crystalline materials. For TMC-PC, it was shown that a submonolayer of Cr can effectively block the diffusion of Ag into the polymer [46]. Since Cr is a transition metal, it is very reactive. The Cr atoms immediately react with the polymer and do not diffuse into the bulk. On the surface they act as nucleation centers for Ag atoms impinging onto and diffusing across the organic surface. As more Ag atoms are trapped on the surface, diffusion into the material is reduced.

If the diffusion mechanisms for DIP and TMC-PC are similar, a submonolayer of Cr should reduce Ag diffusion into the DIP film. In order to test the feasibility of a Cr barrier layer, a submonolayer of Cr with a nominal thickness of 0.1 nm was deposited onto the DIP film prior to evaporation of the Ag radiotracers. In fig. 2.30(a) the depth profiles for DIP films with and without Cr barrier are shown. In fig. 2.30(b) the data is normalized with respect to the activity on the surface of each sample. As for TMC-PC, the deposition of Cr leads to a reduced Ag concentration in the film. However, the reduction of the Ag diffusion is not as effective as observed for TMC-PC. Considering this together with the fact that an increasing surface coverage with Ag clusters had no effect on the metal diffusion (see chp. 2.7.1.3) indicates that the ratio of *surface diffusivity* D_{surface} and *bulk diffusivity* D_{bulk} is smaller for DIP as compared to TMC-PC.

In chp. 2.7.1.5 it was found that grain boundaries act as fast diffusion paths. While DIP and TMC-PC have the same cohesive energy they differ in their microstructure. DIP forms polycrystalline, well ordered films and TMC-PC films are amorphous. The existence of grain boundaries in DIP and their absence in TMC-PC can explain the difference in the ratios $D_{\text{surface}}/D_{\text{bulk}}$ and the varying effectiveness of Cr barrier layers because the grain boundaries act as fast diffusion paths in DIP. Submonolayers of Cr act as diffusion barriers on polymers because the Cr atoms dispersed across the surface act as nucleation centers for metals atoms which diffuse across the surface. If noble metal atoms diffuse right into the bulk along grain boundaries rather than to move across the surface first, dispersed Cr atoms will trap the metal atoms less effectively. While Cr can decrease metal diffusion, it still has to be examined whether the Cr barrier influences the electronic properties of the metal-organic interface.

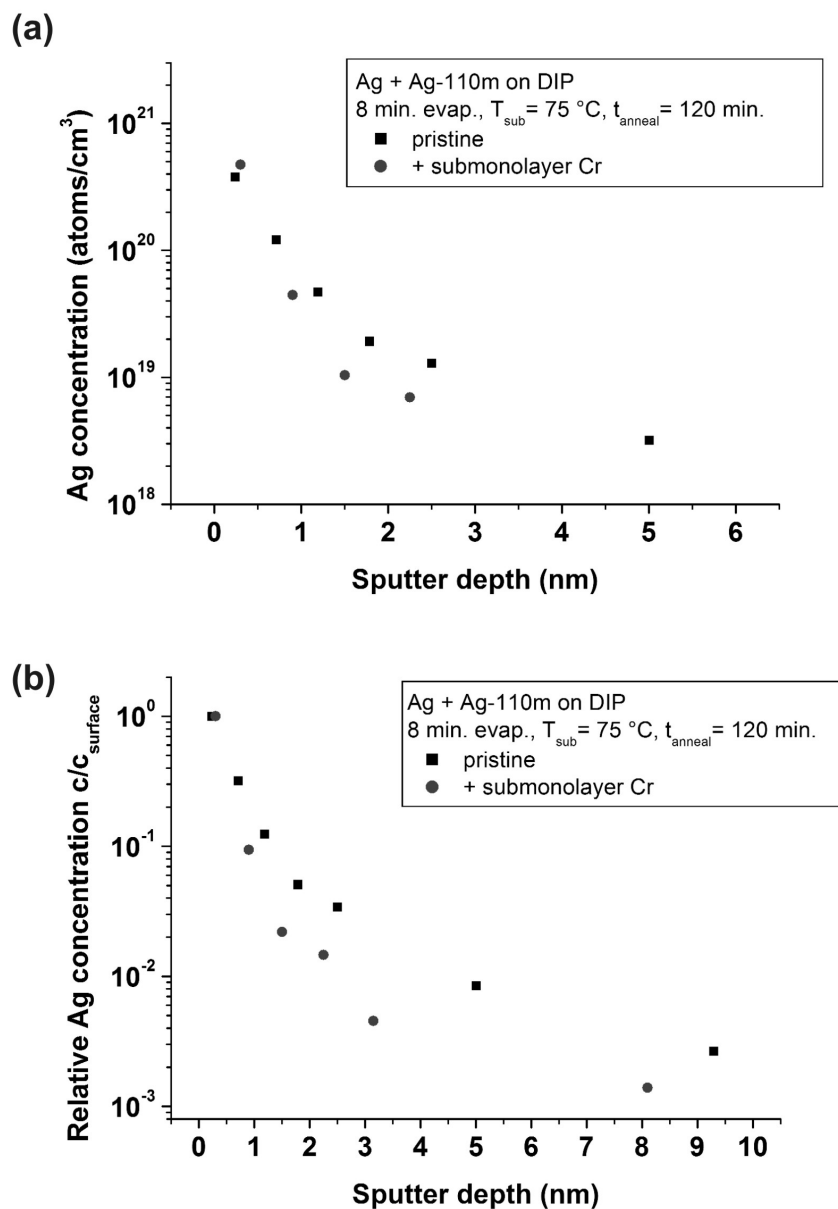


Figure 2.30: (a) Depth profiles for DIP films with and without Cr diffusion barrier. (b) The relative Ag concentration with respect to the surface concentration shows that a submonolayer of Cr reduces the metal concentration in the diindenoperylene films as compared to the untreated diindenoperylene film.

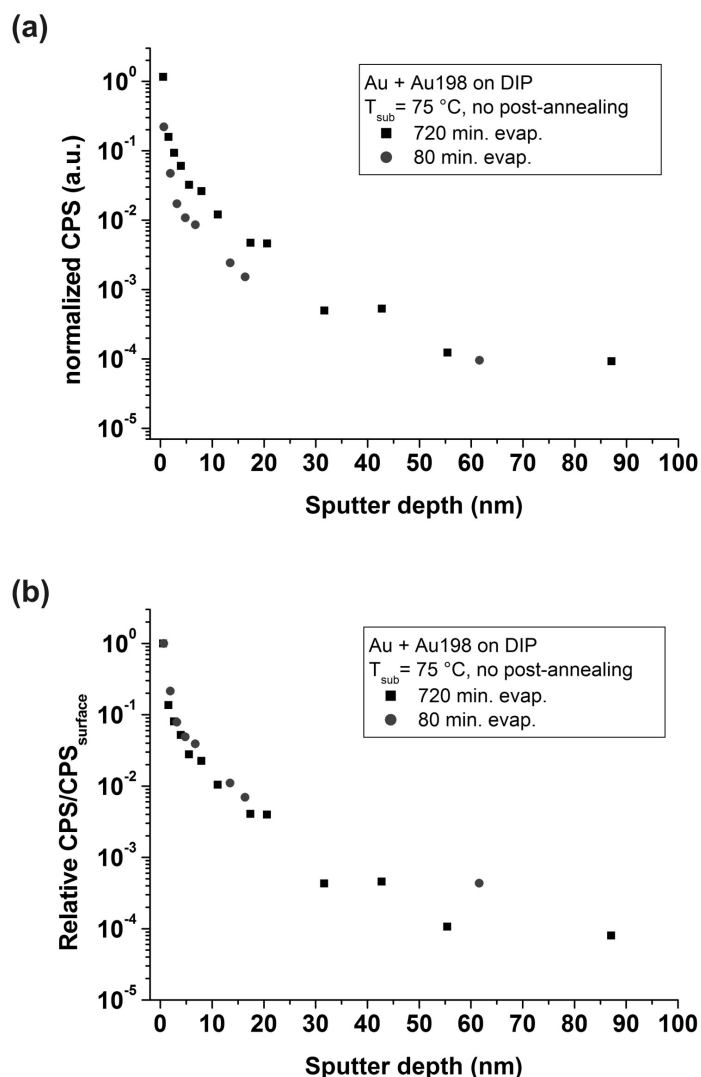


Figure 2.31: (a) Depth profiles for Au diffusion in DIP for 80 and 720 min. of tracer evaporation. The obtained depth profiles show the same characteristic features observed for the Ag depth profiles. (b) Relative CPS with respect to the CPS on the surface. As for the Ag diffusion no time dependence is observed.

2.7.2 Au Depth Profiles

As mentioned in the introduction, Au is used for metallization of Pc- and DIP-TFTs due to the good alignment of the Au work function and the HOMO level of the organic semiconductors. Depth profiles for Au + ^{198}Au evaporated at 860°C for 80 and 720 min. is shown in fig. 2.31(a). A comparison with the depth profiles obtained for Ag diffusion will show whether the diffusion process is comparable for the two noble metals. As for

Ag, a drop in the *counts per second* (CPS) is observed in the first 5 nm followed by a region of decreasing negative slope. In fig. 2.31(b) the relative CPS with respect to the surface are plotted against the sputter depth. No time dependence is observed. The low CPS imply that the surface coverage is too low to impede metal diffusion by trapping in clusters.

2.8 Correlation between Metal Diffusion and Device Properties of OFETs

The radiotracer measurements provided details on metal diffusion into the organic semiconductor and the mechanism of the interface formation and the resulting structure. Metal atoms diffuse into the organic film where they are immobilized by cluster formation. Increased diffusion at low deposition rates and/or high substrate temperatures leads to formation of a rough smeared-out interface consisting of clusters of different sizes located near the former surface of the organic semiconductor. As mentioned in chp. 2.2.2.2, this interface should be treated as an additional layer that can influence the energy alignment at the interface. For fabrication of actual devices it is important to understand how these structures influence the electronic properties of the interface and thus the device. Charge carrier injection might be either enhanced or impeded depending on how the energy alignment and the injection barriers are influenced (see equations 2.4 and 2.5 in chp. 2.2.2.2). Comparison of the current-voltage curves of contacts formed by slow and fast metal deposition combined with the information of the interface derived from the radiotracer depth profiles can further the understanding of the influence of the interfacial structure on the device performance.

2.8.1 Sample Preparation

Three Au contact arrays with a thickness of 50 nm were deposited onto a 40 nm Pc film (see chp. 2.4.7). The Pc film was provided by Dr. Jens Pflaum from the University of Stuttgart. It was grown on a Si wafer with a native oxide layer. Two contact arrays were deposited at a substrate temperature of 75 °C. The first contact array (Array 1 in the following) was deposited at a rate of 0.8 nm/min. For the second set of contacts (Array 2 in the following) first a submonolayer of Au was deposited very slowly (< 1 ML/h) on top of the Pc film in order to allow strong diffusion (see fig. 2.20). Afterwards, the contacts were deposited at the same rate of 0.8 nm/min as the first set. The third array

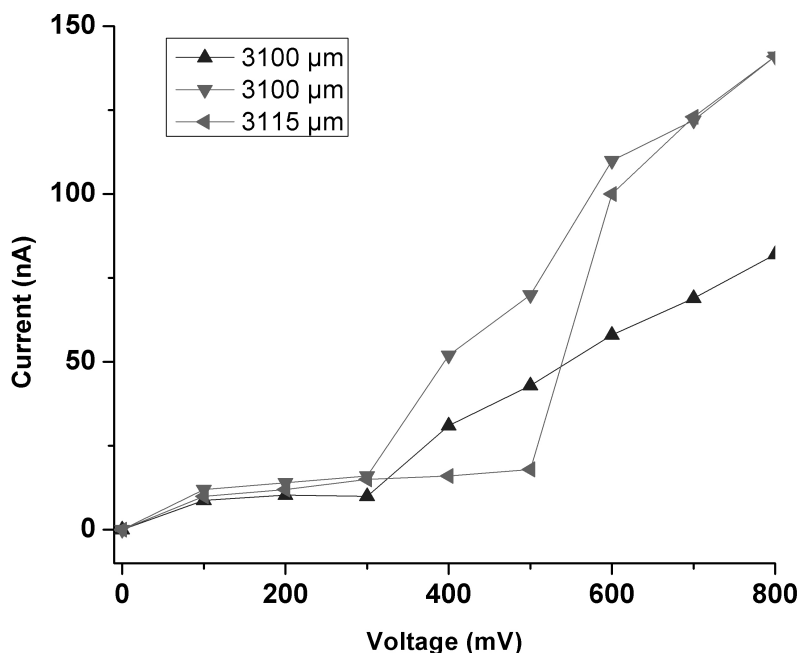


Figure 2.32: Transition in the I-V curves of the contacts of Array 2 with a channel length varying between 3100 and 3115 μm . Below the switching voltage, the current is almost zero and independent of the applied voltage. Above a critical voltage the current increases with increasing voltage. The switching is reversible if the applied voltage is not increased above 2 V.

(Array 3 in the following) was deposited at 0.8 nm/min with the substrate at room temperature, corresponding to the profile for DIP in fig. 2.25.

2.8.2 Electronic Characterization

For the electronic characterization of the Au contacts voltages between 0 and 6 V were applied between the contacts. Different channel length could be measured by selecting different contact pads (see fig. 2.15). The resulting currents were in the order of 0- 10^4 nA. Higher voltages were not used as the resulting currents could damage the contact between the metal and the organic semiconductor.

For the I-V curves of the contacts a switching process was observed for voltages mostly in the mV-range. This transition was observed for all three interface structures. In fig. 2.32 the transition in the I-V curves for contacts of Array 2 are shown. Below the switching voltage the current is very small (< 20 nA) and shows no dependence on the

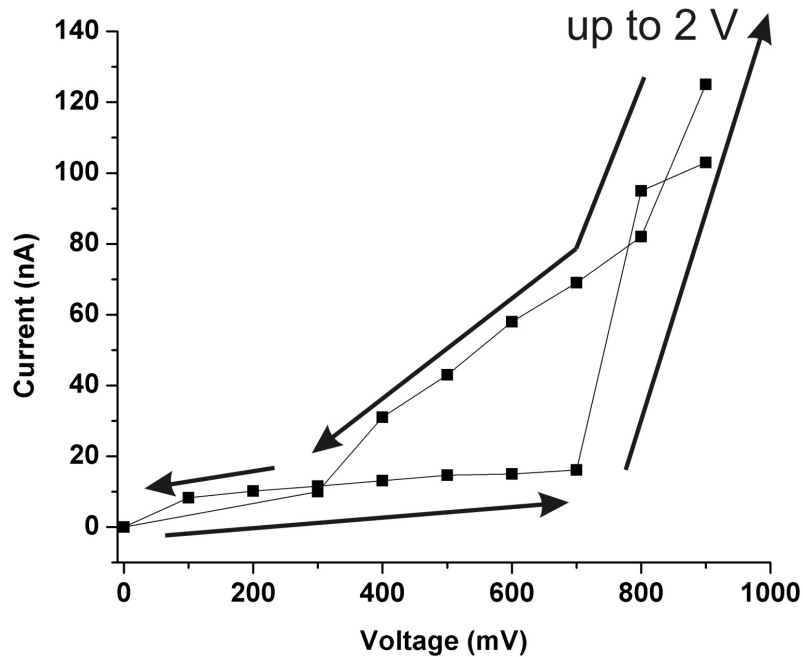


Figure 2.33: The graph shows the I-V curve of a contact of Array 2 with a channel length of $3100 \mu\text{m}$. A switching is observed as the voltage is increased above 700 mV . It is not observed anymore after the applied voltage was raised above 2 V . In that case, the current continuously decreases to zero when the voltage is decreased again.

voltage. Above the switching voltage there is a sharp increase in the current and it continues to increase with increasing voltage.

This switching process is reversible if only small voltages below 2 V are applied. If the voltage is increased up to 2 V and then ramped down to 0 V again, the switching is not as pronounced as before and the switching voltage changed from 700 mV to 300 mV (see fig. 2.33).

A similar effect is observed in nanocomposites and nanowires [61, 62]. In plasma polymers that contain silver nanoparticles a switching process was observed if the voltage was varied from -2 V to $+2 \text{ V}$. With each cycle the switching was less pronounced and the switching voltage (the so-called threshold voltage) decreased [62]. While still several mechanisms are discussed as origin for the switching, it seems to be clearly linked to the microstructure as it is only observed for nanocomposites near percolation [62]. Therefore, the switching observed for the Au contacts may be related to the morphology of the interface. Due to diffusion during contact deposition the interface is rough with

dispersed metal clusters near the interface. If this interface region is comparable to a percolated network of clusters in a nanocomposite, the observed switching process could result. The large variation in the switching voltage and the slope of the I-V curve upon switching are attributed to differences in the individual contacts.

As already small voltages seem to permanently change the electronic properties of the contact, the maximum voltage was limited to 6 V so that the influence of the metal diffusion on the contact properties could be examined and not the changes due to high voltages and currents. Furthermore, since the native oxide layer of the Si wafer only has a thickness of about 2 nm, no gate voltage was applied in order to avoid an electrical breakthrough of the insulating layer.

2.8.2.1 General Features

Fig. 2.34(a) and (b) show the I-V curves for Array 1 and Array 2 respectively. The I-V curves of Array 3 are shown in fig. 2.35. All the curves have a similar shape but the values of the I-V curves of different contacts within the same array can deviate from each other by about 50 %. This might prove that the formation of reproducible top contacts is extremely difficult even if the contacts are formed on the same film under the same conditions. Within each array, the channel length between the contacts does not seem to have an influence on the I-V curve. This indicates that the contact resistance between the Au pad and the Pc film is dominating the overall resistance so that the channel resistance can be neglected.

But even with this large deviation within the same array, the comparison of the I-V curves of the two different contact arrays in fig. 2.36 shows that the extent of the metal diffusion has a clear influence on the contact properties. The arrays were formed on the same Pc film, the only difference being the increased metal penetration for Array 2. For this array the contact resistance appears to be larger and charge carrier injection is impeded as the maximum current injected is smaller as compared to Array 1. Therefore, the rough interface formed by increased diffusion results in inferior contacts as the charge carrier injection is impeded. However, the contacts of Array 3 feature the smoothest interface but its I-V curves are comparable to Array 2 and inferior to those of Array 1. This shows that a certain interface roughness could be favorable as the alignment of the Au contacts and the HOMO of the organic semiconductor is improved and the injection barrier decreased. But if the roughness exceeds a certain limit the injection barrier is increased again.

In fig. 2.34(a) it is also shown that almost no current is measured if the organic

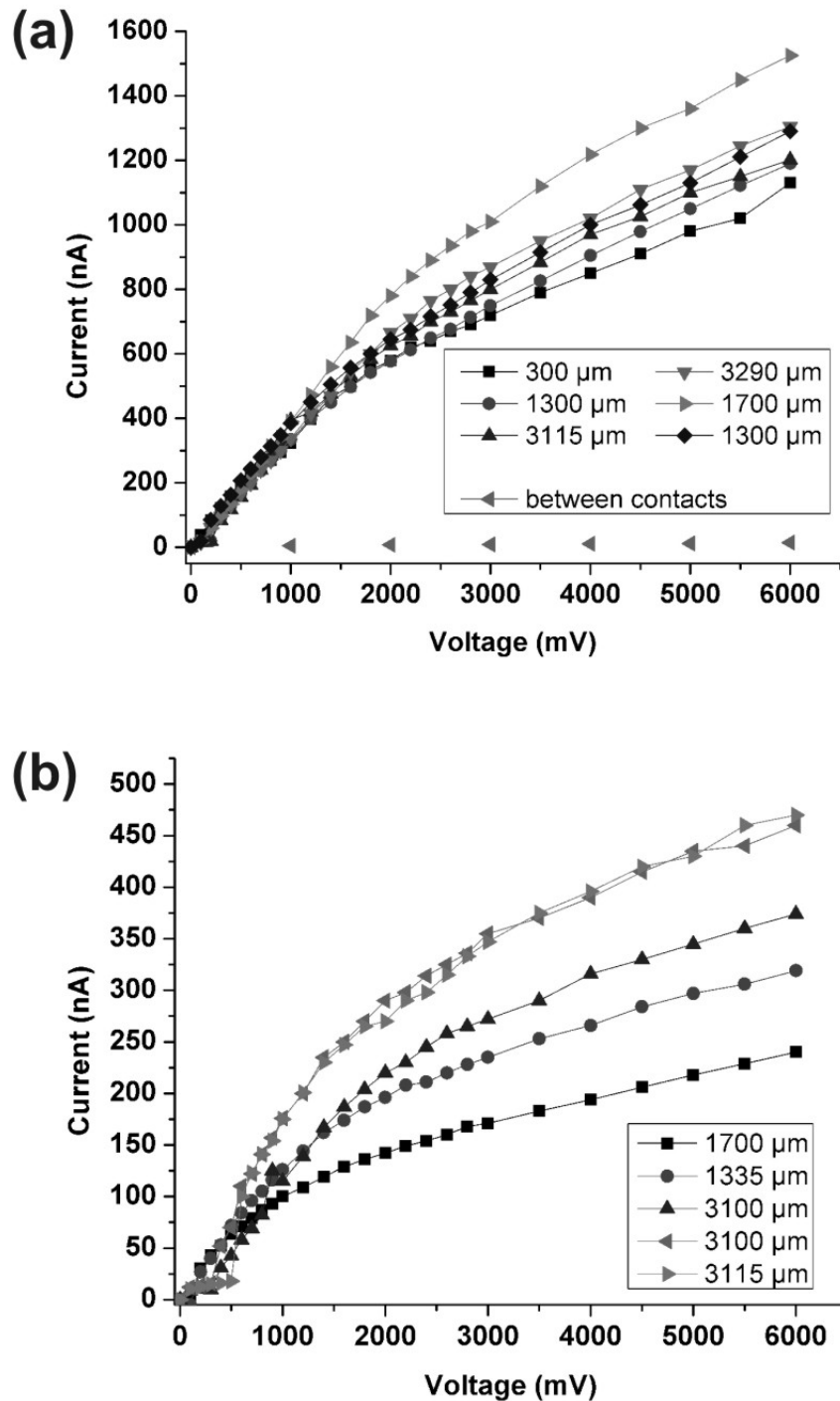


Figure 2.34: Current-voltages dependence of the Au contacts deposited with (a) high (Array 1) and (b) low (Array 2) deposition rates at a substrate temperature of 75°C . The general shape of the I-V curves is similar for both contact arrays. The deviation within one array might be caused by differences in the individual top contacts. The channel length does not seem to have an influence on the I-V curves.

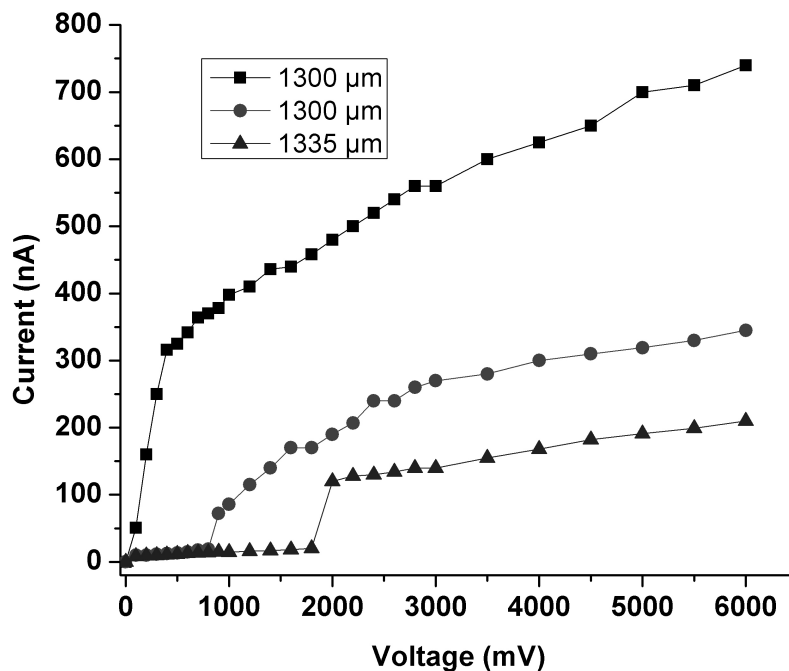


Figure 2.35: Current-voltages dependence of the Au contacts deposited with a high deposition rate with the substrate being at room temperature. The general shape of the I-V curves is similar to that of Array 1 and 2.

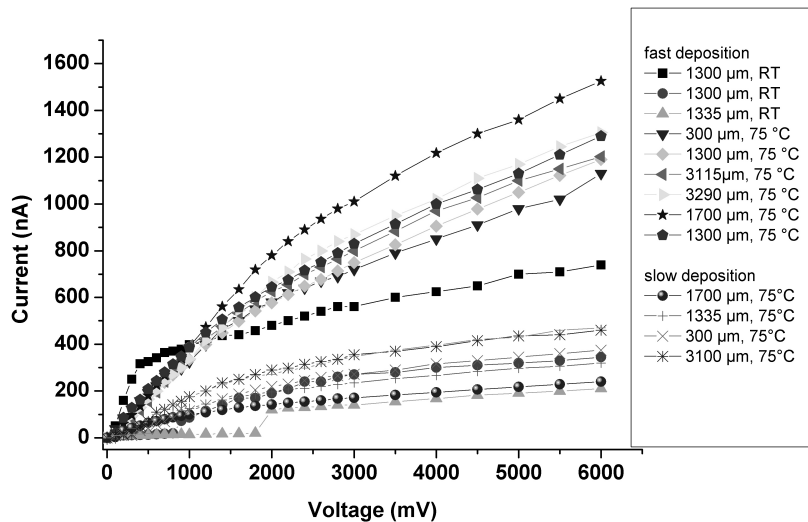


Figure 2.36: Comparison of I-V curves of different contacts. The contacts deposited at 75 °C at the higher deposition rate showed the best I-V characteristics of the three different contact arrays.

semiconductor is contacted directly. Under illumination from a bright light source a current of about 3 μA was measured for the contacts of Array 1 and 2 independent of the applied voltage or the deposition conditions of the contacts. This proves that in fact the organic semiconductor is conducting the measured current and not the doped Si wafer underneath the film. Furthermore, this shows that the low intrinsic charge carrier concentration and the charge injection barrier are responsible for the much smaller currents measured without illumination.

For Array 3 currents in the order of 25 μA were measured. This indicates that the alignment of metal work function and HOMO is optimized for extraction of the charge carriers from the organic semiconductor and that the current without illumination is limited by the injection.

2.8.2.2 Aging

Another interesting effect that was only observed for the contacts of Array 2 was a change of the I-V curve after 24 hours. The I-V curves of the contacts of Array 2 showed currents that were much smaller than the currents measured for the contacts of Array 1. After storage in ambient air for 24 hours, the I-V curves of Array 2 were comparable to the curves of Array 1 (see fig. 2.37). Since the I-V curves of Array 1 did not change upon exposure to air this improvement cannot be caused by simple oxidation of the interface as this would occur for both arrays. This change of the I-V characteristic may rather reflect room temperature diffusion in the organic material which was also observed in polymers [46, 63]. In this case, single atoms and small clusters might diffuse back to the interface where they are incorporated into the closed layer. This process would smoothen the interface and its morphology would be similar to an interface that was formed by fast deposition.

2.8.2.3 Asymmetric Behaviour

The results presented above indicate that different interface morphologies can optimize the injection or extraction of charge carriers. Therefore, it might be possible to optimize the performance of an organic semiconductor by deposition of two contacts with different interfaces. This approach was tested by deposition of one contact similar to those in Array 1 (best injection behavior) and one similar to Array 3 (best extraction). In fig. 2.38 the resulting I-V curves are shown. In one direction a very high current is measured. If the current direction is reversed the resulting current is much smaller. In the high-current direction the photo-induced current was 25 μA and in the low-current direction

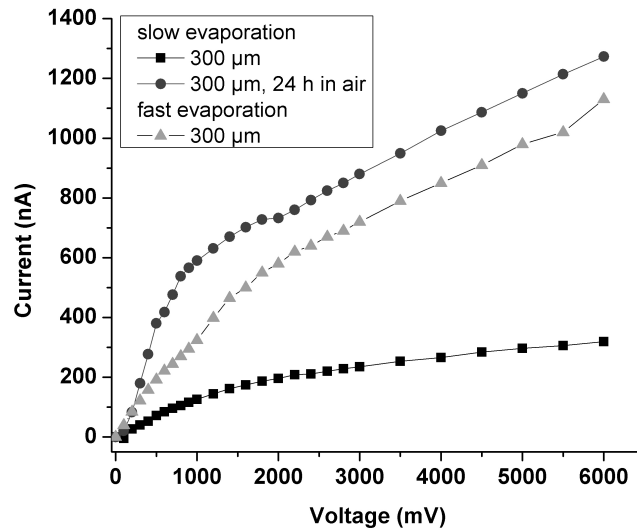


Figure 2.37: After storage in air for 24 hours the I-V characteristic of a contact from Array 2 changes considerably. Its I-V curve is now comparable to that of a contact of Array 1 with the same channel length. This might indicate the presence of room temperature diffusion as the clusters of the rough surface of Array 2 diffuse back to the interface. This process would result in a smoother surface comparable to that of Array 1.

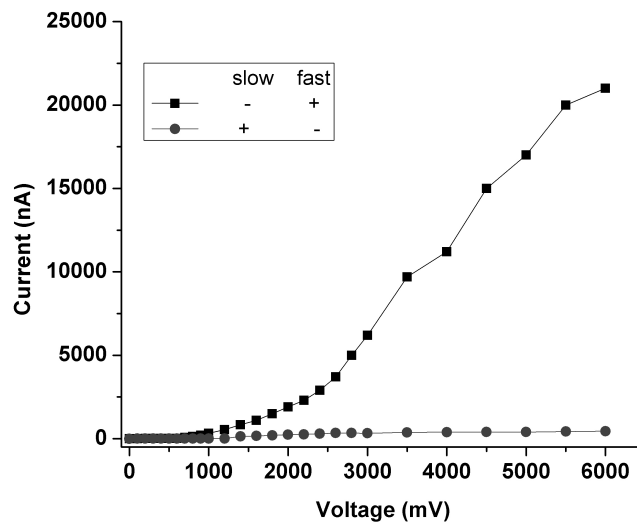


Figure 2.38: I-V curves of an asymmetric contact. Depending on the direction of the current flow, the resulting I-V curves differ greatly from each other. This indicates that one contact is optimized for charge carrier injection while the other is optimized for extraction of charge carriers.

the photo-current was only 3 μm . These results proof that of the two contacts one is indeed optimized for injection and the other for extraction of charge carriers. This optimization is not possible for bottom contact devices as the organic semiconductor is deposited on top of the metal and no diffusion occurs and the structure of the interface cannot be varied for individual contacts.

2.9 Summary and Outlook

With the investigation of noble metal diffusion in organic semiconducting thin films, the functional part of an OFET, one important challenge in the field of organic electronics was addressed: the metallization of organic semiconductors. It was found that most metal atoms remain on or near the surface of the organic thin film, but a small fraction of metal atoms diffuses into the organic thin film. In the case of diindenoperylene, a small fraction of metal atoms diffuses through the entire film and accumulates at the interface between organic film and substrate. The accumulation of even small amounts of metal atoms at the buried interface between organic semiconductor thin film and gate dielectric might cause serious changes in the device performance.

Comparison with radiotracer diffusion measurements in the polymer trimethylcyclohexane polycarbonate showed similar diffusion behavior of Ag in both films. While one material is amorphous and the other is polycrystalline, both their cohesive energies are smaller than that of the metal. The interaction between the noble metal atoms and the organic molecules is only weak, allowing single metal atoms to be highly mobile in the organic film. Immobilization occurs by cluster formation between two or more noble metal atoms. Once a closed metal layer is formed on top of the organic film, no further diffusion should occur, as the high cohesive energy of the metal keeps atoms from leaving the metal layer.

Grain boundaries were identified as fast diffusion paths. For DIP films with different grain boundary densities it was found that more metal diffuses into the organic film with the higher grain boundary density. Therefore, organic semiconducting thin films with large grain sizes are not only favorable due to their higher charge carrier mobilities but also because metal diffusion is less pronounced. The fast diffusion along these grain boundaries was identified as one reason why Cr barrier layers, which have been successfully applied to amorphous polymers, are less efficient in reducing Ag diffusion into organic semiconductors. Whether these submonolayers influence the electronic properties of the metal-organic interface has still to be examined.

The combined results of the radiotracer measurements and first electrical measurements of contacts allowed to identify the influence of the metal diffusion and structure of the interface on the electronic properties of the interface which is of importance for the device performance.

I-V measurements of Au contacts on pentacene films showed large differences in the behavior of different contacts depending not only on the deposition parameters but also the individual contacts. A sudden change in the I-V characteristics in the mV-range was observed. At larger voltage a clear difference in the characteristics of contacts which were deposited under different conditions was observed. While slight diffusion might improve the charge injection at the interface the results indicate indicate that the roughening of the interface due to increased metal diffusion leads to the formation of inferior contacts as the contact resistance increases and charge carrier injection seems to be impeded.

For rough interfaces the I-V curves changed after 24 h and were then comparable with the I-V curves of the contacts that were deposited at a higher deposition rate. This might indicate that diffusion occurs at room temperature so that single atoms and small clusters diffuse back to the interface decreasing its roughness. It was shown that combining two contacts with different interfaces might optimize the device performance as the energy alignment at the interfaces of the contacts either optimize charge carrier injection or extraction. Such an optimization by control of the interface roughness would not be possible for bottom-contact devices as no diffusion occurs.

The depth profiles provide proof of the exceptional resolution of this technique because the signal decreases in parts by even more than one order of magnitude per nanometer in this first region. This leads to an observed resolution in the submonolayer regime, which means about a nanometer in this case. Due to its high resolution and extreme sensitivity the radiotracer technique is well suited to study metal diffusion in organic thin films as was demonstrated in this chapter for crystalline materials and was shown for polymers before [46].

There are other metal/organic systems of great technological importance for which radiotracer measurements can help to improve the device development and performance. The first example is closely related to organic field effect transistors. The metallization of organic semiconductors is not only important for the fabrication of OFETs but also for organic solar cells, where metal is also deposited on top of organic semiconductors and diffusion might be a problem.

But metal diffusion in organic materials is not an issue limited to organic electronics but also arises in inorganic semiconductor technology. In the so-called dual damascene

processes for the fabrication of modern Cu/low-k interconnects, Cu is deposited onto low-k dielectrics. A diffusion barrier is required to prevent Cu diffusion through the interlayer dielectric and into the silicon [6]. With continuing scaling of integrated circuits the barrier layer thickness decreases from 4.8 nm at the 65 nm technology node to 3.3 nm for the 45 nm node [64]. Especially for porous ultra low-k dielectrics ($\kappa < 2.5$), deposition of an effective diffusion barrier is extremely difficult. Up to the present day, no technique is known that is suitable for the evaluation of the reliability of these very thin barrier layers [6]. Radiotracer diffusion measurements might be the ideal tool to evaluate the reliability of Cu diffusion barrier layers on porous low-k dielectrics. The sensitivity of the radiotracer technique would allow the detection of even smallest amounts of Cu as they can degrade the transistor performance.

Metal diffusion during metallization is only one of several challenges faced in the field of organic thin film field effect transistors. Other functional issues include good on/off ratios, a low subthreshold swing, the susceptibility of the organic semiconductors to degradation due to oxygen and moisture and control of the threshold voltage. The latter two problems are addressed in the next two chapters.

2.10 Author's Related Publications

- [1] M. Scharnberg, J. Hu, J. Kanzow, K. Rätzke, R. Adelung, F. Faupel, C. Pannemann, U. Hilleringmann, S. Meyer, and J. Pflaum, *Radiotracer measurements as a sensitive tool for the detection of metal penetration in molecular-based organic electronics*, Appl. Phys. Lett. 86, 024104 (2005)
- [2] M. Scharnberg, J. Hu, J. Kanzow, K. Rätzke, R. Adelung, F. Faupel, and J. Pflaum, *Ag-diffusion in the organic semiconductor diindenoperylene*, Defects and Diffusion Forum 237-240, 993 (2005)
- [3] M. Scharnberg, J. Kanzow, K. Rätzke, R. Adelung, S. Meyer, J. Pflaum, and F. Faupel, *Radiotracer diffusion measurements of noble metal atoms in semiconducting organic films*, Organic Thin-Film Electronics, edited by A.C. Arias, N. Tessler, L. Burgi, and J.A. Emerson (Mater. Res. Soc. Symp. Proc. 871E, Warrendale, PA, 2005), I6.31 (2005)

3 PTFE Capping Layers for Organic Field Effect Transistors

3.1 Introduction

With the interface formation between metal contacts and organic semiconductor, one important challenge in the fabrication and realization of OFETs was addressed in the last chapter. But as mentioned at the end of the last chapter, more challenges are faced in the field of OFETs. One other critical issue is the susceptibility of many organic semiconductors to degradation of the device performance due to exposure to oxygen and moisture. Therefore, this important issue must be addressed in order to successfully implement these organic materials in working FETs. A possible solution for this problem is the deposition of a capping layer on top of the semiconducting thin film.

An ideal capping layer should not only protect the organic film from oxygen and moisture but should also preserve all the advantages of organic electronics like low weight and mechanical flexibility. Degradation by moisture and oxygen is also known to affect organic light emitting diodes [65] and transparent flexible barrier layers have been reported [66–69]. In order to evaluate if these barrier layers can also be implemented with organic field effect transistors it is first necessary to review these barrier layers and their fabrication in detail in the following subchapter.

3.2 Multilayer Barriers for Organic Light Emitting Diodes

For OLEDs degradation of the organic layer poses a problem, but the main concern is the oxidation of the top electrode. It is formed by a low work function metal which is very reactive and prone to oxidation. The oxidation of the electrode leads to a loss in luminescence and therefore a diffusion barrier for oxygen and water molecules is required.

Al_2O_3 is a good barrier material [66], however the barrier performance of a single layer is limited by the substrate roughness and the presence of intrinsic defects like pinholes in the film which act as fast diffusion paths [66]. Increasing the thickness of the barrier layer leads to an improvement of its performance due to increased coverage of the rough substrate and filling of pinholes but no further significant improvement is observed above a critical thickness of 10-30 nm due to propagation of grain boundary defects [66, 70].

In order to improve the barrier properties, actual barriers consist of a multilayer structure which is formed by alternating films of an acrylic polymer and an inorganic oxide [66]. The polymer film is deposited by flash evaporation of the monomers and curing of the film on the substrate.

First, a 1 μm -thick polymer film is deposited onto the substrate by the *polymer multilayer* (PML) process. The liquid monomers form a non-conformal film that smoothes the surface and decreases the surface roughness. On this planar surface, a ceramic oxide film like Al_2O_3 (≈ 25 nm) is deposited by vacuum deposition. It serves as actual barrier layer blocking the permeation of moisture and oxygen and is followed by a thin film of the acrylic polymer (≈ 240 nm) [69]. The polymer film sandwiched between two ceramic layers decouples defects like pinholes in the individual inorganic films and thereby improves the barrier properties [66]. By alternating deposition of Al_2O_3 layers and polymer thin films a multilayer structure with excellent barrier properties is formed. However, this multilayer process suffers from several severe drawbacks:

- The vacuum equipment required for the flash evaporation of the monomer is complex and expensive [71] compared to standard UHV equipment.
- Curing of the film during processing is required.
- Undesired polymerization within the evaporator leads to a continuous and variable reduction in deposition rate during a deposition run [72, 73].
- The process is not compatible with central hub or in-line batch processing because there are no instant on/off PML sources [72, 73].

This last point is possibly the largest drawback of this technique since batch processing and central hub processing are common fabrication procedures. Especially the fabrication of FETs requires many different processing steps as processes like printing are not realized yet. Thus, a batch process for the deposition of the barrier layers should be favorable.

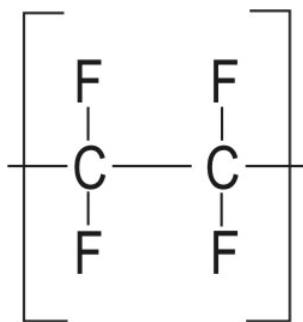


Figure 3.1: Chemical Structure of polytetrafluoroethylene (PTFE).

So far, no PML-based barrier layers have been reported for OFETs so far, probably because of the drawbacks mentioned before. Therefore, it might be of interest to examine other materials and multilayer systems for their suitability as barriers. The capping layer of an OFET does not have to be transparent for visible light as it is required for OLEDs. The material should rather be suitable for vacuum deposition as the inorganic layer is also deposited under UHV conditions and in the case of small molecule semiconductors like Pc and DIP the complete FET is produced in an UHV chamber. Since the surface roughness of the Pc and DIP films is much lower as for the substrates of *flexible organic light emitting diodes* (FOLEDs), non-conformal coverage of the film should not be critical. Also the adhesion between the organic film and the ceramic oxide film should be good.

Since Al_2O_3 is deposited by sputtering, it would be favourable to use an organic film that can be also be deposited by sputtering as the same infrastructure, e.g., Ar gas can be used. Polytetrafluoroethylene (PTFE) films can be deposited by sputtering (see chp. 3.3.1 for details about sputtering) [74, 75] and are hydrophobic making them an obvious choice for a capping layer against moisture. The chemical structure is shown in fig. 3.1. Alternating sputtering of PTFE and Al_2O_3 would allow the deposition of multilayer barriers by a process that is compatible to in-batch processing. The formation of Al-F compounds at the interface should also lead to good adhesion between the organic and inorganic layer.

Furthermore, the sputter-deposited PTFE films are also highly cross-linked [76], so that oxygen diffusion might be blocked too. Thus, the organic film would not only improve the barrier performance by decoupling of defects in the ceramic oxide layers but might also serve as barrier layer itself.

To test their suitability as capping layer it is necessary to test if PTFE films can act as barrier against oxygen and moisture.

For evaluation of the barrier properties, PTFE thin films were sputtered onto working

BOC-OTFTs. The device performance was measured before and after capping for several month and compared to uncapped devices. Then, the change in the electronic properties (esp. the threshold voltage) of the device or absence of it is a measure for the suitability of sputter-deposited PTFE thin films.

The work presented in this chapter was realized in cooperation with the Department EIM-E/Sensor Technology of the University of Paderborn, which produced the OTFT microstructures and performed the electronic characterization.

3.3 Methods

3.3.1 PTFE Deposition

The PTFE films were deposited using RF sputtering from a magnetron source. The basic principles of the sputter deposition process used to deposit the PTFE films are partly comparable to the ion sputtering described in chp. 2.4.3. Here, also ions are used to sputter material from a substrate. However, the ions are not generated in an ion source but the plasma is created directly in the UHV chamber. In a typical *direct current* (DC) planar diode setup for sputtering, the substrate consisting of the material that is to be deposited (*target*), is placed on the cathode. It is bombarded with positive ions from the plasma and caused by the interactions described in chp. 2.4.3 atoms and molecules are sputtered from the target in a cosine distribution. A part of the material is deposited as thin film onto the sample, which is placed on the anode.

DC sputtering cannot be used for deposition of insulators like PTFE since bombardment with positive ions would lead to charging of the target which causes plasma extinction. This problem can be avoided by using a *radio frequency* (RF) field instead of a DC field. The positive charge created by the ion bombardment is compensated by electrons from the plasma when the RF field changes orientation.

Magnetron sputtering is a variation of the sputtering setup. A typical planar magnetron is depicted in fig. 3.2. A magnetic field is used to force the electrons that are emitted from the target into a trajectory as shown in fig. 3.2. This trajectory greatly prolongs their escape path to the anode meaning that each electron undergoes more ionization events. Therefore, one of the advantages of magnetron sputtering is the reduced minimum pressure for sustaining the plasma that is required (typically 10^{-3} mbar) in comparison to DC sputtering (typically 10^{-2} mbar). This furthermore results in higher deposition rates and lower operation voltages (about 500 V as compared to 1-2 kV).

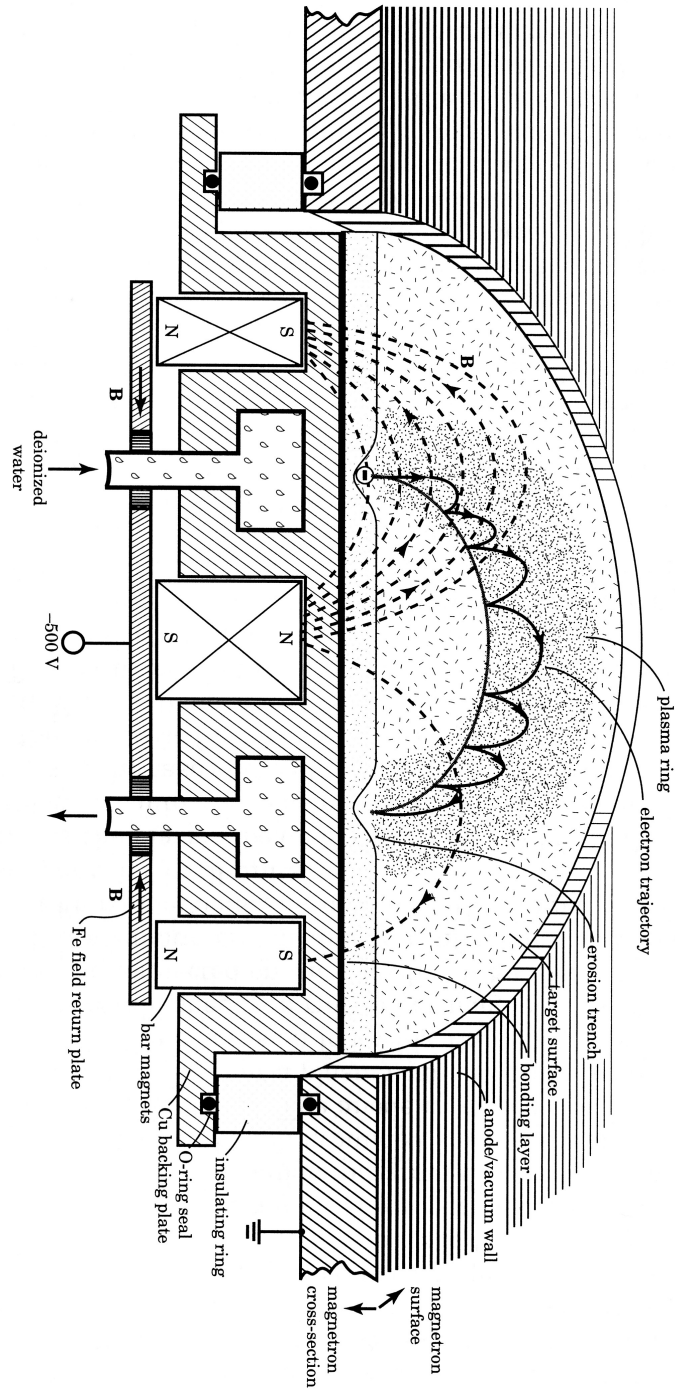


Figure 3.2: Schematic of a planar magnetron (from [77]). Electrons emitted from the target are forced into a trajectory by a magnetic field that prolongs their escape path. Due to the increased number of ionization events per electron the operating pressure and operating voltage are reduced.

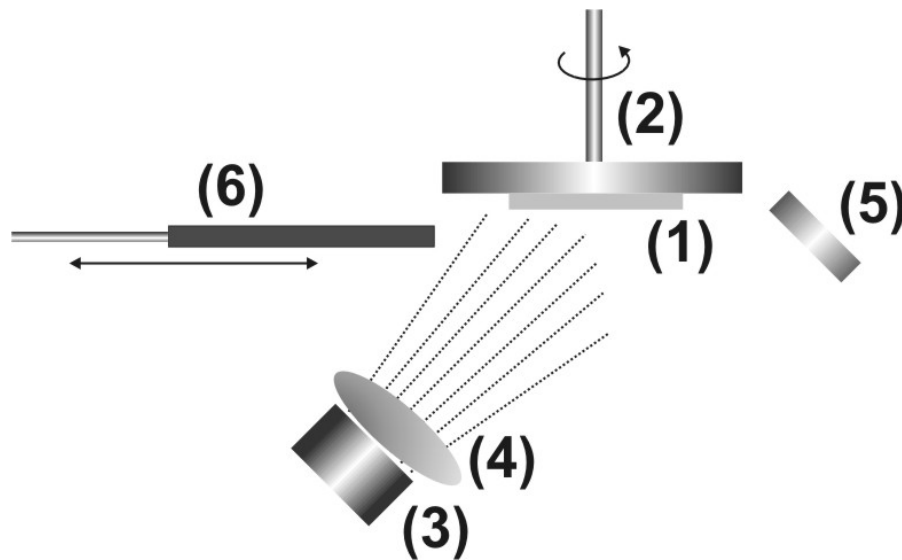


Figure 3.3: Schematic of the UHV chamber used for sputter deposition of the PTFE thin films. The sample (1) is fixed to a rotatable sample holder (2). Above the magnetron sputter source (3) an argon plasma (4) is created. The sputtered material is deposited onto the sample. A QCM (5) was used to measure the sputter rate during film deposition. A shutter (6) protects the sample during ignition and stabilization of the plasma.

Magnetron sputtering is also compatible with RF sputtering for deposition of insulating films.

The UHV chamber used for deposition of the PTFE films is shown in fig. 3.3. An ION 'X-2"UHV 9109 magnetron from *Thin Film Consulting* with a PTFE target with a diameter of 50.8 mm was installed in the chamber. Argon was used as process gas for plasma generation. Its flow was controlled by a mass flow controller.

3.3.2 Determination of the Deposition Rate

A *quartz crystal microbalance* (QCM) was used to determine the deposition rate during magnetron sputtering of the PTFE films in order to control the final film thickness. In a QCM a quartz crystal is placed between two metal electrodes. When a voltage is applied between the electrodes the electric field causes a mechanical strain in the quartz because of the converse piezoelectric effect. If an AC voltage is used the crystal vibrates at its resonance frequency. If a film is deposited on the surface of the crystal, this frequency shifts. According to Sauerbey's equation [78] this shift in the oscillation frequency is given by

$$\Delta f = -C_f \Delta m \quad (3.1)$$

where Δf is the change in the oscillation frequency, C_f is the sensitivity factor of the crystal and Δm the change in mass. The film thickness can be then be calculated by

$$d_f = \frac{\Delta m}{\rho_f} \quad (3.2)$$

where d_f is the film thickness and ρ is the density of the film. A more complex expression than equation 3.2 has to be considered for thick films ($\Delta f > 2\%$) [34, 79]. Since the QCM measurements were only used to control the sputter process and since the actual film thickness was verified by profilometer measurements (see chp. 3.3.3), this dependence will not be discussed in detail. For a more detailed review see [49].

Since the condensation coefficient (see chp. 2.5) for the QCM and the sample may be different and since the material is deposited in a cosine distribution with the QCM located to the side of the sample, it is necessary to perform calibration experiments in order to determine the tooling factor for the setup. The tooling factor is given by

$$t = \frac{d_f^s}{d_f^q} \quad (3.3)$$

where d_f^s is the film thickness actually deposited onto the sample and d_f^q is the film thickness determined by the QCM measurements. The tooling factor is determined by calibration measurements prior to the actual film deposition and was found to be 3 for the given UHV chamber.

3.3.3 Determination of the Film Thickness

In order to verify the QCM data, the thickness of the deposited films was determined in a way that is similar to the method described in chp. 2.4.5 for determination of the sputter depth. In this case, a piece of a silicon wafer is placed next to the samples during film deposition. Afterwards, a part of the film is removed using the sharp tip of a scalpel. The depth of the scratch is equal to the film thickness since the silicon is harder than the stainless steel of the scalpel and is therefore not scratched while the soft and brittle Teflon film is easily removed. The depth is measured using the Dektak 8000 profilometer as described in chp. 2.4.5.

3.3.4 Electronic Characterization

To determine the degradation of the transistors over time the *drain-source current* I_{DS} in dependence on the *drain-source voltage* V_{DS} was measured at a *gate-source voltage* V_{GS} of -40 V directly before and after capping layer deposition and again after one, two, three and four months of operation. All measurements were performed in a shielded metal box without illumination using a HP 4145A Semiconductor Parameter Analyzer from Hewlett-Packard.

The threshold voltage was determined according to the IEEE specification for OFETs [80]. At the point of the maximum slope of the $\sqrt{I_{DS}}-V_{GS}$ -characteristic curve a straight line is fitted. The intercept point with the abscissa ($\sqrt{I_{DS}}=0$) is taken as value of V_{th} [81].

3.4 PTFE Capping Layers for Pc Field Effect Transistors

Before the results of the degradation measurements obtained for the aforementioned samples are discussed, the mechanisms leading to the degradation of the Pc-FETs are briefly introduced and the sample preparation is described.

3.4.1 Degradation Mechanisms

As pointed out in the introduction, exposure to oxygen and humidity can cause degradation of organic electronic devices. In Pc, oxygen is reacting with the middle ring of the molecule (see fig. 2.2(a)) forming pentacenequinone (see fig. 3.4) [82]. These molecules act as scattering and trapping centers for charge carriers in the OFET [83], degrading the performance properties like on-current, on-off ratio and a shift of the threshold volt-

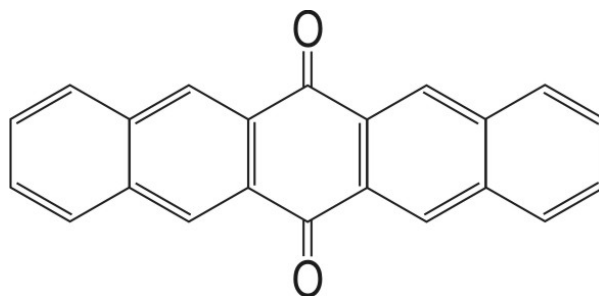


Figure 3.4: Chemical structure of pentacenequinone.

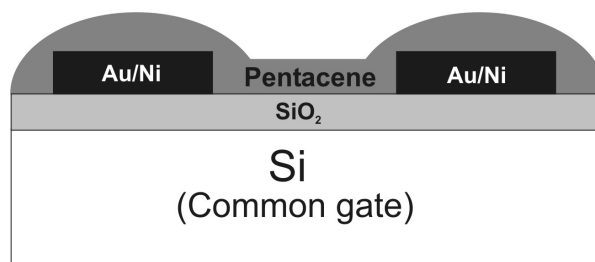


Figure 3.5: Schematic of a pentacene BOC-TFT used for the capping layer experiments. A highly doped silicon wafer served as common gate for all transistors. A pentacene thin film served as semiconductor and was deposited onto the Au contacts and the SiO_2 gate oxide. The schematic is not drawn to scale.

age in positive direction [84]. The incorporation of pentacenquinone into the molecular structure disturbs the π -electron system impeding charge carrier transport. In addition, new molecular orbitals are created, which act as trapping sites for charge carriers.

Water molecules from the ambient air are incorporated during the transistor's operation. The electrical field in the transistor initiates dissociation of the molecules and these ions attach to the grain boundaries of the polycrystalline pentacene film and to the interface between dielectric and pentacene [83]. In both cases the additional charges of the ions create potential barriers. At the grain boundaries these potential barriers lead to a reduction in the current flowing through the channel as they reduce the charge carrier mobility. Accumulation at the interface causes a shift of the threshold voltage in negative direction. For uncapped pentacene OTFTs an overall shift of the threshold voltage into negative directions is observed [85]. This indicates that the degradation due to dissociation of water molecules is dominating the aging process.

3.4.2 Sample Preparation

3.4.2.1 Pentacene Field Effect Transistor

The OFETs for the capping layer experiments were produced at the University of Paderborn. The BOC-TFT structures (see fig. 3.5) were realized on highly doped p-type silicon substrates that served as common gate for the transistors. The gate oxide was a SiO_2 layer with a thickness of 150 nm, that was grown by thermal oxidation of the Si substrate at 960 °C. Patterning of the source and drain contacts was done by UV contact photolithography and mask lift-off in acetone. Afterwards an 8 nm thick nickel layer was deposited as adhesion promoter followed by deposition of the 80 nm Au contacts.

As semiconductor a 30 nm thick Pc film was deposited by thermal evaporation (see fig. 3.5).

The fabricated FET had an interdigital structure with a width W of 46.8 μm , a length of 20 μm and a W/L ratio of 23,400. The interdigital structure allowed to realize large currents in the order of 10^{-3} A. These large currents made it possible to measure a large change in the current due to degradation even several month into the experiment in progress.

3.4.2.2 PTFE Capping Layer

The PTFE film was deposited by magnetron sputtering as described in chp. 3.3.1. The base pressure was 10^{-7} mbar, during the experiment the pressure increased to 10^{-3} mbar. A power of 50 W was chosen and the resulting deposition rate that was measured with a QCM was 21 nm/min. The nominal deposited film thickness was 1.5 μm , which was verified as described in chp. 3.3.3.

3.4.3 Degradation Measurements

The results of the electronic characterization are shown in fig. 3.6 and tab. 3.1. The initial on-current I_{DS} was -6.8 mA and the threshold voltage V_{th} was 12.3 V. After deposition of the PTFE capping layer, I_{DS} changed to -6.2 mA and V_{th} to 13.2 V. This small change of 0.9 V directly after deposition (which can be attributed to aging during shipping from Paderborn to Kiel and back) proves that it is feasible to deposit an additional layer by sputtering without damaging the FET and degrading its performance.

The transistor structure was measured periodically every 30 days. After a strong decrease of I_{DS} within the first 60 days, the decrease slowed down significantly for the next 60 days. A comparable transistor without capping layer showed a constant decrease in I_{DS} of one order of magnitude per 90 days and a shift of V_{th} in negative direction [85]. The comparison of the results for the capped and uncapped FET indicates that the PTFE capping layer cannot completely prevent aging of the transistor but can at least reduce the degradation. The shift in the threshold voltage towards positive values for the capped FET suggests that the degradation process is dominated by the oxygen mechanism (see chp. 3.4.1), while the aging of the uncapped FET is dominated by the influence of humidity as the threshold voltage shifts to more negative values. Both degradation mechanisms take place in the uncapped FET. But the degradation due to dissociated water molecules seems to have a larger impact on the device performance than aging due to formation of pentacenequinone, since the overall shift of V_{th} is towards

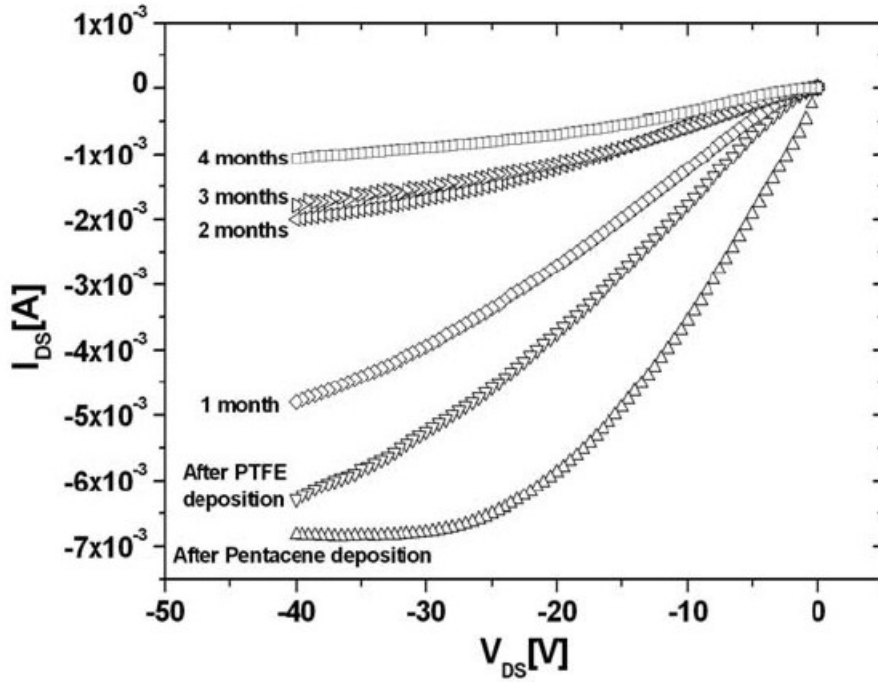


Figure 3.6: $I_{DS} - V_{DS}$ characteristics at $-40 V_{GS}$ of an OTFT with a W/L ratio of 23,400 before and after encapsulation with a PTFE thin film (from [86]). While degradation of I_{DS} is strongly reduced as compared to uncapped TFT over time, it is still significant, so that a single PTFE film cannot act as capping layer but has to be combined with a ceramic oxide in a multilayer barrier. The change in the $I-V$ curve after deposition of the PTFE layer as compared to the original curve is attributed to aging during shipping not to deposition of the PTFE film onto the OTFT.

Time	max. I_{DS}	V_{th}
before PTFE	-6.8 mA	12.3 V
after PTFE	-6.2 mA	13.2 V
30 days	-4.7 mA	18.2 V
60 days	-1.9 mA	n.a.
90 days	-1.7 mA	n.a.
120 days	-1.1 mA	23.2 V

Table 3.1: Values of I_{DS} and V_{th} during the aging experiments for the capped transistors. I_{DS} and V_{th} of uncapped transistors decrease by one order of magnitude every three months.

negative values. Because of its hydrophobic nature the PTFE capping layer protects the underlying Pc film from water molecules of the ambient air. However, the cross-linking of the sputtered film is not dense enough to prevent oxygen permeation through the film.

3.5 Summary and Outlook

In this chapter it was shown that capping layers of sputter-deposited PTFE can protect Pc-films from moisture while degradation caused by oxygen was not prevented as the threshold voltage shifted to more positive values over time and current and charge carrier mobility decreased.

While PTFE alone cannot act as a protective barrier, it might be deposited alternately with Al_2O_3 as part of a multi-layer barrier. Such a barrier layer system would also be of interest for the implementation in OLEDs as the sputter deposition of PTFE would avoid the problems arising from film deposition by PML.

While PTFE films are not fully transparent for visible light, these barriers might not be used for capping of flexible substrates as the color of the PTFE films might influence the colour of the OLED. However, OLEDs fabricated on *indium-tin-oxide* (ITO) only need a protective diffusion barrier on the back-side, so that transparency of the barrier is not critical. Therefore, fabrication and testing of sputter-deposited PTFE/ Al_2O_3 is very interesting for future projects.

Pc films have to be protected from exposure to solvents. It was shown that solutions used during processing of AMLCDs can influence the grain boundary state and grain state of the pentacene film modifying the device performance [87]. It was also demonstrated that films which can be deposited solvent-less can act as barrier layer between Pc films and photoresists [88]. This barrier film can protect the Pc from the solvent used for deposition of the photoresist. That might allow the patterning of Pc by standard photolithography processes. Since they are insoluble in most solvents, sputtered PTFE films might act as a barrier layer against solvents allowing to deposit spin-on oxygen barriers or photoresists on top of Pc films, acting as barrier against water molecules at the same time.

While being part of a barrier layer, Teflon-based polymers might have the advantage of serving as a multifunctional organic thin film in OFETs. One example for such a multifunctional organic thin film is introduced in the next chapter: a Teflon-based capping layer which is further functionalized for tuning of the threshold voltage and for inverting the operating mode of the transistor from enhancement to depletion at $V_{GS} = 0$ V.

3.6 Author's Related Publications

- [1] C. Pannemann, T. Diekmann, U. Hilleringmann, U. Schürmann, M. Scharnberg, V. Zaporajtchenko, R. Adelung, and F. Faupel, *PTFE-Encapsulation for Pentacene based organic Thin-Film Transistors*, IEEE Proc. of the IEEE Polytronic 2005 conference, IEEE Catalog No. 05TH8855C, 63 (2005)
- [2] C. Pannemann, T. Diekmann, U. Hilleringmann, U. Schürmann, M. Scharnberg, V. Zaporajtchenko, R. Adelung, and F. Faupel, *PTFE-Encapsulation for Pentacene based organic Thin-Film Transistors*, Material Science-Poland 25(1), 95, (2007)

4 Teflon-based Electret Layers for Threshold Voltage Tuning

4.1 Introduction

In the last chapter a Teflon-based functional organic thin film that could serve as one part of a capping layer for OTFTs was examined. An encapsulating layer is required if the organic semiconductor is susceptible to degradation by the ambient air or moisture.

However, deposition of an additional film means that an additional processing step would be required in the fabrication, which results in increased production costs. If the capping layer could be further functionalized to enhance the device performance, the cost-value ratio of the additional deposition step would improve. A capping layer containing a Teflon-based layer as introduced in the last chapter might serve as such a multifunctional organic thin film.

As already mentioned in chp. 2, one major problem of organic semiconductors are high threshold voltages. One additional reason for high threshold voltages are new organic gate dielectrics developed for all-organic-TFTs. They must be deposited as thick pin-hole free films in order to reduce leakage currents through the dielectric [10]. The capacitance of the gate oxide is inversely proportional to the thickness of the dielectric layer. A very thick film leads to a small capacitance of the dielectric. Since the threshold voltage is inversely proportional to the capacitance, small capacitances result in increased threshold voltages.

Furthermore, oxygen plasma treatments can improve the crystallinity of the pentacene films [86, 89], resulting in higher currents but also in a large positive shift of the threshold voltage [86, 90, 91]. For most applications the threshold voltage should be in the range of several volts. Especially for portable electronics typical battery voltages have to be sufficient. However, threshold voltages of OTFTs can reach orders of up to several dozen volts. One approach to tune the threshold voltage of OTFTs is the realization of dual-gate OTFTs (see fig. 4.1) [92], in which the second gate lowers the threshold voltage of

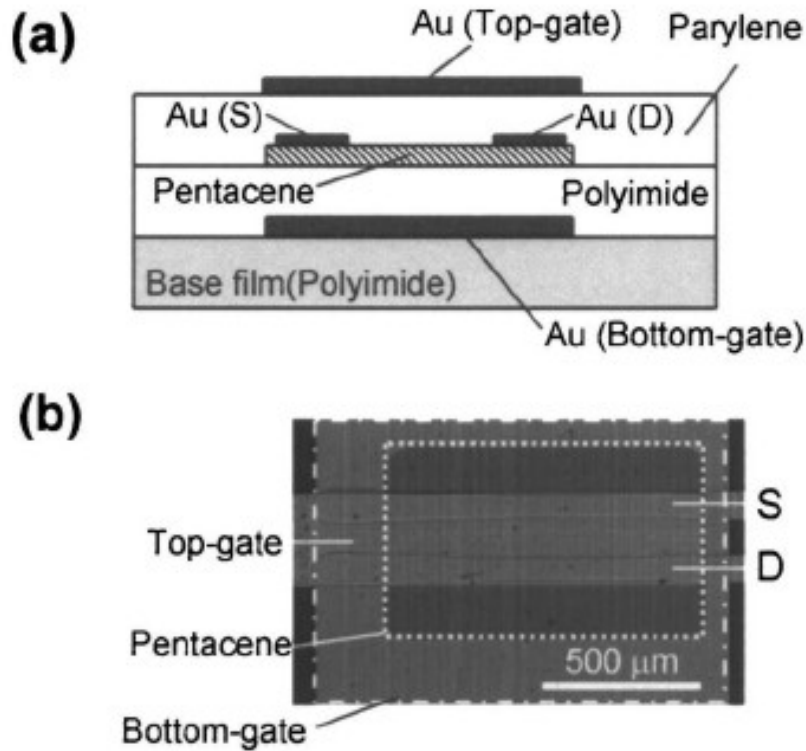


Figure 4.1: (a) The cross-sectional illustration of organic transistors on plastic films with double-gate structures. (b) A micrograph of the fabricated TFTs. The dashed-line represents the area of pentacene, while the dash-dotted line represents the bottom-gate electrode (from [92]).

a bottom-gate field effect transistor. Such setups would ultimately also be limited by the battery voltage, as this is the maximum voltage that can be applied to the top gate.

A second approach for controlling the threshold voltage is the charging of the gate dielectric with a permanent charge. This approach was successfully demonstrated for SiO_2 and spin-on *silsesquioxane* (SSQ) gate dielectrics in BOC-OTFTs [93]. However, this approach has two disadvantages. First, the gate has to be charged prior to deposition of the organic semiconductor. Thus, it is not possible to shift the threshold voltage with knowledge of the actual device characteristics after fabrication. Second, it is impossible to combine this approach with TOC-FETs or the capping layer approach that was discussed in the last chapter. SiO_2 films require deposition temperatures that are incompatible with organic films and also flexible plastic substrates. The spin-on SSQ films can also not be implemented in a multilayer capping layer as the solvents required for spin coating might damage the organic semiconducting thin film.

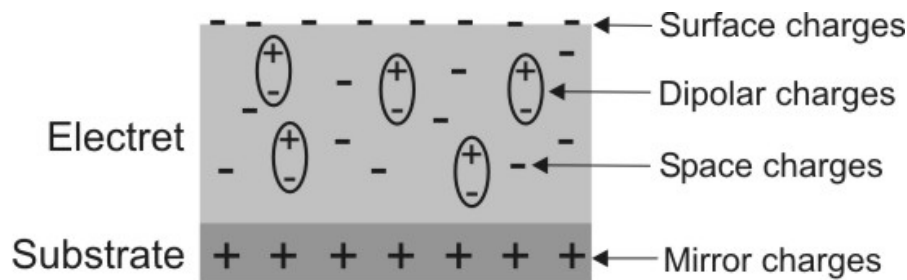


Figure 4.2: Schematic representation of an electret. The total charge is determined by dipolar and mirror charges on the one hand and trapped charges (surface and space) on the other hand. In Teflon surface charges are dominant.

Electrets carry a quasi-permanent electric charge with charge densities that allow reaching voltages of up to several hundred volts. Teflon films have been successfully implemented as electrets for a long time, e.g., in electret microphones [94]. Successful deposition of a Teflon-based film onto a working OTFT was presented in the last chapter. If a Teflon capping layer could also serve as second gate in a dual-gate OTFT, this bifunctional layer would address two problems faced in fabrication of OTFTs. In the following chapter, Teflon AF 1600 is deposited on top of a bottom gate Pc-TFT in order to examine whether the threshold voltage can be tuned by controlled charging of the electret film.

The work presented in this chapter was realized in cooperation with the Department EIM-E/Sensor Technology of the University of Paderborn, which provided the OTFT microstructures and performed the electronic characterization.

4.2 Electrets

4.2.1 Basics

An *electret* is defined as a dielectric material that carries a quasi-permanent electric charge. Quasi-permanent means that the time constant of the charge decay is much higher than the duration of the experiment [94]. In good electret materials the charges are stable for more than several decades. A schematic representation of an electret is shown in fig. 4.2. An electret features a permanent electrical field, if dipolar (displaced) charges and mirror charges in the substrate (in case of a conducting substrate) on one side and trapped (surface and space) charges on the other side do not compensate each other. In Teflon FEP trap charges are dominating [94]. Contributions of dipoles can be

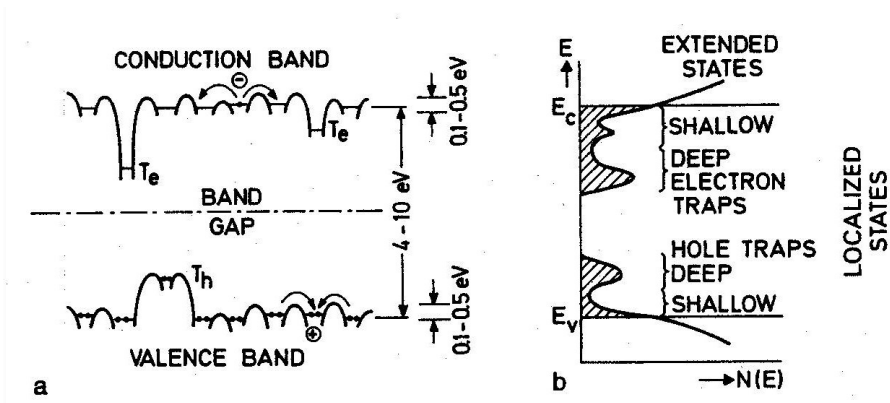


Figure 4.3: Energy band diagram of a polymer. Charge carriers are localized in trap states in the band gap close to the conduction and valence band (from [94]).

neglected as it can be expected from the low dielectric constant which is an indication of the low polarizability of the material. In fig. 4.3 the energy band diagram of a polymer is shown.

Due to the disordered structure of amorphous and semi-crystalline polymers the band edges are not sharp and distinct as known from inorganic semiconductors. The band structure depends on the local molecular environment. Because of varying spacing between molecules the splitting into bonding and anti-bonding states also varies resulting in the locally varying band structure. The *valence band edge* E_v and the *conduction band edge* E_c are better described as *mobility edges*. Near the mobility edge the charge carrier mobility changes abruptly. The space and surface charges are localized in trap levels near the mobility edge. The depth of the trap levels also depends on the local molecular environment. Charges are localized in these traps until they gain enough energy to leave the potential well of the trap level and reach the conduction or valence band. The trapping time depends on the depth of the trap level and the temperature.

In amorphous polymers trap levels are generated by local defects. For space charges these can be impurities, defects in monomers or cross-links. The origin of the surface traps is not well understood. Chemical impurities, surface defects due to oxidation and chain ends are among the suspected mechanisms. Surface traps are of great importance if surface charging techniques like the corona-discharge (see chp. 4.3.2) are used [94].

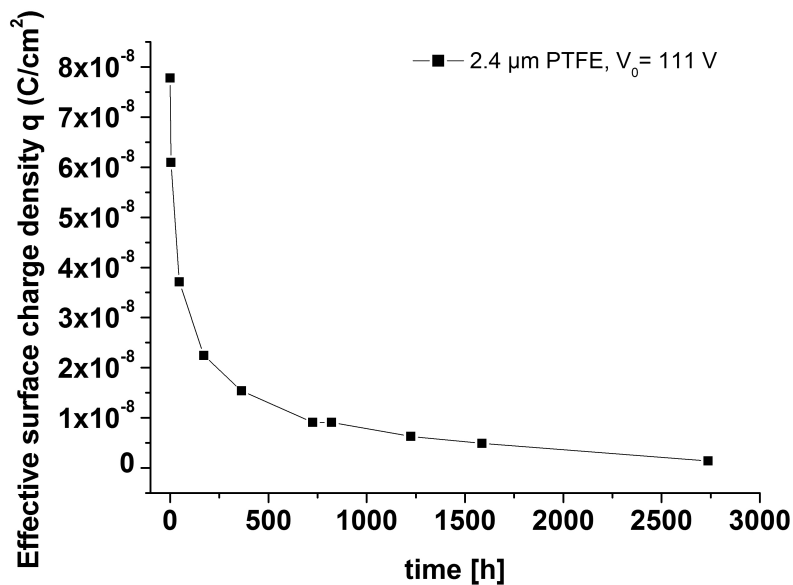


Figure 4.4: Charge decay in a 2.4 μm PTFE electret layer stored at room temperature in ambient air. Within the first 48 hours 50% of the initial charge decayed. Therefore, Teflon AF was chosen as electret material for the experiments.

4.2.2 Selection of the Electret Material

In the last chapter, a PTFE functional organic thin film was used as a capping layer for OTFTs. PTFE is known to be an excellent electret material [95] and PTFE films deposited by *pulsed laser deposition* (PLD) showed excellent charge stability [96]. If sputtered PTFE films are also good electret materials an electret-based dual gate OTFT can easily be realized and combined with the capping layer approach discussed in the previous chapter. The advantage of sputtered PTFE is that it allows fast deposition and uniform coverage of larger areas as compared to thermal evaporation.

However, isothermal storage of a PTFE electret at room temperature revealed a poor performance. Fig. 4.4 shows the change in charge density with time for a 2.4 μm PTFE film that was charged at 600 V and stored in ambient air at room temperature. After 48 hours the charge density already dropped by more than 50%. Therefore, the sputtered PTFE is not suitable as electret material and was not further examined.

Teflon AF (see fig. 4.5) is also known as an excellent gate dielectric [95]. It is typically deposited by spin coating but unlike most polymers it can also be deposited by thermal evaporation [97] (see chp. 4.3.1 for details). The evaporated films are also excellent electrets. [98, 99]. Compared to spin-coating thermal evaporation has the advantage

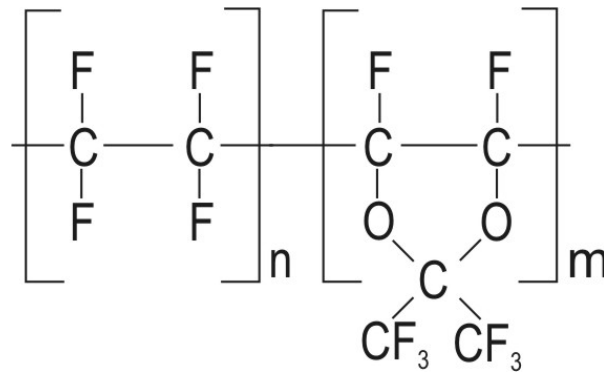


Figure 4.5: Chemical structure of Teflon AF.

that it is a solvent-free process because the solvents for Teflon AF are on the one hand very toxic and solvent residues in the electret film can influence the charge stability [97]. Also, thermal evaporation in an UHV chamber would also be compatible with the multilayer approach discussed in the last chapter.

Teflon AF is an amorphous copolymer composed of the *tetrafluoroethylene* (TFE) monomer and the *2,2-bis(trifluoromethyl)-4,5-difluoro-1,3-dioxole* (PDD) monomer. The ratio of TFE and PDD monomers is 1:2 for AF 1600 which has a T_g of 160 °C [100].

4.3 Methods

4.3.1 Thermal Evaporation of Teflon AF

The thermal evaporation of metals as described in chp. 2.4.2 is based on a simple mechanism. The metal is heated to a temperature at which its vapor pressure exceeds the base pressure in the vacuum chamber and single atoms are evaporated or sublimed. For polymers the process is more complicated. Decomposition and thermal degradation of the monomers due to heating renders thermal evaporation of most polymers impossible without changing their chemical structure. The deposited films are only decomposition products of the original monomers and can be very different in chemical composition.

A special property of Teflon AF is the fact that upon annealing cleaving of the bonds between to dioxole fragments in the backbone between the monomers is preferred and the created free radical is stabilized by interaction with the adjacent oxygen atom [97]. During thermal evaporation single monomers are therefore evaporated and these monomers polymerize on the substrate surface. While the chemical structure of Teflon AF is not changed upon deposition only the molecular weight decreases resulting in a lower T_g .

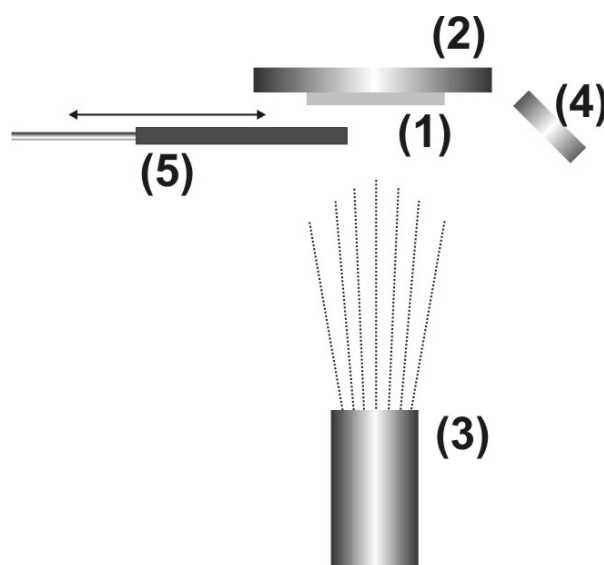


Figure 4.6: Schematic of the UHV chamber for polymer evaporation: The sample (1) is fixed to a sample holder (2). The polymer is evaporated from the evaporator (3) while the deposition rate is determined by a QCM (4). A shutter (5) protects the sample during heating and cooling of the evaporator.

The Teflon AF films were deposited by thermal evaporation in an UHV chamber (see fig. 4.6). The substrate was placed on a sample holder above the evaporator. A shutter could be moved between the substrate and the evaporator while the evaporator was heated up or cooled down in order to avoid unwanted film deposition. The evaporator was developed in the Chair for Multicomponent Materials by Dipl.-Ing. Stefan Rehders and Dr. Vladimir Zaporozhchenko. It features a large Cu crucible allowing uniform

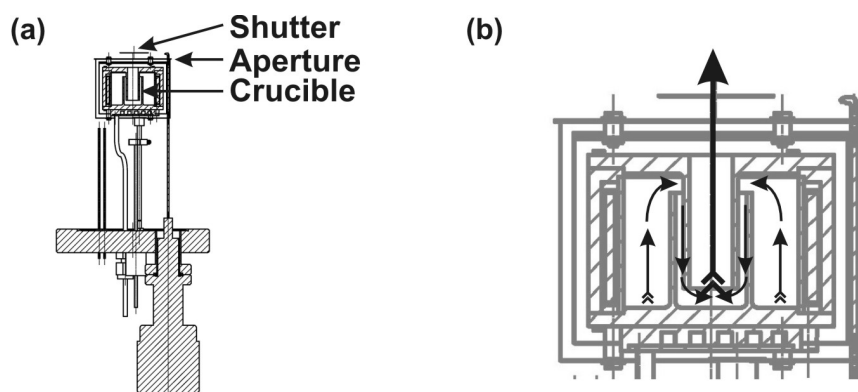


Figure 4.7: (a) Drawing of the polymer evaporator used for deposition of Teflon AF. (b) The crucible was constructed in a way, that the polymer is evaporated indirectly, so that only monomers and small molecules can leave the evaporator.

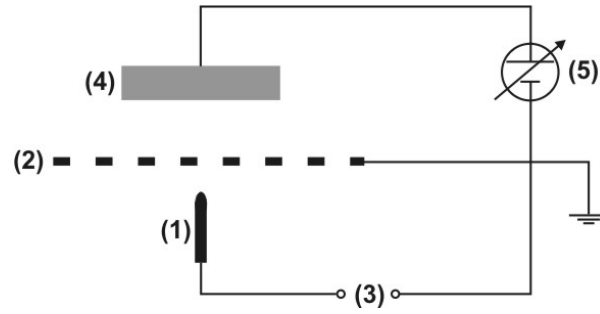


Figure 4.8: Schematic of the corona discharge setup. Between a fine tungsten tip (1) and a steel grid (2) a 5 kV AC voltage is applied by a power supply (3). Between the grid and the sample (4) a DC voltage is applied by a variable power supply (5).

heating of the polymer (see fig. 4.7(a)) The monomers are not evaporated from the reservoir directly towards the sample but have to take an indirect path (see fig. 4.7(b)). This design is chosen to avoid deposition of larger polymer species during heating and melting of the polymer. The deposition rate was measured with a QCM (see chp. 3.3.2) and the final film thickness was determined by profilometer measurements as described in chp. 2.4.5. The base pressure in the chamber was 10^{-7} mbar. Teflon AF was evaporated at $385\text{ }^{\circ}\text{C}$ raising the pressure to 10^{-5} mbar. Teflon FEP was evaporated at $440\text{ }^{\circ}\text{C}$ and the chamber pressure was in the range of 10^{-4} mbar.

4.3.2 Electret Charging

The polymer films were charged using a corona discharge. A schematic of the custom-made device is shown in fig. 4.8. Between a fine tungsten tip and a steel grid a 5 kV AC voltage is applied. Due to the high density of the electric field near the tip, molecules from the ambient air are ionized. The DC voltage that is applied between the grid and the sample allows the extraction of ions from the discharge region. By choosing the polarity of the field either positive or negative ions can be extracted. In air, the negative ions are mainly CO_3^- of thermal energy and the positive charge carriers are $(\text{H}_2\text{O})_n\text{H}^+$ [94]. The sample is charged by ions until the field created by the charges in the sample compensates the extraction voltage.

Due to the low energy of the negative charge carriers it is likely that they transfer their charge to the sample and then reenter the air. For Teflon it was found that the charges penetrate just a little or not at all into the sample [94]. This is important for the desired application in electret-based dual-gate OTFTs as the charge should not penetrate into the TFT, where they might affect the device performance.

4.3.3 Charge Density Measurements

The charge of the electret was measured by a voltage compensation method. The electret was placed parallel to a metalized membrane with an air gap in between. An acoustic source oscillating at a frequency of 1 kHz causes a vibration in the membrane. The resulting AC voltage was compensated with a DC voltage. This compensation voltage is proportional to the *effective surface charge density* q , which is given by

$$q = -\frac{\epsilon_0 \epsilon_r V_0}{d} \quad (4.1)$$

where ϵ_0 and ϵ_r are the dielectric constant of vacuum and the relative dielectric constant of the dielectric respectively, V_0 the compensation voltage and d the thickness of the dielectric [94].

Since d is known and V_0 is determined by the compensation measurements, the charge density q can be calculated using equation 4.1.

4.3.4 Electronic Characterization

In order to determine the shift in the threshold voltage due to charging of the electret the square root of the drain-source current in dependence of the *gate-source voltage* V_{GS} was measured at a fixed drain-source current I_{DS} of -5 V. The influence of the electret gate on the field effect mobility and on-current of the TFT was determined by measuring I_{DS} in dependence of the drain-source voltage V_{DS} for V_{GS} ranging from +5 to -40 V directly before and after deposition of the electret gate. All measurements were performed in a shielded metal box without illumination using a HP 4145A Semiconductor Parameter Analyzer from Hewlett-Packard.

4.4 Tuning of the Threshold Voltage

In order to test the approach, Teflon AF 1600 films were deposited onto working BOC-Pc-TFTs and the change in the threshold voltage was measured.

4.4.1 Sample Preparation

4.4.1.1 Pc-TFTs

The Pc-OTFTs were very similar to the TFTs described in chp. 3.4.2.1. Heavily doped p-type silicon wafers served as both substrate and common gate for all fabricated transistors. The SiO₂ gate dielectric was grown by a wet thermal oxidation step at 960°C and had a thickness of 138 nm. The drain and source bottom contacts (see fig. 3.5) were patterned using UV photolithography and lift-off by ultrasonic agitation. An interdigital contact design with a W/L ratio of 37,500 was chosen to ensure large drain-source currents even after the deposition of the Teflon layer which is assumed to affect the upper layers of the organic film. The contacts were formed by DC-sputtering of Au after a 4 nm thin Ni layer was deposited as adhesion promoter. After the surface of the dielectric was cleaned with oxygen plasma (30 s, 100 W) to improve the organic film formation, a 30 nm thick film of pre-purified pentacene was deposited by thermal evaporation at a base pressure of $1 \cdot 10^{-6}$ mbar and a low deposition rate while the substrate was kept at room-temperature. As a result of the plasma treatment, large Pc grain sizes of up to 1 μm were obtained [85].

4.4.1.2 Electret Gate

A 2 μm thick Teflon AF 1600 film was deposited onto the Pc-TFT by thermal evaporation and was charged to a charge density of $-1.3 \cdot 10^8$ C/cm² using the corona discharge method. This corresponds to a compensation voltage of -15 V.

4.4.2 Electronic Characterization

After fabrication of the BOC-Pc-TFTs the output and transfer characteristics were measured to determine their initial performance. The output current at V_{DS} of -40 V and V_{GS} of -40 V was as large as -800 μA (see fig. 4.9(a)) and the calculated charge carrier field-effect mobility was $4.6 \cdot 10^{-4}$ cm²/Vs.

The threshold voltage was extracted from the square-root of the on-current characteristics (see fig. 4.10(a)) and was found to be +13.1 V due to a modification of the surface potential of the dielectric induced by the oxygen plasma [90].

After charging of the electret, the OTFTs were characterized again showing a reduced on-current of -42 μA and a decreased charge carrier field effect mobility of $6 \cdot 10^{-5}$ cm²/Vs (see fig. 4.9(b)). This reduction might be caused by the deposition of the additional layer

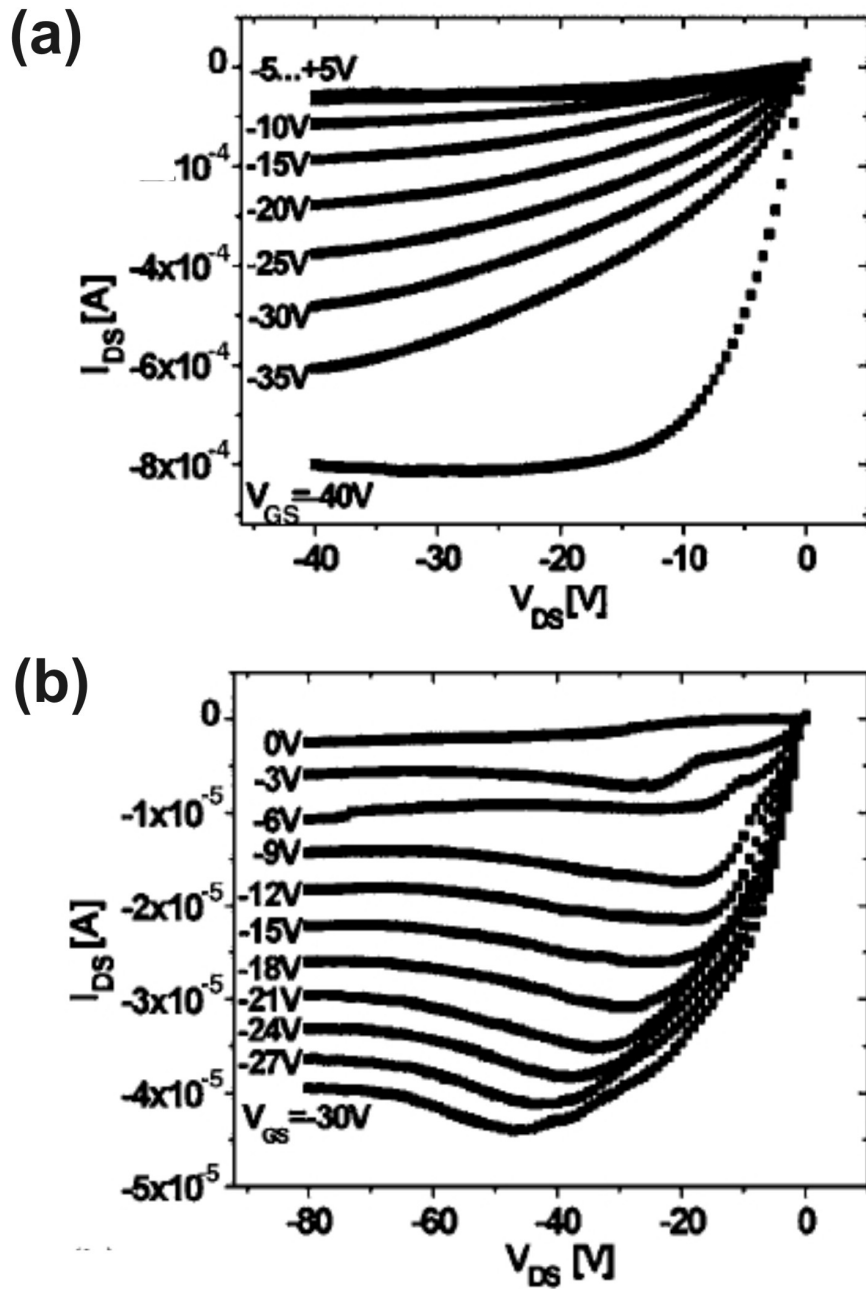


Figure 4.9: Drain-source current versus drain-source voltage of the Pc-TFT (a) prior to deposition of the Teflon AF 1600 thin film and (b) after deposition and charging of the electret layer. The field effect mobility decreased from (a) $4.6 \cdot 10^{-4} \text{ cm}^2/\text{Vs}$ to (b) $6 \cdot 10^{-5} \text{ cm}^2/\text{Vs}$. The qualitative change in the shape of the curves, e.g., the minimum, is attributed to degradation by exposure to oxygen.

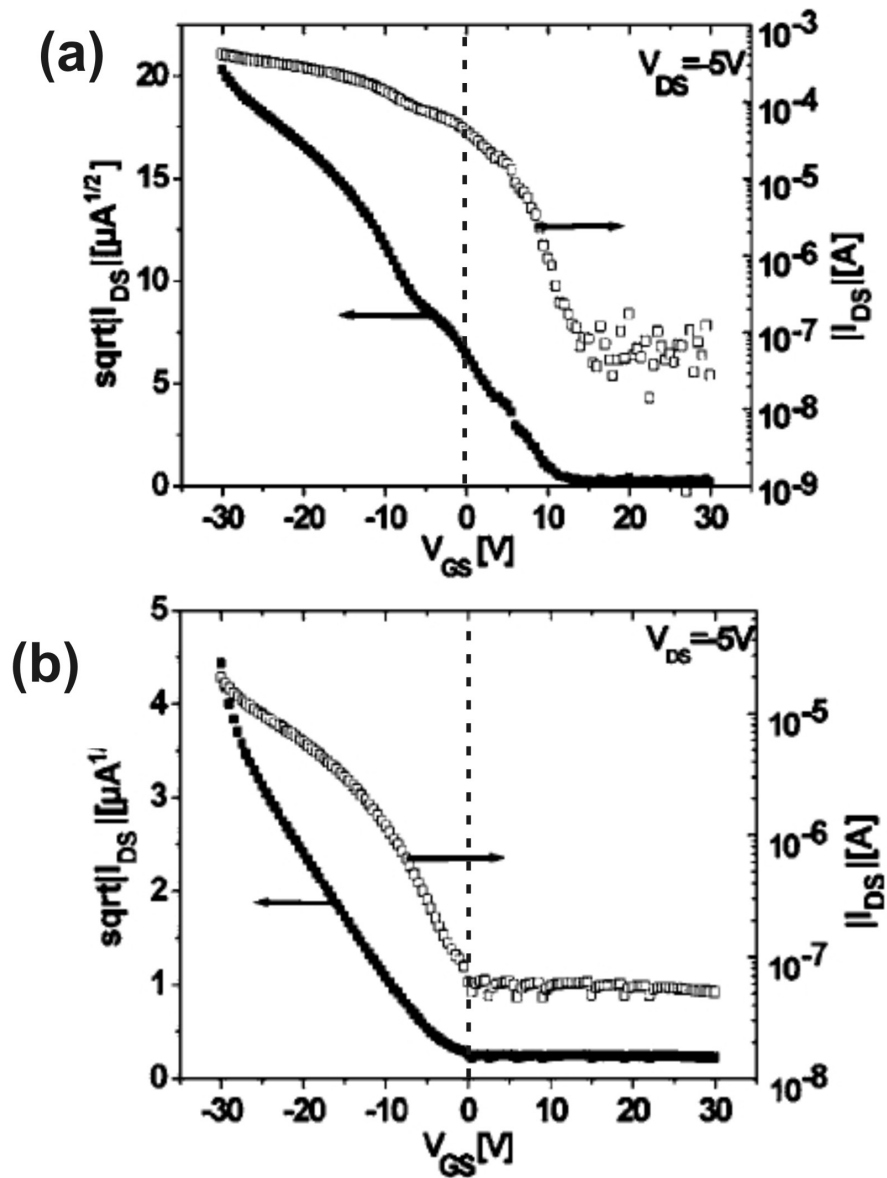


Figure 4.10: Drain-source current versus gate-source voltage of the Pc-TFT (a) prior to deposition of the Teflon AF 1600 thin film and (b) after deposition and charging of the electret layer. The threshold voltage shifted from (a) +13.1 V to (b) -2.3 V.

onto the organic semiconductor as was already reported before [101] or due to aging of the film in between charging of the film and the I-V measurements. The threshold voltage can be extracted from the transfer characteristics in fig. 4.10(b) and was determined to be -2.3 V as compared to +13.1 V prior to electret deposition. The shift in the threshold voltage agrees very well with the charging of the electret to -15 V indicating that the shift is caused by the depletion of the channel region due to the positive charge carriers being pulled towards the electret top gate. The excess holes might then be trapped in the top of the pyramidal structure of the pentacene crystallites which are only connected at the base (see fig. 2.18). The shift of the threshold voltage towards more negative values cannot be attributed to aging since a negative shift could only be caused by degradation due to moisture. This is prevented by Teflon films as was shown in the last chapter.

In addition to the shift in the threshold voltage a qualitative change in the shape of the I-V curves is observed, e.g., a minimum in the $I_{DS} - V_{GS}$ curve. These changes are attributed to aging of the organic semiconductor due to exposure to oxygen as it was shown in the last chapter that Teflon-based capping layers cannot block oxygen. The shift in the threshold voltage cannot result from this aging as it would lead to a shift of the threshold voltage towards more positive values.

4.5 Summary and Outlook

In this chapter, the feasibility of a Teflon-based electret layer for control of the threshold voltage was investigated. A Teflon AF 1600 film was charged with negative charge carriers, creating an electret film. It was shown that the threshold voltage of a BOC-OTFT was shifted after charging of the electret proving the general feasibility of the approach. In order to determine if the decreased current and mobility are caused by the electret or by aging of the organic semiconductor should be determined in future experiments, maybe even in combination with the multilayer diffusion barrier approach.

Using an electret layer as top gate has several advantages. No active power supply is required, as the charge carriers are trapped in the electret quasi-permanently. Therefore, leakage currents through the top gate electrode are also no issue. The major advantage of this approach is the wide range of voltages that can be realized. Voltages are not limited to values of typical batteries but voltages in the range of 10^0 to 10^3 can be easily achieved.

Additionally, the Teflon film can be charged locally using a corona setup, which allows a selective charging of different parts of a wafer with different voltages. Furthermore,

sputter deposition as well as thermal evaporation are suitable for deposition of Teflon films onto the organic semiconductors, since they do not damage the active layer. Other approaches that use spin-coating or thermally grown SiO₂ could not be used for top-gates as neither solvents nor high temperatures are not compatible with Pc thin films. Gate dielectrics of BOC-TFTs that are charged as electrets can also be used to control the threshold voltage but cannot act as a protective layer against degradation of the active layer, as the organic semiconductor is deposited on top of the electret gate.

Just as the PTFE layer in the last chapter, Teflon AF 1600 thin films cannot prevent aging of the organic semiconductor. However, the electret gate and the multilayer barrier approach described in the last chapter might be combined. A capping layer consisting of alternating films of ceramic oxide and a Teflon AF in which the last Teflon layer is charged as electret would not only protect the film from aging but would also allow control of the threshold voltage. Thermal evaporation is not feasible for technical applications if film thicknesses above 1 μm are required, but the thicknesses required for multilayer barriers and low-voltage electrets ($V < 30$ V) are only in the range of 100 nm to 1 μm.

It is also of interest to investigate, if the sputtering process of PTFE can be optimized in order to improve the electret properties of these films as it was already shown that PTFE films deposited by pulsed-laser deposition show good electret properties [96]. Sputtering allows higher deposition rates than evaporation and is therefore better suited for industrial applications.

In addition to the control of the threshold voltage demonstrated above, new sensor applications might be possible. An electret could be used to either turn a field effect on or off until the charges in the electret decay. Without external influence the charges are quasi-permanently stable, but, e.g., vapors of solvents like acetone, can lead to charge decay in the electrets, switching the transistor from on(off) to off(on). The switching of the transistor could be used as sensing signal.

The dual-gate-electret approach can now be applied to other OTFT structures. TFTs using carbon nanotubes as semiconductor are known to have very promising properties, e.g., high on/off ratios, but also show high threshold voltages. Using an electret to tune the threshold voltage might allow the use of the good characteristics of the tube-FETs while avoiding the drawback of the high threshold voltages.

4.6 Author's Related Publications

- [1] M. Scharnberg, V. Zaporojtchenko, R. Adelung, F. Faupel, C. Pannemann, T. Diekmann, and U. Hilleringmann, *Tuning the threshold voltage of organic field-effect transistors by an electret encapsulating layer*, Appl. Phys. Lett. 90, 013501 (2007)
- [2] M. Scharnberg, V. Zaporojtchenko, F. Faupel, manuscript in preparation

5 Water Jet Reflection on Ultrahydrophobic Surfaces

5.1 Introduction

In the previous chapters two applications of functional organic thin films - as capping and electret layer - were described. The capping layers use the hydrophobic nature of the Teflon films to block permeation of water molecules. In this chapter, another application for the hydrophobicity of functional organic thin films is presented. By deposition of a hydrophobic Teflon-based thin film a microstructured hydrophilic metal surface is turned into a ultrahydrophobic surface.

Ultrahydrophobic materials are of great technological and commercial interest as they might find applications in wall and car paints, roof tiles and many other applications. The ultrahydrophobicity is caused by a combination of a hydrophobic surface chemistry and a surface structure with a roughness in the micro- or nanometer range [102].

In the scope of the work on ultrahydrophobic surfaces a new phenomenon was observed which has not been reported for water yet - the reflection of water jets. Scattering and reflection phenomena are known and well studied for a lot of physical systems, i.e. light or neutron scattering or the reflection of sound waves. What distinguishes the water jet reflection from all other reflection and scattering phenomena is that the jet is not reflected at the point of incidence. It impinges on the surface, flows across the ultrahydrophobic surface for a distance that is equivalent to several jet diameters before it takes off from the surface as a coherent jet.

In the following chapter the water jet reflection from ultrahydrophobic surfaces is described and the influence of the angle of incidence, the water pressure and the surface structure on the take-off angle are examined. Because biological surfaces show irregularities like leaf veins and other defects a systematic study of the water jet phenomenon is not possible as these defects interfere with the reflection. Therefore, an artificial ultrahydrophobic surface was created by deposition of a Teflon-based organic thin film

onto a microstructured metal alloy surface. These artificial surfaces feature a regular microstructure that can be varied precisely and is defect-free. These surfaces allowed a qualitative analysis of the water jet reflection.

5.2 Reflection of Liquids

A comparable phenomenon was first observed in 1928 for a jet of mercury impinging on a steel ball [103]. A jet of liquid mercury impinging on a steel ball was observed to form a non-spherical sheet on the ball surface before gathering itself and taking off from the surface as coherent jet.

Mercury has a very high surface energy/tension. Therefore, it will not wet most surfaces. When the mercury jet impinges on the surface, it spreads across the surface increasing its total energy. Contraction of the mercury would lower the overall energy and transforms the mercury back into a jet. The momentum of the mercury atoms perpendicular to the plane of the substrate surface might be converted into potential energy by spreading of the mercury across the sample surface and then reconverted upon contraction causing the jet to take off from the surface. The effect has not been examined or described in detail and no photographs or videos exist.

If this phenomenon is based on the lack of wetting, the high surface tension of the liquid and the momentum conversion, it should also be observed for other liquid/substrate systems. Water would be a promising candidate for a liquid, as it is readily available and less hazardous than mercury. However, water wets most surfaces limiting the number of materials that come into question. Even for hydrophobic surfaces like Teflon films with water contact angles of about 120° the wetting is still too strong so that the phenomenon is not observed. Ultrahydrophobic surfaces like the leaves of the Lotus plant are not wet by water as the contact angle of water droplets is larger than 160° . Water jets impinging on such surfaces should be reflected.

In fact, the reflection of water drops from ultrahydrophobic surfaces (*bouncing droplets*) is well known and studied [104–106]. Here the angle of incidence is perpendicular to the plane of the surface and the drop is reflected along its original path. And in chp. 5.5 it is indeed shown that water jets are reflected off the surface of biological ultrahydrophobic surfaces. However, these natural surfaces show a lot of irregularities like leaf veins that impede the flow of the jet across the surface. In order to examine the physics behind this phenomenon and to determine the influence of water pressure, angle of incidence and microstructure of the surface it is necessary to use ultrahydrophobic surfaces that are

homogeneous and defect-free. A microstructured NiAl-1.5 at.% Re alloy coated with a PTFE thin film is such a ultrahydrophobic system and was used for the work presented here.

5.3 Biological and Artificial Ultrahydrophobic Surfaces

The water jet reflection was observed for both natural and artificial ultrahydrophobic surfaces. Since their microstructure is different, this already indicates that the surface morphology does not play a significant role, as long as the surface is ultrahydrophobic.

5.3.1 Nasturtium

Nasturtium (*Tropaeolum majus*) belongs to the group of plants with leaves that are ultrahydrophobic. The surface of a leaf is shown in a *scanning electron microscopy* (SEM) image in fig. 5.1. The leaf surface shows a roughness in the micrometer range (see fig. 5.1(a)) and is covered by wax crystals which provide a hydrophobic surface chemistry (see fig. 5.1(b)). While a water jet is reflected, irregularities like leaf veins can disturb the reflection making it difficult to study the phenomenon qualitatively on these surfaces. Leaves from two different types of Nasturtium plants were used for this work.

5.3.2 Teflon-coated Metal Fibers

In order to systematically study this phenomenon it is necessary to use ultrahydrophobic surfaces that are defect-free. In addition it would be beneficial if the microstructure of the ultrahydrophobic surface could be varied in order to study its influence on the water jet reflection.

A suitable model system is a eutectic NiAl-1.5 at.% Re alloy. By directional solidification in a Bridgman-type growth facility a single crystal is grown. Due to the strongly asymmetric composition of the eutectic alloy and the simultaneous solidification of both phases the minor phase (hexagonal Re) forms nanofibers in the major phase (B2-NiAl) [108]. These nanofibers are all oriented in the same crystallographic orientation [109]. By selective dissolution using an etching solution (HCl(32%) : H₂O₂(30%) : H₂O, 10 : 10 : 80) the major phase is removed. The Re-nanofibers are not etched creating a

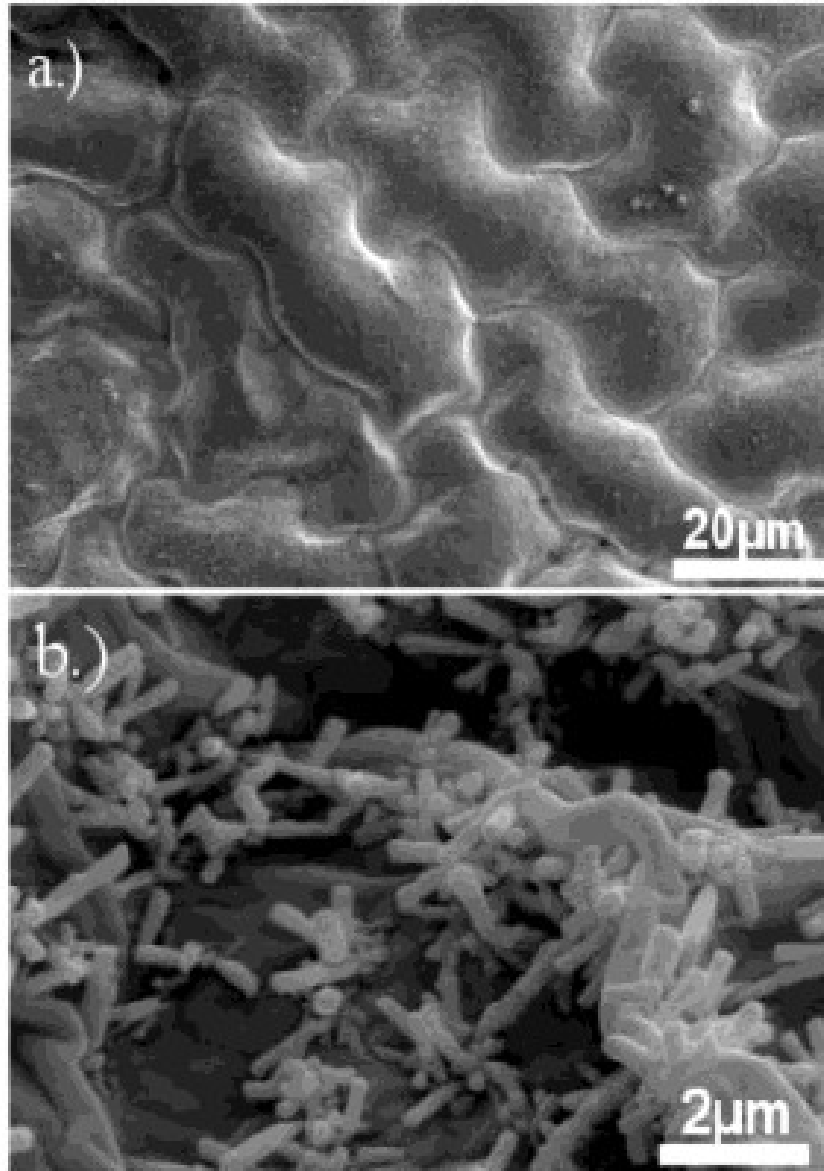


Figure 5.1: SEM image of the surface of a *Nasturtium* leaf (from [107]).
(a) Surface structure of the leaves with a roughness in the micrometer range.
(b) Wax crystals covering the surface shown in (a). The combination of the surface structure and the hydrophobicity of the wax causes the ultrahydrophobicity of the leaf.

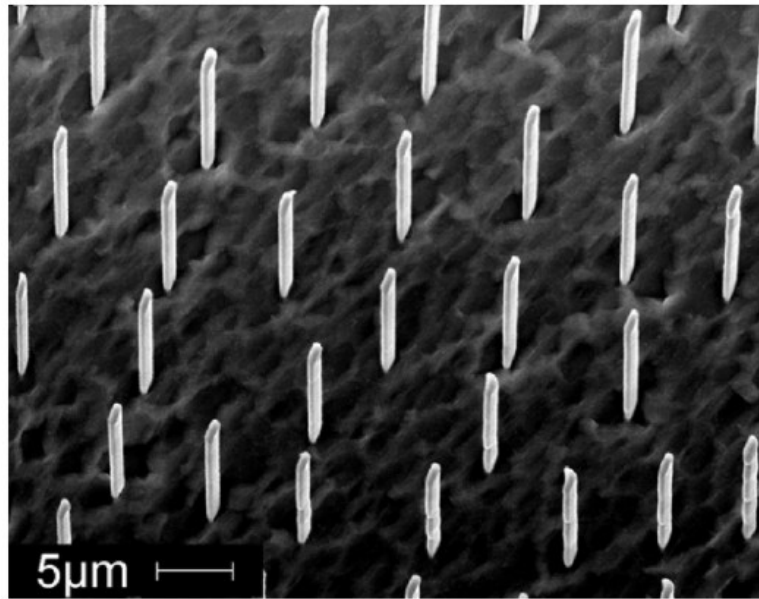


Figure 5.2: SEM image of the etched NiAl-1.5 at.% Re surface (from [110]). The Re-nanofibers can be seen standing upright on the surface and are all oriented in the same direction.

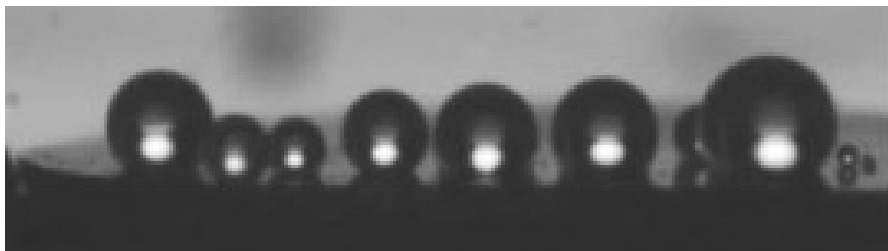


Figure 5.3: Water drops on a artificial ultrahydrophobic surface with a fiber length of 2 to 5 μm .

sample with nanofibers standing upright on the alloy surface (see fig. 5.2). By variation of the etching time, the fiber length can be controlled. In order to obtain an artificial ultrahydrophobic surface the sample surface needs further functionalization. A PTFE thin film was sputtered onto the etched sample covering the nanofibers. A PVD process was chosen as it allows deposition of functional organic thin films while maintaining the surface topography of the substrate. Other techniques like spin coating would not allow covering of the nanofibers with a thin film. This is of great importance as the resulting combination of rough microstructure of the alloy and the hydrophobicity of the PTFE film creates a ultrahydrophobic surface with contact angles above 160° (see fig. 5.3). On these regular and defect-free surfaces water jet reflection is also observed.

5.4 Methods

5.4.1 PTFE Deposition

The sputter deposition of PTFE thin films was performed in the chamber described in chp. 3.4.2.2. A PTFE film with a nominal thickness of 170 nm was deposited at a power of 50 W and a rate of 12 nm/min. Due to the rotation of the sample holder the needles are covered by Teflon from all sides while the topography of the sample is maintained.

5.4.2 Water Jet

The water jet was formed by manually forcing water from a syringe through an attached needle with an inner diameter of 400 μm . The velocity of the water jet was in the range of 2.4 m/s. The Reynolds number is measure for the type of flow regime. It is given by

$$Re = \frac{vd\rho}{\eta} \quad (5.1)$$

where v is the velocity of the water jet, d the jet diameter, ρ the density of water and η the dynamic viscosity of water. Inserting values of 2.4 m/s for the velocity, 0.4 mm for the jet diameter and 998 kgm^3 and $8.9 \cdot 10^{-4}$ Pa·s for the density and viscosity of water at 25 °C into equation 5.1 gives a Reynolds number of 1076.5. This value is far below the Reynolds number of the turbulent regime for plate flow ($Re > 10^6$). So the water jet reflection on ultrahydrophobic surfaces occurs in the laminar flow regime.

The videos of the water jet reflection were taken with a CCD camera that was connected to a frame grabber card. The videos have a resolution of 640x480 pixels at a frame rate of 25 frames/sec. Captures were taken from the video in order to determine the dependence of the take-off angle on the angle of incidence and the water pressure.

5.5 Water Jet Reflection

In fig. 5.4 a water jet impinging on a nasturtium leaf is shown. Upon impact the jet flattens into a thin sheet that has a non-spherical shape bounded by a thicker roll on each side (fig. 5.5). Since there is no wetting of the ultrahydrophobic surface by the water, the water contracts again in order to minimize its total surface energy. After a flow length in the order of several jet diameters the water converts back into a jet that takes off from the surface under an angle that is close to (fig. 5.4(b,c)) or smaller than

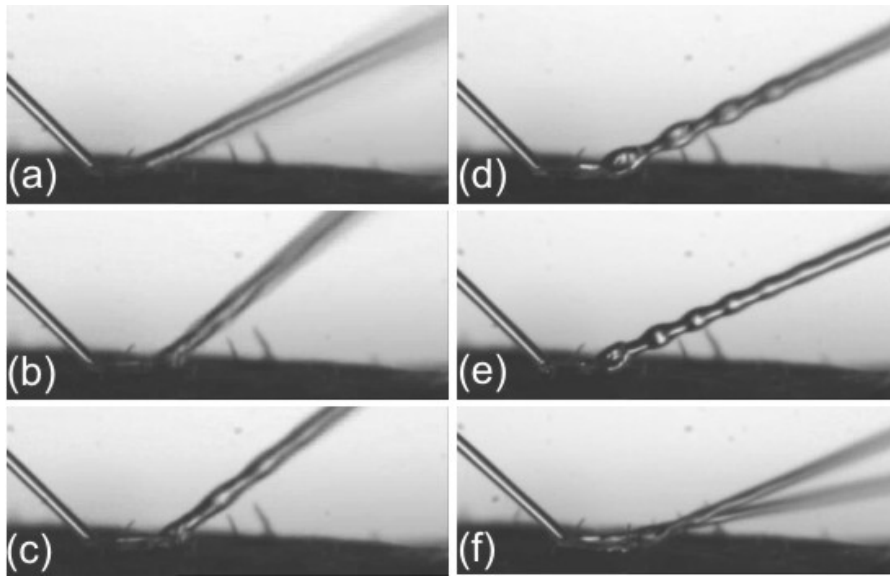


Figure 5.4: Reflection of a water jet on a *Nasturtium* leaf. Oscillations in the reflected jet ((c)-(e)) as well as splitting of the jet at a leaf vein can be observed (f).

the angle of incidence (fig. 5.4(a,d,e)). With increasing pressure the flow length across the surface as well as the width of the elliptical sheet increase (see fig. 5.4 and fig. 5.5, respectively).

With increasing pressure, oscillations are observed in the outgoing water jet (fig. 5.4(c-e)). The oscillations are caused by the forces acting on the water sheet due to spreading across the ultrahydrophobic surface. The water sheet on the surface has a non-spherical cross-section perpendicular to the flow direction. Minimization of the surface energy should result in a circular cross-section of the jet upon take-off. If the restoring forces acting on the water sheet are at higher pressures large enough they cause an overshooting of the jet past the circular cross-section. The cross. section of the jet will take up a non-circular shape again, now with the long axis perpendicular to the initial orientation (see fig. 5.6(a)). The shape of the cross-section will oscillate between the two different non-circular shapes until the energy stored in the oscillation is used up due to friction between water molecules within the jet. The fact that the oscillation is damped and disappears proves that it is not caused by capillary instability. Otherwise the oscillations would increase until the jet decompose into a series of single drops.

This oscillation is a quite common phenomenon which is observed when liquids are poured from a curved spout like milk from a milk carton (see fig. 5.6(b)) and was already described for water ejected from elliptical nozzles [111, 112]. For the bouncing water

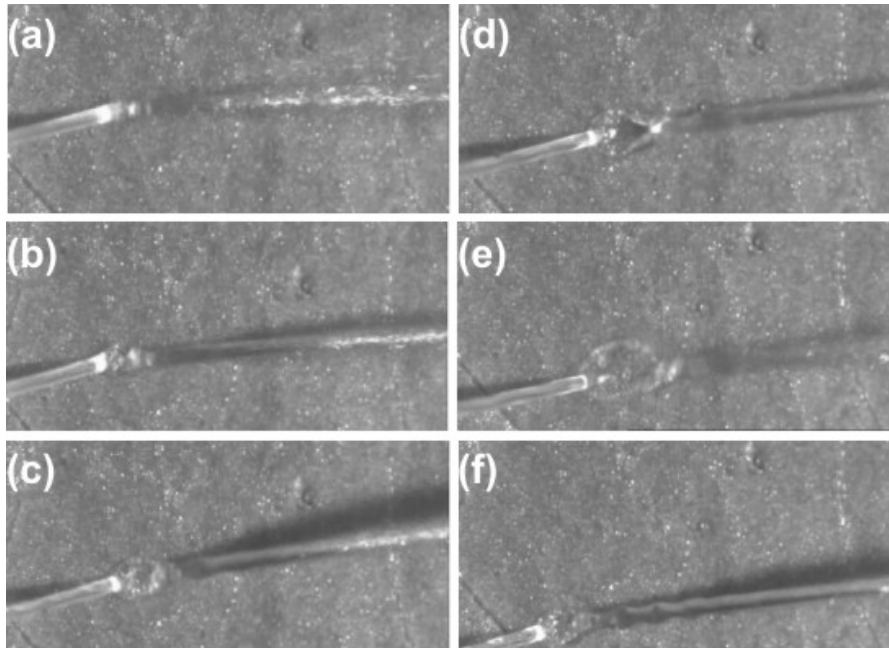


Figure 5.5: Top view of the reflection of a water jet on a Nasturtium leaf. With increasing flow length (i.e. pressure) the area of the elliptical sheet on the leaf surface increases. Oscillations in the reflected jet are observed as well (f).

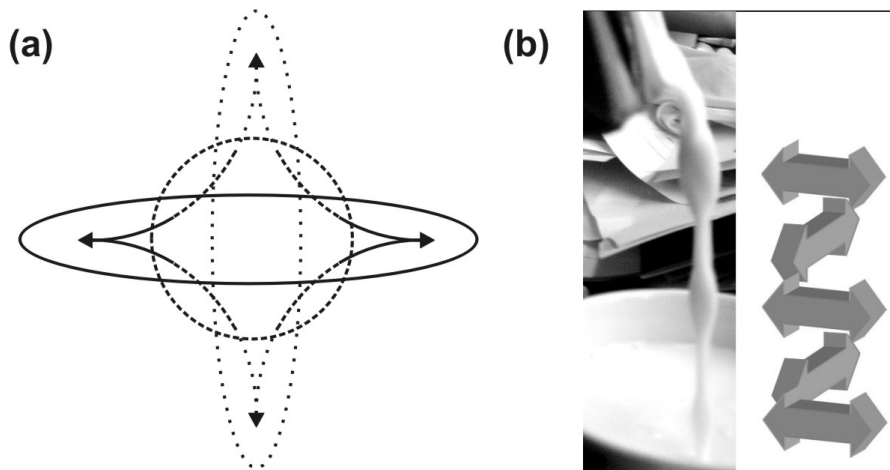


Figure 5.6: (a) Schematic of the cross-section of the water jet. The water jet on the surface has the form of a flat sheet (solid line). Minimization of the surface energy leads to formation of a circular cross-section (dashed line). Overshooting leads to a elliptical cross-section perpendicular to the initial orientation of the long axis (dotted line). The shape of the cross-section oscillates between these two shapes. (b) Oscillation in a milk jet poured from a curved spout.

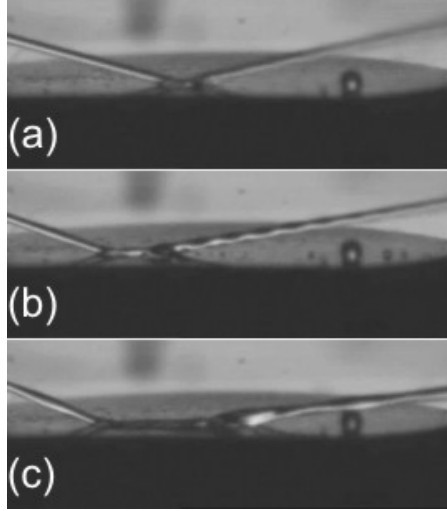


Figure 5.7: Reflection of a water jet on an artificial surface with a fiber length of 2 to 5 μ m. The oscillations observed in the reflected beam are less pronounced as compared to the reflection on the Nasturtium leaf (b). Very long flow length can be obtained on the defect-free artificial surfaces (c).

drops mentioned in chp. 5.2, it was observed that above a certain velocity, the drop loses 10 % of its original velocity to oscillations of its shape [113]. This agrees very well with the increase in the outgoing jet's diameter, which is about 10 % as compared to the diameter of the incoming jet.

Fig. 5.4(f) illustrates the problem discussed in the introduction. If the water jet flows across a defect like a leaf vein, artifacts like a split jet are observed. This limits the maximum flow length of the jet on the surface to about 2.4 mm. In order to study a wider range of flow lengths a defect-free surface has to be used.

Fig. 5.7 and 5.8 show water jets impinging on metal alloy/PTFE surfaces with fiber lengths of 2-5 μ m and 50 μ m, respectively. The basic features of the phenomenon observed are the same as for the nasturtium leaf. The oscillations in the outgoing jet are also observed, however they are not as pronounced as for the nasturtium leaves. Due to the regular structure of the surface, very large flow lengths can be reached. Directly after impact on the surface and a small flow length the take-off angle is almost similar to the angle of incidence (fig. 5.7(a) and 5.8(a)). The flow length is very small at first but increases afterwards. This might indicate that after impact of the jet a steady state needs to be established.

For large flow lengths which are corresponding to high water pressures the diameter of the outgoing jet increases (fig. 5.7(c) and fig. 5.8(f)). Due to the continuum equation the product of jet velocity v_{jet} and area of the jet A_{jet} has to be constant, as no water is

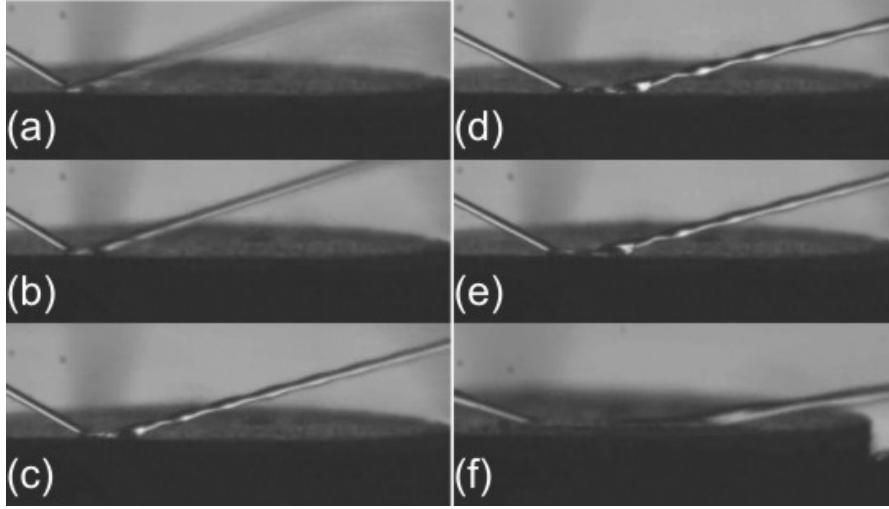


Figure 5.8: Reflection of a water jet on an artificial surface with a fiber length of $50 \mu\text{m}$. The oscillations observed in the reflected beam are less pronounced as compared to the reflection on the Nasturtium leaf (c)-(e). Very long flow length can be obtained on the defect-free artificial surfaces (f).

lost and water is incompressible. Therefore, the increased jet diameter indicates a loss of momentum of the jet for large flow length ratios ($l_{\text{flow}}/d_{\text{jet}} > 10$). But for smaller flow lengths l_{flow} the jet diameter is almost equal to the diameter of the incoming jet. A small increase can be attributed to the oscillation in the reflected jet. As the diameter is almost similar, the velocity of the jet must also be close to the velocity of the incoming jet and the ratio of v_x/v_z does not change with increasing velocity.

The fiber length of the surface does not seem to have a major effect on the reflection of the water jet as fig. 5.7 and fig. 5.8 indicate.

In the graph in fig. 5.9 the ratio of the angle of incidence θ_{in} and the take-off angle θ_{out} with respect to the ratio of flow length l_{flow} and the jet diameter d_{jet} is displayed for two kinds of Nasturtium leaves. For flow length ratios $l_{\text{flow}}/d_{\text{jet}} < 4$, $\theta_{\text{out}}/\theta_{\text{in}}$ is independent of the flow length and thus the water pressure. For larger values of $l_{\text{flow}}/d_{\text{jet}}$, $\theta_{\text{out}}/\theta_{\text{in}}$ seems to decrease. However, large flow lengths could not be examined due to the nature of the nasturtium surface mentioned above. The different values of $\theta_{\text{out}}/\theta_{\text{in}}$ for the two types of Nasturtium leaves most likely originate from differences in the microstructure of the leaves which should be examined in the future.

The same independence of $\theta_{\text{out}}/\theta_{\text{in}}$ on $l_{\text{flow}}/d_{\text{jet}}$ was basically observed for the artificial ultrahydrophobic surface for both nanofiber lengths as shown in fig. 5.10 and 5.11. The fact that θ_{out} does not depend on $l_{\text{flow}}/d_{\text{jet}}$ indicates that the water flows across

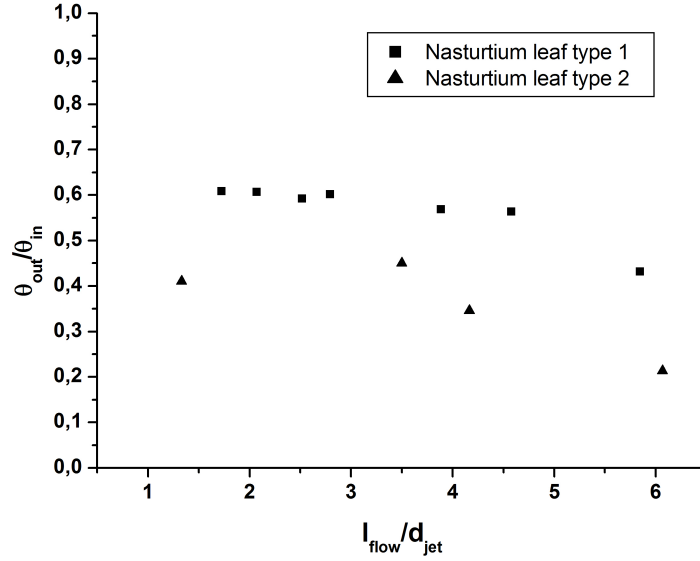


Figure 5.9: Dependence of the ratio of outgoing angle to angle of incidence ($\theta_{\text{out}}/\theta_{\text{in}}$) on the flow length l_{flow} (in jet diameters) for two types of Nasturtium leaves. For $l_{\text{flow}}/d_{\text{jet}} < 4$ the ratios is independent of the flow length. For larger flow length is appears to decrease.

the ultrahydrophobic surface without friction. If friction led to energy loss the take-off angle should decrease. However, this effect is not observed. Slip flow of water across ultrahydrophobic surfaces was very recently proposed in PRL [114] and is still subject to an ongoing discussion [115, 116].

For the 50 μm sample a flow length range exists for which a pressure/flow length dependence is observed. For about $1 < l_{\text{flow}} < 3$ the ratio $\theta_{\text{out}}/\theta_{\text{in}}$ decreases with increasing flow length (see 5.11). For 2-5 μm fiber length there is not enough data for analysis.

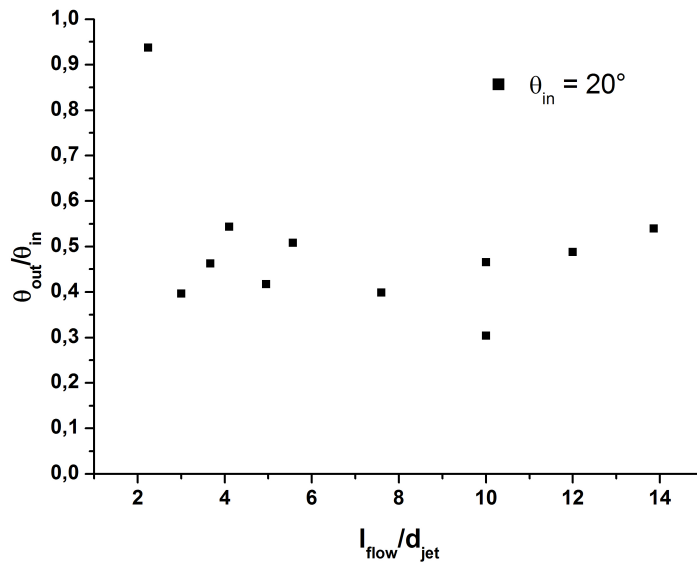


Figure 5.10: Dependence of the ratio of outgoing angle to angle of incidence (θ_{out}/θ_{in}) on the flow length l_{flow} (in jet diameters) for an artificial surface with a fiber length of 2 to 5 μm . The ratio is independent of the flow length for the entire range of l_{flow}/d_{jet} that was examined.

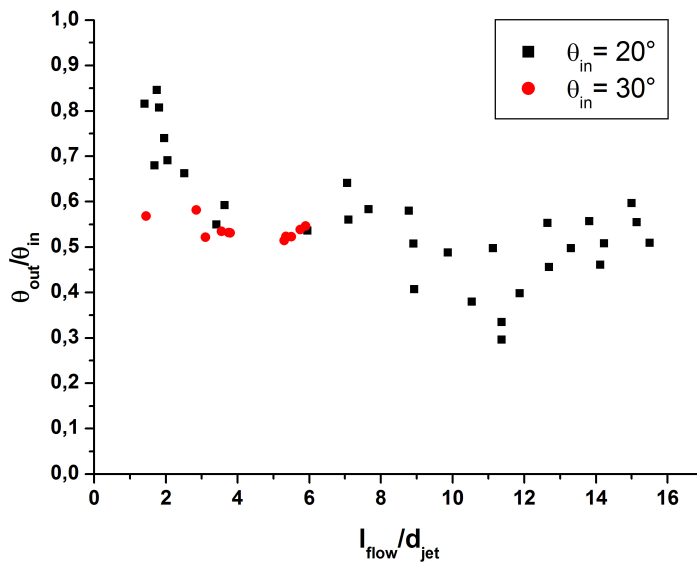


Figure 5.11: Dependence of the ratio of outgoing angle to angle of incidence (θ_{out}/θ_{in}) on the flow length l_{flow} (in jet diameters) for an artificial surface with a fiber length of 2 to 5 μm . The ratio is independent of the flow length for about $3 < l_{flow}/d_{jet} < 15$. For $l_{flow}/d_{jet} < 3$ the ratio strongly decreases from 0.85 to ≈ 0.55 .



Figure 5.12: Multiple reflection of a water jet between two Nasturtium leaves.

5.6 Summary and Outlook

The deposition of a functional Teflon thin film altered the hydrophilic nature of the microstructured metal alloy and created an ultrahydrophobic surface. On these surfaces as well as on leaves of the Nasturtium plant the reflection of water jets was observed for the first time. A jet impinges on the surface, spreads out and flows across it for a distance equal to several jet diameters before it contracts again and takes off as a coherent jet. If two ultrahydrophobic surfaces are placed opposite to each other, even multireflection can be observed (see fig. 5.12).

This phenomenon is based on the absence of any interaction of the ultrahydrophobic surface (except for momentum transfer) and the water jet and on the surface tension of the water. The precise control of the microstructure of the artificial ultrahydrophobic surface allowed the examination of the influence of the microstructure on the water jet reflection.

An analytical description of the water jet reflection is not possible as it is a three-dimensional transient flow problem. It can be solved numerically and modelling and simulation of the phenomenon should be developed in the future. At this point it was only possible to describe the effect qualitatively.

The minimization of the surface energy of the water was identified as driving force for the reflection as well as for the oscillations observed in the outgoing jet.

It was found that the ratio of take-off angle and angle of incidence does not depend on the flow length and water pressure over a large range. This might be proof for slip flow of the water across the ultrahydrophobic surface. First experiments of water jet reflection on rotating ultrahydrophobic surfaces seem to confirm the friction-less slip flow on these surfaces as the reflection seems to be unaffected by the substrate rotation. More experiments to confirm these first results should be performed.

The ratio of take-off angle and angle of incidence does not depend on the angle of incidence, too, and for both needle lengths, the reflection phenomenon was observed and the needle length had no influence on the ratio.

An improved experimental setup that allows exact control and measurement of the water pressure will help to gain further insight into the phenomenon as it will allow a more quantitative analysis which is also required for modeling. Also, a high speed camera would make it possible to study the first instance after impact of the jet more closely in order to determine whether a dynamic process exists before a steady state is established.

An effect like the splitting of water jets which is undesired for a systematic study of the phenomenon might on the other hand lead to new interesting applications like fluid manipulation and mixing.

If the slip flow on these surfaces can be confirmed by further experiments this might be of great interest for engineering applications as in fluid pipes and bearings due to the lower friction.

5.7 Author's Related Publications

[1] M.Scharnberg, V. Zaporojtchenko, R. Adelung, F. Faupel, and A.W. Hassel, manuscript in preparation

6 General Conclusions and Outlook

In this work, two types of functional organic thin films were examined with respect to their use in technical applications as well to basic research.

The first system, organic semiconductors consisting of small molecules, is used as semiconductor in organic field effect transistors. One of the challenges arising from the implementation of organic semiconductors is the penetration of metal atoms into the organic thin film during metallization. The diffusion behaviour of noble metals in organic molecular thin films of pentacene and diindenoperylene was examined with high resolution depth profiles obtained by radiotracer measurements. It was found that the basic diffusion processes are comparable to noble metal diffusion in polymers while differences are observed due to the different microstructures. The experiments showed that most metal atoms remain on or near the surface of the organic film, but a small fraction of metal atoms diffuses through the film and in some cases they accumulate at the interface between organic film and substrate. Grain boundaries in the crystalline small molecule semiconductors were identified as fast diffusion paths.

These findings are of great relevance to technical applications. Even at the high deposition rates used in industrial applications small amounts of metal can diffuse into the organic material in the early stages of contact deposition before a closed layer is formed. These small amounts can strongly alter the device performance and the charge carrier injection at the metal-organic semiconductor interface. In fact, the correlation of I-V measurements and radiotracer measurements of Au contacts on pentacene indicate that increased diffusion during deposition of the contacts leads to an increased contact resistance. This is a very important result since the charge carrier injection is of great importance for the device performance. In order to control diffusion, a submonolayer of Cr was deposited as a barrier layer and it was shown that just a submonolayer of Cr can already influence the noble metal diffusion but is less effective than for amorphous polymers because the grain boundaries of the polycrystalline films act as fast diffusion paths.

The feasibility of radiotracer diffusion measurements for organic crystalline semicon-

ductors was demonstrated. It is also of interest for other organic functional thin films, i.e. organic semiconductors in organic solar cells and organic light emitting diodes. In these devices, metal deposition onto the organic thin films is often required, and metal diffusion might degrade the device performance. Examination and control of metal diffusion in these systems might be an interesting and important application of the radiotracer technique.

The second organic thin film system that was examined are Teflon-based functional thin films. The utilization of different material properties of these films for technical applications was studied.

It was examined if Teflon thin films can be used as capping layers for organic field effect transistors. Pentacene and other organic semiconductors are prone to degradation due to ambient air which poses a large problem for possible applications of organic semiconductors. The threshold voltage as well as the on/off current ratio are negatively influenced by aging. While a thin Teflon film deposited on top of the pentacene can protect the semiconductor against aging due to exposure to moisture oxygen permeation is not prevented. Thus Teflon thin films alone cannot act as barrier layers. But they might be of great interest for multilayer barrier systems. In existing multilayer barrier systems the polymer is deposited by methods that are not compatible with in-batch processing. Alternating sputtering of Teflon PTFE with Al_2O_3 might allow the fabrication of multi-layer capping layers for protection of organic field effect transistors and also organic light emitting diodes against oxygen and moisture that are compatible with in-batch processing.

In addition, the Teflon films can be further functionalized by charging them as electrets, allowing control of the threshold voltage of organic thin film transistors. This electret-based dual gate field-effect transistor structure allowed to shift the threshold voltage of a transistor to low voltages that are required for technological applications like portable multimedia devices.

The third application of Teflon-based thin films also utilizes the low surface energy and hydrophobic nature of the Teflon surface. A functional organic thin film based on sputtered PTFE was deposited onto a microstructured metal alloy surface creating a ultrahydrophobic surface that showed a contact angle of $>160^\circ$ for water. On these substrates as well as on biological ultrahydrophobic surfaces, e.g., the leaves of the nasturtium plant, a phenomenon was discovered that was not observed for water jets so far. A water jet that impinges on the surface below a critical angle flows across the surface for several beam diameters before it takes off from the surface again as a coherent jet

with comparable jet diameter. The phenomenon was examined qualitatively and the dependence of the take-off angle on the angle of incidence and the water pressure as well as the microstructure of the surface was described. This demonstrates that the functional organic thin films are also of interest for basic research. But water jet reflection on ultrahydrophobic system might also find applications in fluidic systems for friction-less guidance of liquids.

The functional organic thin films examined in this work are used in a wide range of applications ranging from basic research to advanced organic electronics. E.g., a combination of the electronic properties of one organic thin film, i.e. a semiconductor, and the chemical and electronic properties of another organic film, i.e. Teflon-based thin films, can modify existing devices.

In conclusion, it was demonstrated, that organic thin films can alter the mechanical, chemical and electronic properties of their substrates on a macroscopic scale leading to modified or new functionalities.

Bibliography

- [1] L. Torsi, N. Cioffi, C. D. Franco, L. Sabbatini, P. Zambonin, and T. Bleve-Zacheo, *Solid-State Electronics* **45**, 1479 (2001).
- [2] P. Peumans, A. Yakimov, and S. Forrest, *J. Appl. Phys.* **93** (7), 3693 (2003).
- [3] U. Schürmann, H. Takele, V. Zaporojtchenko, and F. Faupel, *Thin Solid Films* **515**, 801 (2006).
- [4] K. L. Prime and G. M. Whitesides, *Science* **252**, 1164 (1991).
- [5] C. E. D. Chidsey, *Science* **251**, 919 (1991).
- [6] International technology roadmap for semiconductors (itrs), Tech. rep. (2005).
- [7] J. H. Burroughes, D. D. C. Bradley, A. R. Brown, R. N. Marks, K. Mackay, R. H. Friend, P. L. Burns, and A. B. Holmes, *Nature* **347**, 539 (1990).
- [8] C. Dimitrakopoulos and P. Malenfant, *Adv. Mater.* **14**, 99 (2002).
- [9] H. Hoppe and N. S. Sariciftci, *J. Mater. Res.* **19** (7), 1924 (2004).
- [10] S. Lee, B. Koo, J.-G. Park, H. Moon, J. Hahn, and J. Kim, *MRS Bulletin* **31**, 455 (2006).
- [11] Y. Park, J. Lim, H. Lee, and K. Cho, *materials today* **10** (3), 46 (2007).
- [12] M. Pope and C. Swenberg, *Electronic Processes in Organic Crystals and Polymers*, Oxford University Press, Oxford, 2nd edn. (1999).
- [13] D. F. Barbe and C. R. Westgate, *J. Phys. Chem. Solids* **31** (12), 2679 (1970).
- [14] S. Sze, *Semiconductor Devices - Physics and Technology*, John Wiley & Sons, 2nd edn. (2002).

- [15] T. Kelley, D. Muyres, P. Baude, T. Smith, and T. Jones, *Organic Crystals and Polymers*, vol. 771, p. 169, Mat. res. Soc. Symp. Proc., Warrendale, PA, USA, 2nd edn. (2003).
- [16] N. Karl, K.-H. Kraft, J. Marktanner, M. Münch, F. Schatz, R. Stehle, and H.-M. Uhde, *J. Vac. Sci. Technol. A* **17**, 2318 (1999).
- [17] V. Sundar, J. Zaumseil, V. Podzorov, E. Menard, R. Willet, T. Someya, M. Gershenson, and J. Rogers, *Science* **303**, 1644 (2004).
- [18] R. Zeis, C. Besnard, T. Siegrist, C. Schlockermann, X. Chi, and C. Kloc, *Chem. Mater.* **18**, 244 (2006).
- [19] A. Facchetti, M. Yoon, C. Stern, G. Hutchison, M. Ratner, and T. Marks, *J. Am. Chem. Soc.* **126** (41), 13480 (2004).
- [20] H. Ishii, K. Sugiyama, E. Ito, and K. Seki, *Adv. Mater.* **11** (8), 605 (1999).
- [21] S. Nelson, Y.-Y. Lin, D. Gundlach, and T. Jackson, *Appl. Phys. Lett.* **72**, 1854 (1998).
- [22] Y.-Y. Lin, D. Gundlach, S. Nelson, and T. Jackson, *IEEE Electron Device Lett.* **18**, 606 (1997).
- [23] C. Dimitrakopoulos, S. Purushothaman, K. Kymissis, A. Callegari, and J. Shaw, *Science* **283**, 822 (1999).
- [24] S. Fritz, S. Martin, C. Frisbie, M. Ward, and M. Toney, *J. Am. Chem. Soc.* **126**, 4084 (2004).
- [25] A. Dürr, N. Koch, M. Kelsch, A. Rühm, J. Ghijsen, R. Johnson, J. Pireaux, J. Schwartz, H. Dosch, and A. Kahn, *Phys. Rev. B* **68**, 115428 (2003).
- [26] G. Horowitz, *Semiconducting polymers : chemistry, physics and engineering*, chap. Physics of Organic Field-Effect Transistors, p. 463, Weinheim (2000).
- [27] B. Streetman and S. Banerjee, *Solid State Electronic Devices*, Pearson Prentice Hall, New Jersey, 6th edn. (2006).
- [28] J. Bardeen and W. Brattain, *Phys. Rev.* **74**, 230 (1948).
- [29] W. Shockley, *Bell Syst. Techn. J.* **28**, 435 (1949).

-
- [30] D. Kahn and M. Atalla, Carnegie Institute of Technology, Pittsburgh, PA (1960).
- [31] G. Horowitz, *Adv. Mater.* **10**, 365 (1998).
- [32] S. Scheinert and G. Paasch, *Physics of Organic Semiconductors*, chap. Fabrication and Analysis of Polymer Field-Effect Transistors, p. 343, Wiley-VCH, Berlin, 1st edn. (2005).
- [33] C. Dimitrakopoulos, J. Kymissis, and S. Purushothaman, in *Proceedings of The Int. Conf. on Digital Printing Technologies*, pp. 493–496, Society of Imaging Science and Technology (2000).
- [34] J. Kymissis, M.s., Mass. Inst. Tech., Cambridge, MA (1999).
- [35] J. Kymissis, C. Dimitrakopoulos, and S. Purushothaman, *IEEE Trans. Electron Devices* **48**, 1060 (2001).
- [36] H. Ishii, N. Hayashi, and K. Seki, *Conjugated Polymer and Molecular Interfaces*, chap. Energy Level Alignment at Organic-Metal Interfaces, M. Dekker, New York (2002).
- [37] C. Shen, A. Kahn, and I. Hill, *Conjugated Polymer and Molecular Interfaces*, chap. Organic Molecular Interfaces, M. Dekker, New York (2002).
- [38] N. Koch, G. Leising, A. Rajagopal, and J. Pireaux, *Conjugated Polymer and Molecular Interfaces*, chap. Organic Interfaces, M. Dekker, New York (2002).
- [39] A. Dürr, F. Schreiber, M. Kelsch, H. Carstanjen, and H. Dosch, *Adv. Mater.* **14**, 961 (2002).
- [40] D. Gupta and R. Tsui, *Appl. Phys. Lett.* **17** (7), 294 (1970).
- [41] F. Faupel, D. Gupta, B. Silverman, and P. Ho, *Appl. Phys. Lett.* **55**, 357 (1989).
- [42] F. Faupel, R. Willecke, and A. Thran, *Mater. Sci. Eng.* **R22** (1) (1998).
- [43] F. Faupel, A. Thran, V. Zaporozhchenko, T. Strunskus, and M. Kiene, *Diffusion in Advanced Technological Materials*, chap. Metal diffusion in polymers and on polymer surfaces, Noyes Publication, William Andrew Publishing (2004).
- [44] A. Dürr, F. Schreiber, M. Kelsch, H. Carstanjen, H. Dosch, and O. Seeck, *J. Appl. Phys.* **93** (9), 5201 (2003).

- [45] Y. Hirose, A. Kahn, V. Aristov, and P. Soukiassian, *Appl. Phys. Lett.* **68**, 217 (1996).
- [46] A. Thran, T. Strunskus, V. Zaporojtchenko, and F. Faupel, *Appl. Phys. Lett.* **81**, 244 (2002).
- [47] M. Ohring, *The Materials Science of Thin Films*, Academic Press, San Diego, 2nd edn. (1992).
- [48] D. Mattox, *Handbook of Physical Vapour Deposition Processing*, Noyes Publications, New Jersey (1998).
- [49] J. Zekonyte, *Sputtering and Surface Modification of Thermoplastic Polymers with Low Energy Ion Beams*, Ph.D. thesis, Technische Fakultät der Christian-Albrechts-Universität zu Kiel (2005).
- [50] C. Reimann, *K. Dan. Vidensk. Selsk. Mat. Fys. Medd.* **43**, 351 (1993).
- [51] P. Sigmund, *Sputtering by Particle Bombardment*, vol. I, p. 9, Springer Verlag, Berlin (1981).
- [52] J. Malherbe, *Crit. Rev. Solid St. Mat. Sci.* **19 (2)**, 55 (1994).
- [53] B. Chapman, *Glow Discharge Processes*, John Wiley & Sons, New York (1980).
- [54] J. Mahan, *Physical Vapor Deposition of Thin Films*, John Wiley & Sons, New York (2000).
- [55] P. Fettweis, J. Verplancke, R. Venkataraman, B. Young, and H. Schwenn, *Handbook of Radioactivity Analysis*, chap. Semiconductor Detectors, p. 239, Academic Press, 2nd edn. (2003).
- [56] H. Gokan, S. Esho, and Y. Ohnishi, *J. Electrochem. Soc.* **130**, 143 (1984).
- [57] F. Faupel, P. Hüppe, K. Rätzke, R. Willecke, and T. Hehenkamp, *J. Vac. Sci. Technol. A* **10**, 92 (1992).
- [58] A. Thran, M. Kiene, V. Zaporojtchenko, and F. Faupel, *Phys. Rev. Lett.* **82**, 1903 (1999).
- [59] A. Thran, M. Kiene, V. Zaporojtchenko, and F. Faupel, *MRS Bulletin* **3** (1999).

-
- [60] F. LeGoues, B. Silverman, and P. Ho, *J. Vac. Sci. Technol. A* **6**, 2200 (1988).
- [61] S. K. Saha, *Phys. Rev. B* **69**, 125416 (2004).
- [62] A. Kiesow, J. Morris, C. Radehaus, and A. Heilmann, *J. Appl. Phys.* **94** (10), 6988 (2003).
- [63] A. Thran, *Diffusion von Gasen und Metallen in Polymeren: Datenanalysen, Experimente und Simulationen*, Ph.D. thesis, Christian-Albrechts-Universität zu Kiel (2000).
- [64] S. Haukka, N. Raaijmakers, K.-E. Elers, J. Kostamo, W.-M. Li, H. Sprey, P. Soininen, and M. Tuominen, in *IITC*, p. 279 (2002).
- [65] P. Burrows, V. Bulovic, S. Forrest, L. Sapochak, D. McCarty, and M. Thompson, *Appl. Phys. Lett.* **65** (23), 2922 (1994).
- [66] P. Burrows, G. Graff, M. Gross, P. Martin, M. Shi, M. Hall, E. Mast, C. Bonham, W. Bennett, and M. Sullivan, *Displays* **22**, 65 (2001).
- [67] A. Chwang, M. Rothman, S. Mao, R. Hewitt, M. Weaver, J. Silvernail, K. Rajan, M. Hack, and J. Brown, *Appl. Phys. Lett.* **83** (3), 413 (2003).
- [68] M. Weaver, L. Michalski, K. Rajan, M. Rothman, J. Silvernail, and J. Brown, *Appl. Phys. Lett.* **81** (16), 2929 (2002).
- [69] J. Affinito, S. Eufinger, M. Gross, G. Graff, and P. Martin, *Thin Solid Films* **308-309**, 19 (1997).
- [70] H. Chatman, *Surf. Coat. Technology* **78**, 1 (1996).
- [71] J. Affinito, M. Gross, P. Mournier, M. Shi, and G. Graff, *J. Vac. Sci. Technol. A* **17**, 1974 (1999).
- [72] J. Affinito, *Thin Solid Films* **420-421**, 1 (2002).
- [73] J. Affinito, in *Proceedings of the 45th Annual Society of Vacuum Coaters Technical Conference*, pp. 425–439 (2002).
- [74] H. Biederman, *Vacuum* **31**, 285 (1981).
- [75] H. Biederman, J. Jezek, P. Bilkova, P. Hlidek, D. Slavinska, and J. Zemek, *Intern.Symp.Plasm.Chem.* **13**, 1264 (1997).

- [76] U. Schürmann, *Eigenschaften von Polymer-Silber-Nanokompositen hergestellt durch Co-Sputtern*, Ph.D. thesis, Technische Fakultät der Christian-Albrechts-Universität zu Kiel (2006).
- [77] D. Smith, *Thin Film Deposition*, McGraw-Hill (1995).
- [78] G. Sauerbey, *Z. Phys.* **155**, 206 (1959).
- [79] C. Lu and O. Lewis, *J. Appl. Phys.* **43** (11), 4385 (1972).
- [80] D. Gamota and P. Brazis, *IEEE Standard Test Methods for the Characterization of Organic Transistors and Materials*, The Institute of Electrical and Electronics Engineers (2004).
- [81] E. Meijer, C. Tanase, P. Blom, E. V. Veenendaal, B.-H. Huisman, D. D. Leeuw, and T. Klapwijk, *Appl. Phys. Lett.* **80** (20), 3838 (2002).
- [82] S. Kim, H. Choi, and J. Jang, *Appl. Phys. Lett.* **85** (19), 4514 (2004).
- [83] J. Northrup and M. Chabinyk, *Phys. Rev. B* **68**, 041202(R) (2003).
- [84] O. Jurescu, J. Baas, and T. Palstra, *Appl. Phys. Lett.* **84** (16), 3061 (2004).
- [85] C. Pannemann, T. Diekmann, and U. Hilleringmann, *JMR* **19**, 1999 (2004).
- [86] C. Pannemann, T. Diekmann, U. Hilleringmann, U. Schürmann, M. Scharnberg, V. Zaporozhchenko, R. Adelung, and F. Faupel, in *Proc. of the IEEE Polytronic 2005 conference*, vol. IEEE Catalog No. 05TH8855C, p. 63 (2005).
- [87] Y.-W. Wang, H.-L. Cheng, Y.-K. Wang, T.-H. Hu, J.-C. Ho, C.-C. Lee, T.-F. Lei, and C.-F. Yeh, *Thin Solid Films* **491**, 305 (2005).
- [88] I. Kymissis, C. Dimitrakopoulos, and S. Purushothaman, *J. Vac. Sci. Technol. B* **20** (3), 956 (2002).
- [89] S. Lim, S. Kim, J. Lee, M. Kim, D. Kim, and T. Zyung, *Synthetic Metals* **148**, 75 (2005).
- [90] M. Lee and C. Song, *Japanese Journal of Applied Physics* **42** (7A), 4218 (2003).
- [91] A. Wang, I. Kymissis, V. Bulovic, and A. I. Akinwande (2005).

-
- [92] S. Iba, T. Sekitani, Y. Kato, T. Someya, H. Kawaguchi, M. Takamiya, T. Sakurai, and S. Takagi, *Appl. Phys. Lett.* **87**, 023509 (2005).
- [93] C. Huang, J. West, and H. Katz, *Mater. Res. Soc. Symp. Proc.* **889**, 0889 (2006).
- [94] G. Sessler, (Editor) *Electrets*, Springer Verlag Berlin Heidelberg, 2nd edn. (1987).
- [95] R. Schwödiauer, G. Neugschwandtner, S. Bauer-Gogonea, S. Bauer, and W. Wirges, *Appl. Phys. Lett.* **75 (25)**, 3998 (1999).
- [96] R. Schwödiauer, S. Bauer-Gogonea, S. Bauer, J. Heitz, and D. Bäuerle, *Appl. Phys. Lett.* **73**, 2941 (1998).
- [97] T. Nason, J. Moore, and T. Lu, *Appl. Phys. Lett.* **60 (15)**, 1866 (1992).
- [98] R. Hirschberg, V. Zaporojtchenko, and F. Faupel, unpublished.
- [99] M. Scharnberg, V. Zaporojtchenko, and F. Faupel, unpublished.
- [100] P. Resnick, *Polym. Prepr.* **31 (1)**, 312 (1990).
- [101] C. Pannemann, T. Diekmann, and U. Hilleringmann, in *Proc. of the 16th International IEEE Conf. on Microelectronics ICM 2004*, p. 79 (2004).
- [102] X.-M. Li, *Chem. Soc. Rev.* (2007).
- [103] W. C. Baker, *Proceedings of the Physical Society* **40 (1)**, 181 (1927).
- [104] G. Hartley and R. Brunskill, *Surface Phenomena in Chemistry and Biology*, p. 214, Pergamon, Oxford (1958).
- [105] D. Richard and D. Quéré, *Europhys. Lett.* **50**, 769 (2000).
- [106] P. Aussillous and D. Quéré, *Nature* **411**, 924 (2001).
- [107] A. Otten and S. Herminghaus, *Langmuir* **20**, 2405 (2004).
- [108] K. Jackson and J. Hunt, *Trans. Met. Soc. AIME* **236**, 1129 (1966).
- [109] W. Kurz and E. Sahm, *Gerichtet erstarrte eutektische Werkstoffe*, Springer, Berlin (1975).
- [110] A.-W. Hassel, S. Milenkovic, U. Schürmann, H. Greve, V. Zaporojtchenko, R. Adelung, and F. Faupel, *Langmuir* **23 (4)**, 2091 (2007).

- [111] L. Rayleigh, *Proc. Roy. Soc.* **29**, 71 (1879).
- [112] J. Hoyt and J. Taylor, *AIAA Journal* **16**, 85 (1978).
- [113] D. Richard, C. Clanet, and D. Quéré, *Nature* **417**, 811 (2002).
- [114] C.-H. Choi and C.-J. Kim, *Phys. Rev. Lett.* **96**, 066001 (2006).
- [115] L. Bocquet, *Phys. Rev. Lett.* **97**, 109601 (2006).
- [116] C.-H. Choi and C.-J. Kim, *Phys. Rev. Lett.* **97**, 109602 (2006).

List of Figures

2.1	Energy diagrams of molecules	6
2.2	Chemical structure of Pc and DIP	7
2.3	Crystallographic structure of Pentacene	8
2.4	Schematic representation of a DIP unit cell	8
2.5	Energy diagram of a MIS junction	10
2.6	Metal-semiconductor junction	11
2.7	MOSFET structures	13
2.8	TOC and BOC-TFT	15
2.9	UHV chamber for radiotracer deposition	19
2.10	Schematic of the metal evaporator	20
2.11	Processes during ion impingement	21
2.12	UHV chamber for serial sectioning	23
2.13	Sputter mask	25
2.14	Height profile	26
2.15	Schematic of the contact pattern	28
2.16	Processes during film growth	29
2.17	Thin film growth modes	29
2.18	AFM images of unspattered and spattered Pc	32
2.19	AFM images of unspattered and spattered diindenoperylene	33
2.20	Pc and DIP depth profiles for Ag diffusion	34
2.21	Influence of interface sputtering on depth profiles	35
2.22	Chemical structure of TMC-PC	36
2.23	Ag diffusion in DIP and TMC-PC	36
2.24	Depth profiles for 8 and 80 min. tracer deposition	38
2.25	Temperature Dependence of the Ag depth profiles	39
2.26	Temperature dependence of the Ag concentration vs d^2	40
2.27	Accumulation at interface at three temperatures	41
2.28	Influence of film structure on depth profile	42

2.29	Dependence of the metal diffusion on the film structure	43
2.30	Depth profiles for DIP films with and without Cr diffusion barrier	45
2.31	Depth profiles for Au diffusion in DIP	46
2.32	Transition in the I-V curve of the contacts	48
2.33	I-V curve showing switching in the I-V characteristic	49
2.34	I-V dependence of two Au contact arrays	51
2.35	I-V dependence of Au contact array	52
2.36	Comparison of I-V curves of different contacts	52
2.37	Aging of I-V characteristics	54
2.38	I-V curve of asymmetric contacts	54
3.1	Chemical Structure of polytetrafluoroethylene (PTFE).	60
3.2	Schematic of a planar magnetron	62
3.3	UHV chamber for sputter deposition of PTFE	63
3.4	Chemical structure of pentacenequinone.	65
3.5	Pc-BOC-FET	66
3.6	$I_{DS} - V_{DS}$ characteristics of an OTFT	68
4.1	Cross-sectional illustration of a dual gate organic transistor	72
4.2	Schematic representation of an electret	73
4.3	Band diagram of an electret	74
4.4	Charge stability of PTFE	75
4.5	Chemical structure of Teflon AF.	76
4.6	UHV chamber for polymer evaporation	77
4.7	Schematic of the polymer evaporator	77
4.8	Schematic of the corona discharge setup	78
4.9	I_{DS} vs V_{DS} of the Pc-TFT prior to and after electret deposition	81
4.10	$\sqrt{I_{DS}}$ vs V_{GS} of the Pc-TFT prior to and after electret deposition	82
5.1	SEM image of a Nasturtium leaf surface	89
5.2	SEM image of metal nanofibers	90
5.3	Water drops on a ultrahydrophobic surface	90
5.4	Water jet reflection on a Nasturtium leaf (side view)	92
5.5	Water jet reflection on a Nasturtium leaf (top view)	93
5.6	Oscillations in the water jet	93
5.7	Water jet reflection on an artificial ultrahydrophobic surface (short fibers)	94
5.8	Water jet reflection on an artificial ultrahydrophobic surface (long fibers)	95

5.9	Angle analysis for Nasturtium	96
5.10	Angle analysis for short-fiber artificial ultrahydrophobic surfaces	97
5.11	Angle analysis for long-fiber artificial ultrahydrophobic surfaces	97
5.12	Multiple reflection of a water jet	98

List of Tables

2.1	Mobilities of selected semiconductors	5
2.2	Sputter regimes	21
2.3	Sputter yields of selected elements	22
2.4	Ge properties	24
2.5	Details of DIP films with different microstructures	42
3.1	Degradation data	68

Acknowledgments

First and foremost I thank Prof. Dr. Franz Faupel and Prof. Dr. Rainer Adelung. The former for giving me the opportunity to do this work at his chair and for recommending me first to Dr. Paul S. Ho and then to Dr. Adelung. The latter I thank for "‘hiring me unseen"’, for the interesting topic and especially the great support throughout the whole work and for "‘watching my back"’.

Dipl.-Ing. Stefan Rehders provided a lot of technical support and helped to realize new ideas which of course were always due yesterday and delivered in time. No just for this he deserves my gratitude.

My computer problems were solved by Dipl.-Ing. Rainer Kloth and Dipl.-Geol. Beate Minten explained and fought University bureaucracy for me.

Thanks a lot to Dipl.-Ing. Jan Kruse for the Latex troubleshooting.

Dr. Christoph Pannemann and Dipl.-Ing. Thomas Diekmann from the University of Paderborn as well as Dr. Jens Pflaum from the University of Stuttgart I thank for providing the samples for my work.

Dr. Jörn Kanzow introduced me into the lab equipment allowing me a quick start into my thesis. Thanks also for his scientific skepticism. I´m very grateful for his and his wife Indre´s friendship.

Dr. Klaus Rätzke and Dr. Vladimir Zaporojtchenko provided a lot of fruitful scientific discussions. Klaus Rätzke was also the first line of defense concerning questions of all kinds and guided me in the radiotracer lab.

Thanks to Dipl.-Ing. Christian Hanisch, Dipl.-Ing. Sebastian Wille, M.Sc. Jingping Hu, M.Sc. Ding Li and Kerstin Meurisch for contributing to this work.

I´d like to thank Dipl.-Ing. Alexander Bartsch, Dr. Ulrich Schürmann, Dipl.-Ing. Christian Hanisch, Dipl.-Ing. Sebastian Wille, Dipl.-Ing. Jan Kruse, Dipl.-Phys. Tomislav Hrkac, Dipl.-Ing. Henry Greve, M.Sc. Mady Elbahri and all the other members and former members of the Chair of Multicomponent Materials for their friendship and the familiar atmosphere at work which I find quite special.

Last but certainly not least, I thank my family. Not only for moving my stuff all the time but for all the support. And my fiancée Diana for making everything so much better.

Curriculum Vitae

Name: Michael Scharnberg
Address: Johann-Fleck-Straße 21, 24106 Kiel
Born: 17.Mai 1977 in Preetz
Parents: Doris Hedwig Scharnberg geb. Wüstholtz
Joachim Alexander Scharnberg

School Education

1983 - 1987 Rodomstorschule in Plön
1987 - 1996 Internatsgymnasium Schloss Plön in Plön
6/94 Graduation (Abitur)

Academic Education

10/1997 - 08/2001 Student in Materials Science
at the Christian-Albrechts-University in Kiel
09/2001 - 08/2003 Graduate Student in Materials Science
at the University of Texas at Austin
08/2003 Master Thesis: "Atomic Layer Deposition and Interfacial
Chemistry during Tantalum Based Barrier Layer
Deposition on Low-k Dielectrics"

Occupational History

04/2000 - 08/2001 Teaching and Research Assistant at the Chair for Multicomponent
Materials at the Christian-Albrechts-University Kiel
09/2001 - 12/2001 Teaching Assistant at the Mechanical Engineering Department
at the University of Texas at Austin
01/2002 - 08/2003 Research Assistant at the Laboratory for Interconnect
and Packaging at the University of Texas at Austin
09/2003 - Researcher at the Chair for Multicomponent Materials
at the Christian-Albrechts-University Kiel